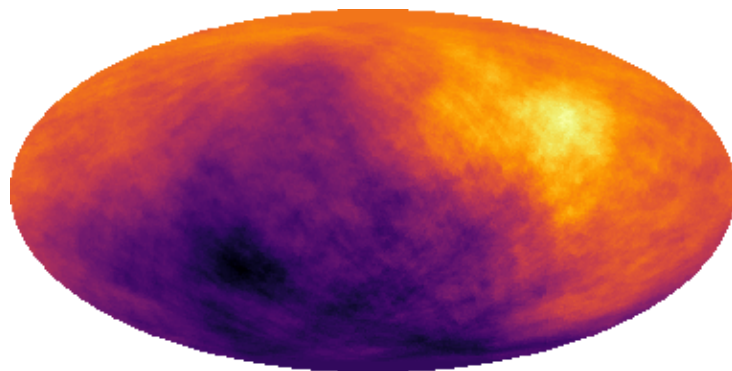


FACULTY OF PHYSICS  
LUDWIG-MAXIMILIANS-UNIVERSITÄT MÜNCHEN

MASTER'S THESIS

# The Cosmic Matter Dipole



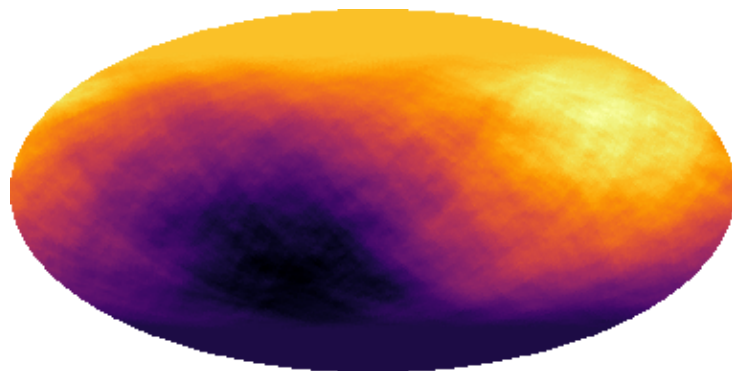
AUTHOR:  
Tobias Nadolny

DATE:  
15 April 2021

FAKULTÄT FÜR PHYSIK  
LUDWIG-MAXIMILIANS-UNIVERSITÄT MÜNCHEN

MASTERARBEIT

# Der kosmische Materiedipol



AUTOR:  
Tobias Nadolny

DATUM:  
15. April 2021

Supervisor (University of Geneva):

Professor Dr. Ruth Durrer

Professor Dr. Martin Kunz

Dr. Hamsa Padmanabhan

Supervisor (LMU):

Professor Dr. Jochen Weller

## Abstract

The cosmological principle - the assumption of homogeneity and isotropy - is fundamental in the standard model of cosmology. Building on this assumption, anisotropies in the observable number density of galaxies on the sky are constrained. The anisotropy on the largest scale is referred to as the cosmic matter dipole. Next to matter density fluctuations which lead to an intrinsic dipole, Doppler effects and relativistic aberration due to our motion with respect to the observed galaxies cause an additional contribution to the dipole. The amplitude and direction of this kinematic dipole are extremely well constrained if the cosmic microwave background dipole is interpreted as a purely kinematic effect, such that our velocity can be inferred from it.

Several studies of the dipole in the distribution of radio sources and quasars as tracers of the matter distribution have been conducted. They give evidence that the amplitude of the cosmic matter dipole is larger than predicted by the standard model of cosmology, while its direction is consistent with expectations. This challenges the assumption of isotropy as well as the exclusively kinematic interpretation of the cosmic microwave background dipole. It is therefore important to investigate this discrepancy further.

In this master thesis, first, the relevant theory of the cosmic matter dipole is studied. Secondly, a catalog of radio sources and a sample of quasars as two different tracers of the matter distribution are analysed with regard to the dipole. Thereby, it is found that the main systematic uncertainty originates in the intrinsic dipole. For this reason, thirdly, a new method is proposed to distinguish the intrinsic dipole from the kinematic dipole. This is achieved by involving not only the flux or magnitude but also additional properties of the observed sources such as their size or redshift. The potential of this new method is demonstrated by showing how it can be applied in two different future galaxy and radio surveys. By simulations, we confirm that the velocity and the intrinsic dipole can indeed be measured separately.

*The figure on the English title page shows the distribution of radio sources observed by the NVSS.*

*The figure on the German title page shows the distribution of the quasar sample from [27]*

*The distributions are smoothed in such a way that only the dipole is visible.*

# Table of Contents

<b>Abstract</b>	<b>i</b>
<b>1 Introduction</b>	<b>1</b>
1.1 Cosmological Principle . . . . .	2
1.2 Cosmic Microwave Background Velocity . . . . .	2
1.3 Previous Work . . . . .	4
<b>2 Theory of the Cosmic Matter Dipole</b>	<b>5</b>
2.1 Kinematic Dipole . . . . .	6
2.1.1 Standard Derivation . . . . .	6
2.1.2 General Relativistic Derivation . . . . .	8
2.2 Intrinsic Dipole . . . . .	9
2.3 Shot Noise . . . . .	12
2.4 Effect of Incomplete Sky Coverage . . . . .	13
2.5 Combined Dipole . . . . .	17
2.6 Evaluation of the Significance . . . . .	22
2.7 Dipole Estimator . . . . .	24
<b>3 NVSS Radio Sources Dipole</b>	<b>25</b>
3.1 Measuring the Dipole . . . . .	25
3.1.1 Data . . . . .	25
3.1.2 Mask . . . . .	27
3.1.3 Results . . . . .	29
3.2 Simulations . . . . .	30
3.2.1 Angular Power Spectrum . . . . .	30
3.2.2 Mock Catalogs . . . . .	31
3.3 Results . . . . .	33
3.4 Higher Multipoles . . . . .	35
<b>4 Quasar Dipole</b>	<b>38</b>
4.1 Dipole . . . . .	38
4.2 Intrinsic Clustering . . . . .	41

<b>5</b>	<b>New Method with Weighted Dipoles</b>	<b>43</b>
5.1	Possible Weights . . . . .	43
5.2	Weighted Dipole . . . . .	45
5.3	Velocity and Intrinsic Dipole Estimators . . . . .	47
5.4	Shot Noise . . . . .	47
5.5	Applications . . . . .	49
5.5.1	LSST/Euclid . . . . .	49
5.5.2	SKA . . . . .	52
5.6	Optimal Weights . . . . .	53
5.7	Caveats . . . . .	55
5.8	Results . . . . .	57
5.8.1	Measuring our Velocity . . . . .	57
5.8.2	Effect of Measurement Uncertainty . . . . .	61
5.8.3	Measuring the Intrinsic Dipole . . . . .	61
<b>6</b>	<b>Conclusions</b>	<b>65</b>
	<b>Appendix</b>	<b>67</b>
<b>A</b>	<b>Spherical Harmonics</b>	<b>67</b>
A.1	Basics . . . . .	67
A.2	Realizing Fluctuations from the Angular Power Spectrum . . . . .	68
A.3	Relation with the Dipole . . . . .	69
<b>B</b>	<b>Contributions to the Angular Power Spectrum</b>	<b>71</b>
<b>C</b>	<b>Multipole Estimator</b>	<b>73</b>
<b>D</b>	<b>Bulk Flow Velocity</b>	<b>75</b>
	<b>List of Acronyms</b>	<b>76</b>
	<b>Bibliography</b>	<b>77</b>

# 1 Introduction

The standard model of cosmology, our current understanding of the history of the universe, is based on two fundamental assumptions, isotropy and homogeneity. This is often referred to as the cosmological principle [1]. In this work, the isotropy of the matter distribution in the universe is investigated. Since in our local neighbourhood, the universe is certainly not isotropic, in order to test the isotropy, one needs to probe the distribution of very distant, hence cosmic matter. To do so, catalogues of  $10^5$ – $10^8$  radio sources, quasars, or in general galaxies are analysed. Their distribution on the sky serves as a tracer of the matter distribution which is analysed carefully to find small,  $\lesssim 1\%$  deviations from the mean number density.

This thesis focuses on the anisotropy on the largest scale. Expanding the matter distribution in spherical harmonics, the largest scale is characterized by the first multipole, the dipole. The anisotropy in the distribution of distant matter on the largest scale is thus referred to as the cosmic matter dipole. Studying the dipole instead of for example the quadrupole or even higher multipoles is particularly interesting because relativistic aberration and Doppler effects due to our motion with respect to the observed galaxies also give a dipole contribution to first order in the velocity.

Both, this kinematic dipole as well as the intrinsic fluctuations in the matter distribution are extremely well constrained by the standard model of cosmology. However, previous studies have found evidence that the amplitude of this dipole is larger than expected. Therefore, investigating the cosmic matter dipole serves as an important test of the model. Put simply, this work is aimed to answer two elementary questions:

*Is there a direction on the sky defining a hemisphere that has significantly more matter in it than the opposite hemisphere?*

*How fast and in which direction are we moving with respect to the mean rest frame of distant galaxies?*

The following sections make the assumption of isotropy more precise and discuss the expected velocity from observations of the cosmic microwave background (CMB). The end of this introduction puts this work into the context of previous studies concerning the dipole in the matter distribution.

## 1.1 Cosmological Principle

The simplest model of the universe is a spherically symmetric and homogeneous one, where no direction and no point in space is special. Therefore, it is reasonable that the standard model of cosmology builds on the assumption that the universe is isotropic and homogeneous, the cosmological principle.

There is also a weaker assumption, the Copernican principle, which states that we are not a special observer in the universe. The two principles are related in the following way. If we observe isotropy, by invoking only the Copernican principle, one should also observe an isotropic universe at other points in the universe. Since from isotropy at more than one point in space follows homogeneity [2], the weaker Copernican principle together with isotropy thus leads to homogeneity and therefore the cosmological principle (see also the discussion in [3]). However, homogeneity does not imply isotropy. A constant velocity field, for example, is homogeneous but not isotropic.

It is important to precisely state what is meant by homogeneity and isotropy. First, the universe is certainly not exactly homogeneous and isotropic but only statistically, in the sense that averages over a certain volume or solid angle will have the same value everywhere. Secondly, on small distances, the universe is not homogeneous and isotropic even when averaged. For example, we can observe a highly clustered distribution of galaxies in our local neighbourhood [4]. In large-scale structure surveys, homogeneity up to 1% is only found at scales larger than  $\sim 100\text{Mpc}$  (e.g. [3, 5]). Thirdly, as a consequence of special relativity, two observers with a non-zero relative velocity observe their surroundings differently. Thus, the cosmological principle cannot hold for all observers. However, there should exist one reference frame, where homogeneity and isotropy apply. Hence, the cosmological principle can be meaningfully formulated as

*There exists a reference frame, where the universe is homogeneous and isotropic when averaged over large enough scales.*

A consequence of the cosmological principle is that the CMB and the large-scale structure in the universe share the same rest frame. If this was not the case, then there would not be a reference frame where both large-scale structure and CMB look isotropic, since both of them are affected by Doppler effects. The cosmological principle thus implies that we can infer our velocity with which we are moving with respect to the mean rest frame of distant galaxies from the velocity with which we are moving with respect to the CMB.

## 1.2 Cosmic Microwave Background Velocity

The CMB is found to be isotropic up to the level of  $\sim 10^{-5}$ . However, this is not the case on the largest scale, where an anisotropy of  $\sim 10^{-3}$  is observed (see Figure 1.1). This is the CMB dipole which is generally interpreted as the effect of our motion with respect to the surface of last scattering [8]. The Doppler shift of the frequencies leads to a boost of the temperature, so a moving observer with velocity  $v/c$  in units of the speed of light perceives the temperature  $T$  at an angle  $\theta$  to the direction of motion

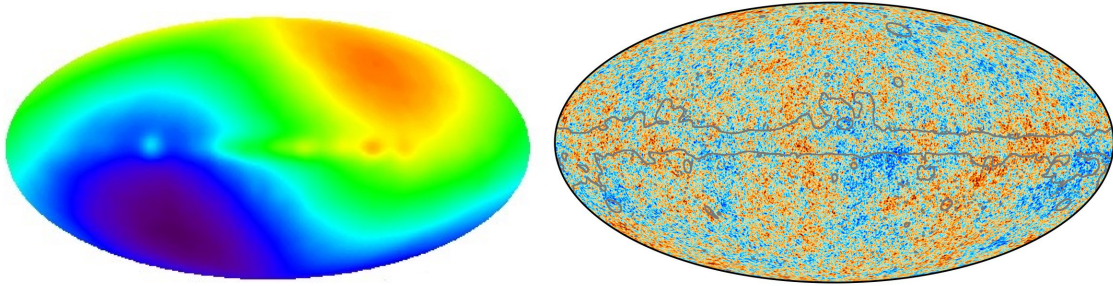


*Figure 1.1: Left:* The temperature sky map from 4-year DMR data of the COBE mission [6]. The maximum temperature fluctuations are  $\Delta T = \pm 3.353\text{mK}$  around the mean of  $2.73\text{K}$ . Credits: NASA and the COBE Science Team.

*Right:* The 2018 Planck map of the temperature anisotropies of the CMB [7] after removal of the dipole. The gray line shows the extent of the masked and inpainted region, mostly around the galactic plane. The maximum temperature fluctuation is  $\Delta T = \pm 300\mu\text{K}$ . Credits: ESA and the Planck Collaboration.

$T(\theta) \propto \sqrt{1 - v^2/c^2}/(1 - (v/c) \cos \theta)$ . The intrinsic CMB dipole in the standard model of cosmology is expected to be much smaller ( $\sim 10^{-5}$ ) and therefore typically neglected. Thus, our velocity  $\beta_{\text{CMB}} = v/c$  and the direction of our motion (here given in galactic coordinates  $(l, b)$ ) with respect to the CMB can be directly obtained from its dipole. A precise measurement by the Planck mission [7] yields

$$\begin{aligned} \beta_{\text{CMB}} &= (1.23357 \pm 0.00036) \times 10^{-3} \\ (l, b) &= (264.021 \pm 0.011, 48.253 \pm 0.005)^\circ, \end{aligned} \tag{1.1}$$

which corresponds to  $v = (369.82 \pm 0.11)\text{km/s}$ . To be more precise, ‘our motion’ means the motion of the Solar System barycenter. The motion of the Planck satellite around the Earth and Earth’s orbit around the Sun are extremely well known and not part of this result. To infer the velocity, the following assumption was used:

*The intrinsic CMB dipole is negligible and the observed CMB dipole is only caused by our motion with respect to the surface of last scattering.*

There is some evidence that this assumption is true. An analysis of the Doppler effects on smaller scale CMB fluctuations confirms the measurement of our velocity independently of the dipole [9]. However this measurement of  $\beta_{\text{CMB}}$  has an uncertainty of approximately 50%. It is thus by far not as good as the precision with which the dipole is measured.

As established in the previous section, a consequence of the cosmological principle is that the velocity found through the CMB dipole is also the one with which we are moving with respect to cosmic matter. Therefore, the velocity and direction from (1.1) determine the amplitude and direction of the kinematic contribution to the cosmic matter dipole. Hence, an analysis of the cosmic matter dipole tests two assumptions, the cosmological principle and the kinematic interpretation of the CMB dipole.

### 1.3 Previous Work

We give a short overview of the literature on the cosmic matter dipole and put this thesis into context. A first analysis [10] of the dipole in the distribution of radio sources has been performed with the NVSS [11] catalog, where consistency between data and theory was found. 9 years later, [12] finds a  $3\sigma$  discrepancy in the same data. In this and subsequent analyses, the direction is found to be consistent with the CMB dipole whereas the dipole amplitude clearly exceeds the expectations [13–20]. The dipole in the source distribution of several other surveys such as the 2MASS [21], 2MRS [22] in [13], the NVSS + SUMSS [23] in [17] and the TGSS [24] in [25] have also been analysed. In most of these studies, the excess of the dipole amplitude in the distribution of radio sources has been found to be significant at approximately  $2\text{--}3\sigma$ . A recent analysis of the SUMSS, WENSS [26], TGSS and NVSS radio sources dipoles and a compilation of different previous results is found in [20].

In this work, we first present the relevant theory of the cosmic matter dipole in Chapter 2, focusing on radio sources as a tracer of the matter distribution. In doing so, we present new aspects and methods to approach the topic, especially concerning the statistics of the expected dipole amplitude and direction.

Next, two data sets are examined, beginning with a detailed discussion of the dipole in the distribution of NVSS radio sources in Chapter 3 and continuing with a brief analysis of the dipole in a sample of quasars in Chapter 4. The latter is very interesting since in the recent publication [27] of the quasar sample and its dipole, a divergence from the assumptions of the cosmological principle and the exclusively kinematical interpretation of the CMB dipole is found at  $4.9\sigma$ .

With these two analyses, we find that the ignorance of the intrinsic dipole amplitude is the main systematic uncertainty. Similar conclusions have been drawn in [18] and [28]. Therefore, in Chapter 5, we go beyond the dipole in the number density and introduce a new method to analyse the cosmic matter dipole. To do so, we extend the idea of [15] by also including additional properties of the sources, such as their sizes or redshifts. This new method allows to distinguish the intrinsic clustering dipole and the kinematic dipole. We then forecast the new method’s potential in future large scale surveys. The results are summarized in Chapter 6.

---

We denote spatial three dimensional vectors as bold letters, e.g.  $\boldsymbol{\beta}$ . The amplitude of the vector is denoted by the letter itself, e.g.  $|\boldsymbol{\beta}| \equiv \beta$ , whereas its unit direction is indicated by a hat as in  $\boldsymbol{\beta}/\beta \equiv \hat{\boldsymbol{\beta}}$ . Throughout this work, we use approximate Planck values for the present day matter density, dark energy density and the Hubble constant,

$$\Omega_m = 0.31 \quad \Omega_\Lambda = 1 - \Omega_m \quad H_0 = 67.6 \text{ km/s/Mpc}, \quad (1.2)$$

and refer to the standard model of cosmology as the  $\Lambda$ CDM model with dark energy ( $\Lambda$ ) and Cold Dark Matter.

## 2 Theory of the Cosmic Matter Dipole

This chapter introduces all the relevant theory behind the cosmic matter dipole. In particular, we focus on the dipole in the distribution of radio sources, also referred to as the cosmic radio dipole. The results derived here can equally be applied to observations at other wavelengths. To start, let us briefly connect the observations with their final product, a catalog of radio sources (see descriptions in e.g. [11, 24]). A radio telescope measures the intensity of radiation in a frequency range from a direction  $\hat{\mathbf{n}}$ . This is the flux density  $S(\hat{\mathbf{n}}) = dE/d\Omega dA d\nu dt$ , the energy received per solid angle  $\Omega$ , per area of the telescope  $A$ , per frequency  $\nu$  and time  $t$ . From the flux density field, sources - meaning compact regions where the flux density clearly exceeds the background noise - are extracted with elaborate fitting methods (e.g. [11, 29, 30]). These sources can be different astronomical objects, typically different types of radio galaxies or star forming galaxies (see e.g. [11, 31, 32]). For the cosmic matter dipole, they are not distinguished and generally referred to as sources. For this chapter, only two properties of each source are considered. The first is the flux

$$F = \frac{dE}{dA d\nu dt}, \quad (2.1)$$

integrating the flux density over the angular extension of the source. Flux is measured in Jansky,  $1\text{Jy} = 10^{-26} \text{Wm}^{-2}\text{Hz}^{-1}$ . The second property is the position of the source, which is given by two coordinates, in short denoted by the direction  $\hat{\mathbf{n}}$ . Other observations of each source, such as its angular size are considered in Chapter 5.

From a list of the positions of all the radio sources, one can compute the number count density  $dN/d\Omega(\hat{\mathbf{n}})$ . Since no telescope is able to detect all sources, a lower flux limit  $F_{\min}$  is necessary, above which the survey is considered to be complete.

Finally, we are able to introduce the cosmic matter dipole as the dipole  $\mathbf{d}^N$  in the number density. To do so, we write the number density in the form

$$\frac{dN}{d\Omega}(> F_{\min}, \hat{\mathbf{n}}) = (1 + \mathbf{d}^N \cdot \hat{\mathbf{n}})\bar{N} + \mathcal{O}(n_j^2), \quad (2.2)$$

where  $\bar{N}$  is the average number density.  $\mathcal{O}(n_j^2)$  denotes the presence of higher multipoles such as the quadrupole, octopole, etc., which are ignored until Section 3.4. All the important concepts of the expansion in spherical harmonics, and its relation to multipoles and the dipole are found in Appendix A. The cosmic matter dipole is thus observed as the number density dipole or equivalently the dipole in the number counts. The true matter

distribution is of course not observable. Therefore, a tracer of it is needed. Here, the tracer is galaxies, or to be more exact, sources that are fitted to images of the sky.

There are three contributions to the number count dipole

$$\mathbf{d}^N = \mathbf{d}_{\text{kin}}^N + \mathbf{d}_{\text{int}} + \mathbf{d}_{\text{SN}}^N + \mathcal{O}(d^2), \quad (2.3)$$

the kinematic dipole due to our velocity with respect to the observed sources, the intrinsic dipole in the matter distribution and a shot noise dipole which is caused by the sources being a discrete sample of the true field. These three contributions are presented in detail in Sections 2.1, 2.2 and 2.3. The effect of incomplete sky coverage is discussed in Section 2.4. Section 2.5 explains how the three dipoles combine into one and Section 2.6 briefly discusses how to compare the expectations with an observation to characterize the agreement or disagreement between the two. Finally, an estimator to measure the dipole is presented in Section 2.7.

## 2.1 Kinematic Dipole

Starting from the assumption of isotropy, we concluded in the introduction that our Solar System is moving with respect to the observed sources at the velocity inferred by the CMB dipole. Assuming a purely kinematic interpretation of the CMB dipole, this velocity, denoted by the vector  $\boldsymbol{\beta}$  with amplitude and direction given in (1.1), is very precisely known. Hence, a clear prediction of the kinematic dipole in the number counts of galaxies can be made, which is derived in the first Section 2.1.1, following [33]. Afterwards, the equivalence between this expression and a fully general relativistic expression of the dipole [34] is shown.

### 2.1.1 Standard Derivation

Special relativity has two important consequences on the observation of radio sources of a moving observer. Firstly, as a result of a Lorentz transformation, the position of each source in its rest frame  $\hat{\mathbf{n}}_{\text{rest}}$  is aberrated to the observed position  $\hat{\mathbf{n}}$ . The angle  $\theta_{\text{rest}}$  between the direction of motion and the source position changes to the observed angle  $\theta = \arccos(\hat{\mathbf{n}} \cdot \hat{\boldsymbol{\beta}})$  by [35]

$$\cos \theta = \frac{\cos \theta_{\text{rest}} + \beta}{\beta \cos \theta_{\text{rest}} + 1}. \quad (2.4)$$

We denote observed quantities without any subscript, while quantities in the rest frame of the source are indicated so explicitly. From (2.4), we find the transformation of the solid angle element

$$\frac{d\Omega}{d\Omega_{\text{rest}}} = \delta(\hat{\mathbf{n}})^{-2}, \quad (2.5)$$

where we defined

$$\delta(\hat{\mathbf{n}}) = \frac{1 + \beta \cos \theta}{\sqrt{1 - \beta^2}} \approx (1 + \beta \cos \theta) + \mathcal{O}(\beta^2). \quad (2.6)$$

From (2.4), we see that each position is aberrated towards the direction of motion. Therefore, more sources are observed in the forward direction. (2.5) shows this equivalently and quantifies this effect. An area containing a fixed number of sources is perceived differently by a factor of  $\delta^{-2}(\hat{\mathbf{n}})$ . Hence, the observed number density is changed by  $\delta^2(\hat{\mathbf{n}})$ .

The second special relativistic consequence is the Doppler effect on the flux. To quantify this, we assume a power law behaviour in the frequency dependence of the source's flux and in the number density of sources with a flux larger than  $F_{\min}$

$$F \propto \nu^{-\alpha} \quad (2.7)$$

$$\frac{dN}{d\Omega}(> F_{\min}, \hat{\mathbf{n}}) \propto F_{\min}^{-x}. \quad (2.8)$$

If the telescope measures the flux in a small frequency band, a power law is a good fit for the dependence of the flux on the frequency. In fact, different sources have different values of the spectral index  $\alpha$ . However, using the average of these values is sufficient. Typically,  $\alpha = 0.75$  is assumed [33]. We will return to a more detailed discussion about the value of the spectral index for the sources observed in the NVSS in Section 3.2.2 as well as for the sample of quasars in Section 4.1. Concerning the power law in the cumulative number counts, the value of  $x$  can be fitted by the data and is typically  $x \approx 1$  (see Section 3.2.2). Most of the sources have a flux value close to  $F_{\min}$ , therefore, we are only interested in the behaviour of  $dN/d\Omega$  in a small region around  $F_{\min}$ , where a power law is a good fit.

The received flux is Doppler boosted by a factor of  $\delta(\hat{\mathbf{n}})$  as can be seen from (2.1), inserting  $dE/dE_{\text{rest}} = d\nu/d\nu_{\text{rest}} = \delta(\hat{\mathbf{n}})$  and  $dt/dt_{\text{rest}} = \delta^{-1}(\hat{\mathbf{n}})$ . Additionally, the Doppler shift of the observed frequency  $\nu = \delta(\hat{\mathbf{n}})\nu_{\text{rest}}$  also changes the received flux. In total, using the power-law (2.7), the observed flux is

$$F \propto \delta(\hat{\mathbf{n}})F_{\text{rest}} \left( \frac{\nu_{\text{rest}}}{\nu} \right)^{-\alpha} = \delta^{1+\alpha}(\hat{\mathbf{n}})F_{\text{rest}}. \quad (2.9)$$

Therefore, using (2.8), the number of sources observed is changed by  $\delta^{x(1+\alpha)}(\hat{\mathbf{n}})$ . Combining aberration and the Doppler effect, one finds

$$\frac{dN}{d\Omega}(> F_{\min}, \hat{\mathbf{n}}) = \frac{dN}{d\Omega_{\text{rest}}}(\hat{\mathbf{n}})\delta^{2+x(1+\alpha)}(\hat{\mathbf{n}}). \quad (2.10)$$

Ignoring any intrinsic anisotropy in the source distribution in the rest frame, which is studied in Section 2.2, we can write  $dN/d\Omega_{\text{rest}}(\hat{\mathbf{n}}) = \bar{N}$  and find to first order in  $\beta$

$$\frac{dN}{d\Omega}(> F_{\min}, \hat{\mathbf{n}}) = (1 + [2 + x(1 + \alpha)]\beta \cos \theta)\bar{N} + \mathcal{O}(\beta^2). \quad (2.11)$$

Here, one recognizes the kinematic dipole in the number counts, first derived in [33]

$$\mathbf{d}_{\text{kin}}^N = [2 + x(1 + \alpha)]\boldsymbol{\beta}. \quad (2.12)$$

Using typical values of  $x$  and  $\alpha$ , we can conclude that the amplitude of the kinematic dipole is

$$d_{\text{kin}}^N = [2 + (1 + \alpha)x]\beta \approx 3.75\beta \approx 4.6 \times 10^{-3}. \quad (2.13)$$

### 2.1.2 General Relativistic Derivation

So far, only special relativity has been used. Here, we explicitly show that a fully general relativistic expression of the kinematic dipole is equivalent to first order. We start with the formula for the general relativistic redshift dependent amplitude of the kinematic dipole in the observed galaxy distribution given in [34] (see also [36–38])

$$d_{\text{kin}}^N(z) = \left[ 3 + \frac{\dot{H}}{H^2} + (2 - 5s)\frac{1+z}{rH} - f_{\text{evo}} \right] \beta + \mathcal{O}(2) \quad (2.14)$$

with the evolution bias

$$f_{\text{evo}}(z, F) = -\frac{\partial \ln[(1+z)^{-3}\mathcal{N}(z, > F)]}{\partial \ln(1+z)} \quad (2.15)$$

and the magnification bias

$$s(\bar{z}, F) = \frac{\partial \log_{10} \mathcal{N}(\bar{z}, < m)}{\partial m} = -\frac{2}{5} \frac{\partial \ln \mathcal{N}(\bar{z}, > F)}{\partial \ln F}. \quad (2.16)$$

Only first order terms are included. A dot refers to a derivative with respect to physical time and  $r$  is the comoving radial distance.  $a = (1+z)^{-1}$  is the scale factor and  $H = \dot{a}/a$  the Hubble parameter.  $\mathcal{N}(z, > F) = \int_{L(z, F)}^{\infty} dL' n_s(z, L')$  is the background comoving number density of sources with flux exceeding  $F$ . It is given by integrating the luminosity function  $n_s(z, L')$  over the range of luminosities that are observed with a flux larger than  $F$ . A perfect flux-limited telescope would observe  $dN/d\Omega dz \equiv \bar{n}(z, > F) = (r^2 a^3 / H) \mathcal{N}(z, > F)$  sources per solid angle and per redshift. We rewrite the evolution bias in terms of  $\bar{n}$ , also making the dependence on the redshift explicit by introducing partial derivatives with respect to  $L$

$$f_{\text{evo}}(z, F) = \frac{\dot{H}}{H^2} + \frac{2}{arH} - \frac{\partial \ln \bar{n}(z, > F)}{\partial \ln(1+z)} \quad (2.17)$$

$$= \frac{\dot{H}}{H^2} + \frac{2}{arH} - \frac{d \ln \bar{n}(z, > F)}{d \ln(1+z)} + \frac{\partial \ln \bar{n}(z, > F)}{\partial \ln L} \frac{\partial \ln L}{\partial \ln(1+z)}. \quad (2.18)$$

One recognizes the magnification bias  $s(z) = -\frac{2}{5} \frac{\partial \ln \mathcal{N}}{\partial \ln L}$  since a derivative w.r.t. the logarithm of the flux is equal to one w.r.t. the logarithm of the luminosity [38]. A flux cut corresponds to a cut in luminosity, which depends explicitly on the redshift by [39, equation (B11)]

$$L(z) = 4\pi F(1+z)^{1+\alpha} r^2, \quad (2.19)$$

where a power-law in the frequency dependence of the luminosity  $L \propto \nu^{-\alpha}$  is assumed. We find the explicit redshift dependence of the luminosity

$$\frac{\partial L}{\partial \ln(1+z)} = \frac{2}{rHa} + (1+\alpha). \quad (2.20)$$

Using this equation in (2.18), we find for the dipole amplitude in (2.14)

$$d_{\text{kin}}^N(z) = \left[ 3 + x(1+\alpha) + \frac{d \ln \bar{n}(z, > F)}{d \ln(1+z)} \right] \beta. \quad (2.21)$$

Here, we reintroduced  $x$  from (2.8), which is related to the magnification bias by  $s = x/2.5$  (compare (2.8) to (2.16)). Averaging over the full redshift range, the dipole amplitude of the projected source density is

$$d_{\text{kin}}^N = \frac{1}{N} \int_0^\infty dz d_{\text{kin}}^N(z) \bar{n}(z, > F) = [2 + x(1+\alpha)] \beta. \quad (2.22)$$

This assumes that  $\langle \alpha(z)x(z) \rangle_z = \langle \alpha(z) \rangle_z \langle x(z) \rangle_z$ . It is used that  $n(z)$  as well as  $z \times n(z)$  vanish for both  $z \rightarrow 0$  and  $z \rightarrow \infty$ .  $N$  is the total number of sources,  $N = \int_0^\infty dz \bar{n}(z, > F)$ .

With this, we have found the equivalence of the special relativistic result for the kinematic dipole amplitude (2.13) of [33] and the corresponding general relativistic expression (2.14) of [34]. To be more precise, we have shown that there are no new leading order contributions from the fully general relativistic treatment of the kinematic dipole amplitude when averaged over the full redshift range. This short calculation can serve as a starting point for the inclusion of second order corrections to the kinematic dipole.

## 2.2 Intrinsic Dipole

The assumption of isotropy in the cosmological principle is a statistical one, meaning that no direction is expected to be preferred. However, each realization such as our observed universe deviates from isotropy. The standard model of cosmology describes and quantifies the expected deviations from isotropy by the angular power spectrum, denoted by the multipole coefficients  $C_l^{\text{int}}$ . In the following, we briefly show how these are related to the matter density fluctuations  $\delta_m$ , following [40].

The fluctuations in the source density  $dN/d\Omega_{\text{rest}}$  around its mean  $\bar{N} = \langle dN/d\Omega_{\text{rest}} \rangle$  are

$$\Delta(\hat{\mathbf{n}}) \equiv \frac{dN/d\Omega_{\text{rest}}(\hat{\mathbf{n}}) - \bar{N}}{\bar{N}}. \quad (2.23)$$

The fluctuations on the sky are related to the observable fluctuations in the source counts in three dimensional space  $\delta_s(\mathbf{r})$  by

$$\Delta(\hat{\mathbf{n}}) = \int_0^\infty dz n(z) \delta_s(\mathbf{r}(z)), \quad (2.24)$$

where we introduced the normalized redshift distribution  $n(z)$  of the sources.

The fluctuations on the sky can also be expressed in terms of spherical harmonics with coefficients (see also Appendix A.1)

$$a_{lm}^{\text{int}} = \int d\Omega Y_{lm}^*(\hat{\mathbf{n}}) \Delta(\hat{\mathbf{n}}). \quad (2.25)$$

The angular power spectrum is defined to be the variance of the spherical harmonic coefficients

$$C_l^{\text{int}} = \langle |a_{lm}^{\text{int}}|^2 \rangle. \quad (2.26)$$

Initial conditions and perturbation theory lead to an expression for the fluctuations  $\delta_m$  in the matter density. Neglecting perturbations (see discussion below),  $\delta_m$  can be related to the observable fluctuations in radio sources by the bias factor  $b$  [41].

$$\delta_s(\mathbf{r}) = b(z)\delta_m(\mathbf{r}). \quad (2.27)$$

We allow the bias to depend on the redshift  $z$ , but approximate it to be scale independent.

We rewrite  $\delta_m(\mathbf{r}) = \delta_m(\mathbf{r}, z=0)D_+(z)$ , introducing the growth factor  $D_+(z)$ , which characterizes the growth of structure over time. We also use the Fourier transformation  $\delta_m(\mathbf{r}, z=0) = \int dk^3/(2\pi)^3 \exp(i\mathbf{k} \cdot \mathbf{r})\delta_m(\mathbf{k})$  of the matter density fluctuations at  $z=0$  and the power spectrum  $P(k, z=0)$ , defined by  $\langle \delta_m(\mathbf{k})\delta_m(\mathbf{k}') \rangle = \delta^{(3)}(\mathbf{k} - \mathbf{k}') (2\pi)^3 P(k, z=0)$ . The Dirac-delta distribution  $\delta^{(3)}$  is a consequence of homogeneity and isotropy [42].

Collecting all these expressions and using the identity (A.5), we find for (2.26)

$$C_l^{\text{int}} = \frac{2}{\pi} \int_0^\infty dk k^2 P(k, z=0) W_l^2(k), \quad (2.28)$$

$$W_l(k) = \int_0^\infty dz n(z) b(z) D(z) j_l(kr(z)), \quad (2.29)$$

where the spherical Bessel function  $j_l$  is used. This is the relation between the amplitude of density fluctuations on different scales  $k$  which is characterized by the power spectrum and the amplitude of fluctuations in the density on the sky on different scales  $l$  characterized by the angular power spectrum.

In fact, (2.27) is only an approximation to the fluctuations in the source counts. Various other effects such as redshift space distortions, lensing and distortions due to gravitational potentials influence the relation between the observed fluctuations in the source counts and the matter density fluctuations [36, 37] (see also [42]). Since the purpose of this section is only to show how fluctuations in the matter field are related to anisotropies in the distribution of galaxies, we do not discuss these effects here. Only the redshift space distortions (RSD) are addressed since these have a sizeable effect on large scales and are thus relevant for the dipole.

For all calculations throughout this work, we use the full expression of the angular power spectrum. This is done with the public code CLASS [43] modified to CLASSgal [38] which includes all perturbations to the angular power spectrum. We give some intuition about

the perturbations in Figure B.1, where we show how different effects modify the angular power spectrum.

In this section, we only show how the most important effect on large scales, the RSD, enter the expression for the angular power spectrum. To do so, we follow [42]. The approximation (2.27) is extended to include perturbations of the volume element

$$\delta_s = b(z)\delta_m + \frac{\delta V}{V}. \quad (2.30)$$

The volume element is

$$V = r^2(z)d\Omega dr = r^2(z)d\Omega \frac{dr}{dz} dz. \quad (2.31)$$

The observed volume element is perturbed through different effects. One of them originates in the peculiar velocity of the sources  $\mathbf{V}_p$ . The background redshift  $\bar{z}$  which is related to the distance  $r(\bar{z}) = \int_0^{\bar{z}} dz'/H(z')$ , where  $H = \dot{a}/a$  is the Hubble parameter and  $a = 1/(1 + \bar{z})$  is the scale factor, is not directly observable. Instead it is changed due to the Doppler effect to

$$z = \bar{z} + \delta z = \bar{z} + (1 + \bar{z})\mathbf{V}_p \cdot \hat{\mathbf{n}}. \quad (2.32)$$

An observer does not measure the background redshift indicating the distance but the perturbed redshift. Inserting (2.32) into the derivative in (2.31), one finds (see Equation (8.7) and (8.8) in [42])

$$\frac{\delta V}{V} = \mathbf{V}_p \cdot \hat{\mathbf{n}} + \frac{1 + \bar{z}}{H} \frac{d\mathbf{V}_p \cdot \hat{\mathbf{n}}}{dr}. \quad (2.33)$$

These two terms influence the observed fluctuations through (2.30). The second term dominates over the first one on small scales since then,  $H^{-1}d/dr \propto k/H$  is large. It is referred to as the RSD. Numerical calculations with CLASS show that the RSD have the largest effect on large scales after the density fluctuations  $\delta_m$  themselves (see Figure B.1).

Finally, we can discuss the intrinsic dipole amplitude  $d_{\text{int}}$ . The  $\Lambda$ CDM model only predicts the multipole coefficient  $C_1^{\text{int}}$ , which we have calculated above. The amplitude of the intrinsic dipole itself is not exactly predicted. As a consequence of isotropy there is also no preferred direction. Instead, the dipole is expected to point in a completely random direction. The  $C_l^{\text{int}}$  is related to the variance of the dipole amplitude by (A.15)

$$\langle d_{\text{int}}^2 \rangle = \frac{9C_1^{\text{int}}}{4\pi}. \quad (2.34)$$

The dipole amplitude that we observe is expected to be a random variable following a  $\chi(3)$  distribution (A.17) (see discussion in Appendix A.3).

We call  $d_{\text{int}} = \sqrt{9C_1^{\text{int}}/(4\pi)}$  the typical dipole amplitude. Its value is displayed for different  $C_1^{\text{int}}$  in Figure 2.1. For the calculation of the  $C_1^{\text{int}}$ , different tophat windows as the redshift distribution are used, so sources have equal probability to be observed between  $z_{\text{min}}$  and  $z_{\text{max}}$  and zero probability otherwise (in fact, this window is slightly smoothed to avoid artefacts from numerical integration).

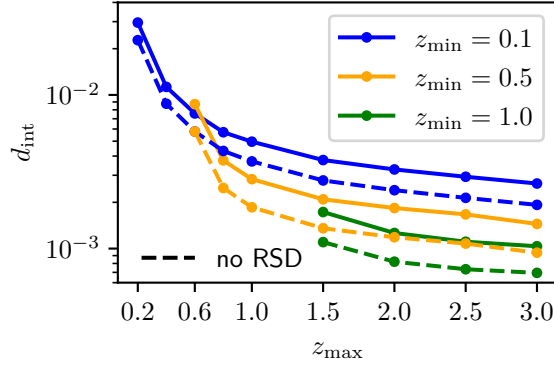


Figure 2.1: The intrinsic dipole  $d_{\text{int}} = \sqrt{9C_1^{\text{int}}/(4\pi)}$  of galaxy number counts as expected in the  $\Lambda$ CDM model. A smoothed tophat window between different  $z_{\text{min}}$  and  $z_{\text{max}}$  is used for the calculation with CLASS. The magnification bias is set to  $s = 0$  and the bias to  $b = 1.5$ . For comparison, the kinematic dipole amplitude is approximately  $5 \times 10^{-3}$ .

In Figure 2.1, one can see that the closer the sources and the smaller the bin, the larger the intrinsic dipole. This is why cosmic sources distributed over large distances are most interesting for the dipole analysis. There, anisotropies are expected to be smallest.

In this work, different surveys will be considered. Depending on their redshift distribution, we will find different typical intrinsic dipole amplitudes, ranging between

$$d_{\text{int}} \sim (0.5\text{--}5) \times 10^{-3}. \quad (2.35)$$

## 2.3 Shot Noise

The third contribution to the cosmic dipole is a natural consequence of measuring point sources. Point sources are a random discrete sample of the underlying field. Thus, the field can be inferred precisely only in the limit of observing  $N \rightarrow \infty$  sources. Since we are limited to a finite number of sources, we analyse the effect of shot noise (also Poissonian noise) on the number count dipole. In this section, shot noise on a full sky coverage is discussed (see also [14, 44]). In Section 2.4, the effect of a partial sky coverage is considered.

Let us consider a field of  $N$  point sources whose positions  $\hat{\mathbf{n}}_i$  are random and independent following an isotropic distribution

$$f(\hat{\mathbf{n}}) = \sum_i^N \delta^{(2)}(\hat{\mathbf{n}} - \hat{\mathbf{n}}_i), \quad (2.36)$$

where  $\delta^{(2)}$  is the Dirac-delta distribution. The underlying distribution is perfectly isotropic and its angular power spectrum vanishes naturally. For the field that consists of a sample,

however, this is not the case as we will show. To do so, we calculate the angular power spectrum of  $f(\hat{\mathbf{n}})$  following Appendix A. The spherical harmonic coefficients (A.1) are

$$a_{lm} = \frac{1}{\bar{N}} \sum_i^N Y_{lm}(\hat{\mathbf{n}}_i). \quad (2.37)$$

The prefactor  $1/\bar{N}$ , where  $\bar{N} = N/4\pi$  is the mean source density, ensures the convention used throughout this work. That is, spherical harmonic coefficients, the dipole (compare to (2.2)) and the multipoles  $C_l$  all characterize the fluctuations relative to the field. The multipoles are (A.8)

$$\begin{aligned} C_l^{\text{SN}} &= \frac{1}{\bar{N}^2} \frac{1}{2l+1} \sum_{m=-l}^l \sum_{i,j}^N \langle Y_{lm}(\hat{\mathbf{n}}_i) Y_{lm}^*(\hat{\mathbf{n}}_j) \rangle \\ &= \frac{1}{\bar{N}^2} \frac{1}{2l+1} \sum_{m=-l}^l \left( \sum_i^N \langle |Y_{lm}(\hat{\mathbf{n}}_i)|^2 \rangle + \sum_{i \neq j}^N \langle Y_{lm}(\hat{\mathbf{n}}_i) Y_{lm}^*(\hat{\mathbf{n}}_j) \rangle \right) \\ &= \begin{cases} 1/\bar{N} & , l > 0 \\ 4\pi & , l = 0. \end{cases} \end{aligned} \quad (2.38)$$

Here, we used (A.3) as well as (A.4) and identified the ensemble average in (A.8) as the average of over all sources' possible positions,  $\langle \dots \rangle = \int d\Omega_i \int d\Omega_j / (4\pi)^2 \dots$

We find that the shot noise power spectrum is non-vanishing and constant

$$C_l^{\text{SN}} = 1/\bar{N}, \quad l \geq 1. \quad (2.39)$$

In the limit of  $N \rightarrow \infty$ , the field would be perfectly sampled and the shot noise angular power spectrum vanishes. As explained in Appendix A.3, the shot noise dipole amplitude is random and follows a  $\chi(3)$ -distribution similar to the intrinsic dipole amplitude. From (A.15), we see that the typical shot noise dipole (still on the full sky) is

$$d_{\text{SN}}^N = \sqrt{\frac{9C_1^{\text{SN}}}{4\pi}} = \frac{3}{\sqrt{N}}. \quad (2.40)$$

For  $10^6$  sources this is  $3 \times 10^{-3}$  and therefore comparable to both the kinematic dipole (2.13) and the intrinsic dipole (2.35).

So far, we have only discussed the intrinsic dipole and the shot noise dipole on the full sky. In the next session, the effect of an incomplete sky coverage on these two dipole is discussed.

## 2.4 Effect of Incomplete Sky Coverage

It is very difficult to observe the full sky. Earth-based telescopes are often not able to see the a north or south region since it is blocked by the Earth. Even for space-based

telescopes, the view into the cosmic distance is partially blocked by the Milky Way. Often, a mask is constructed that covers regions which are not observed or that are known to be noisy (see Section 3.1.2). The part of the sky which is not observed or not taken into the analysis for other reasons is therefore also called the masked region. In this section, we will discuss how an incomplete sky coverage complicates matters and show how the results derived in the previous two sections for a full sky coverage can nevertheless serve as an approximation if a part of the the sky is masked.

To begin, let us consider a quadrupole field with  $l = 2$ ,  $m = 0$ ,  $f(\hat{\mathbf{n}}) \propto \cos^2 \delta$ , which is only observed on the northern half of the sky, i.e. with declination  $\delta > 0$ . The southern hemisphere is masked. Therefore, we only see a maximum at the north pole and a decreasing value of the field towards the equator. To an observer not knowing that the field is mirrored on the southern hemisphere, this resembles a dipole. The dipole estimator used in this work fits a dipole to the observed field. The best fit model in this case would not be a vanishing dipole, but a dipole pointing towards the north. This example shows how fluctuations on smaller scales than the dipole can look like a dipole on a masked sky. We call this the leakage effect.

Since a mask in general breaks the spherical symmetry, it is intuitive that the leakage also changes the distribution of random dipoles. On the full sky, the dipole direction of both the shot noise dipole and the intrinsic dipole is random following an isotropic distribution. The probability density functions (PDFs) of the dipole's declination  $\delta$  and right ascension  $\alpha$  are

$$P(\delta) = (\sin \delta)/2, \quad P(\alpha) = 1/(2\pi). \quad (2.41)$$

On a masked sky, this is not necessarily the case because of leakage from higher intrinsic multipoles to the intrinsic dipole and leakage from higher shot noise multipoles to the shot noise dipole. To summarize, the leakage can change both the distribution of dipole amplitudes and the distribution of directions.

To illustrate this, we begin with a discussion of the shot noise dipole. To do so we fix the total number of observed sources  $N_{\text{tot}}$  and let  $\bar{N} = N_{\text{tot}}/(4\pi f_{\text{sky}})$  vary with the observed fraction of the sky  $f_{\text{sky}}$ . This means a smaller  $f_{\text{sky}}$  corresponds to a larger number density and thus a smaller shot noise angular power spectrum  $C_l^{\text{SN}} = 1/\bar{N}$ . On the other hand, we anticipate that the leakage increases with decreasing  $f_{\text{sky}}$ .

We test these two opposing effects for three simple example masks, displayed in Figure 2.2. The Tetrad Mask covers all of the sky except for four small regions (1/48 of the sky each) that are separated as far as possible from one another. These four regions correspond to the the four corners of a tetrahedron inscribed in a sphere, which motivates the name Tetra Mask. The Half Mask covers half of the sky ( $\alpha \in [0, \pi]$ ). This is an interesting scenario, since many earth-based telescopes only observe the sky above or below a certain declination (see for example the NVSS mask in Figure 3.4 or the LSST mask in Figure 5.2). Here we rotate such a mask by  $90^\circ$  for a better visualisation of the results. A third test is done with the Quad Mask, where two distinct quarters of the sky are not masked (resembling the  $m = 0$  quadrupole, hence the name). This mask is motivated by the one used in the quasar analysis (see Figure 4.1).

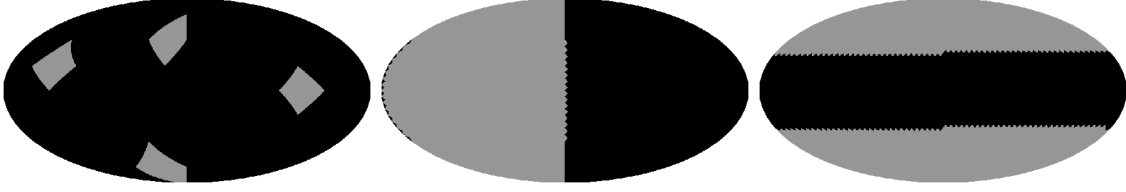


Figure 2.2: From left to right: Mollweide projection of the Tetrads, Half and Quad masks with sky coverages of 8%, 50% and 50%, respectively. Grey indicates the observable regions and black the masked regions.

The middle of the plot corresponds to zero right ascension and zero declination. Declination increases towards the top and decreases towards the bottom. Right ascension increases towards the left. Note that in this projection of the sky, any point on the left is neighbouring the point on the right with the same declination.

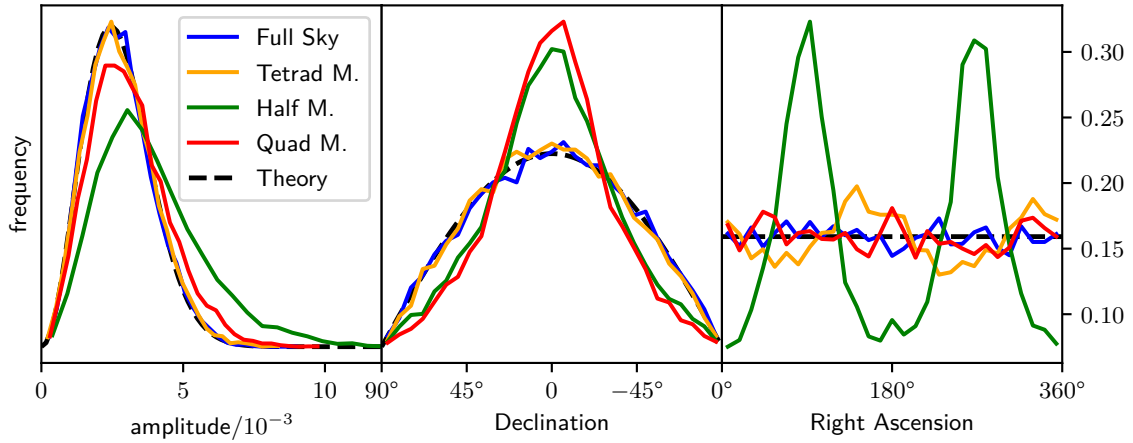


Figure 2.3: Comparison of the distributions of amplitude, declination and right ascension of the shot noise dipole for different sky coverages (see Figure 2.2). The obtain these, shot noise simulations are used (see Appendix A.2), where the number of sources  $N_{\text{tot}} = 10^6$  is the same in the observable region, i.e. the source density is not equal for the different sky coverages. The theory curve is a  $\chi(3)$  distribution with  $\langle d^2 \rangle = 3 \times 10^{-3}$  for the amplitude  $d$ ,  $(\sin \delta)/2$  for the declination  $\delta$  and  $1/(2\pi)$  for the right ascension.

The distributions of random shot noise dipole amplitudes and directions are tested by simulations. For each of the three masks as well as for the full sky, we simulate the shot noise of  $N_{\text{tot}} = 10^6$  sources distributed on the unmasked regions following Appendix A.2. The source density  $\bar{N} = N_{\text{tot}}/(4\pi f_{\text{sky}})$  is larger for smaller sky coverages. We then measure the dipole in the shot noise field using the estimator described in Section 2.7, which is not biased due to incomplete sky coverage. Any directional biases that we observe are the result of the shot noise dipole and not the estimator. The distribution of dipole amplitudes and directions found in 10 000 simulations is shown in Figure 2.3 and discussed in the following.

First, the full sky distribution of the amplitudes agrees perfectly with the theory, which is a  $\chi(3)$  distribution (see Appendix A.3) with typical amplitude (2.40)  $d_{\text{SN}}^N = 3/\sqrt{N_{\text{tot}}}$ . Also, the random directions agree with the isotropic PDFs (2.41).

We continue to discuss the results of the partial sky coverages. We notice that the resulting distribution of amplitudes of the Tetrads Mask is very similar to the full sky one.

This is because on this particular mask, the increasing number density exactly cancels the increasing leakage for smaller sky coverages. It is remarkable that the distributions of amplitudes and directions of shot noise dipoles found when applying the Tetrad Mask, where  $f_{\text{sky}} = 1/12$ , are nearly the same as the ones where the same number of sources is distributed on the full sky instead of the four small patches.

This is not the case for both the Quad Mask and the Half Mask. There, we find that the amplitudes are larger and the direction is biased. Hence, we conclude that directional bias and the amplitude of shot noise on a masked sky do not necessarily correlate with the fraction of the observed sky, when the total number of sources is fixed.

In the middle and right panels of Figure 2.3, we see how the Quad and Half Masks change the isotropic distribution. The random dipoles in the Half Mask tend to point towards the center of the masked region or in the opposite direction, which corresponds to a right ascension of  $90^\circ$  or  $270^\circ$  and zero declination. The sky coverage of the Quad Mask covers the full range of the right ascension for the observed declination range. Therefore, there is only a bias in the declination. Due to the special symmetry of this mask, a random quadrupole has no effect on the dipole. Only an octopole or larger multipoles can induce dipole leakage. The absence of leakage from the quadrupole explains why the distribution of amplitudes from the Quad Mask follows the full sky distribution more closely than the amplitude distribution of the Half Mask.

By inspecting the amplitude distributions in Figure 2.3, we find that the leakage increases the typically observed shot noise dipole only slightly, if the same number of sources is distributed in the observed region. Therefore, we state that the shot noise dipole power observed on a reasonably masked sky  $\tilde{C}_1^{\text{SN}}$  is related to the shot noise dipole power with the same number density on the full sky  $C_1^{\text{SN}}$  by

$$\tilde{C}_1^{\text{SN}} = C_1^{\text{SN}} + \text{leakage} \gtrsim C_1^{\text{SN}}/f_{\text{sky}} = 4\pi/N_{\text{tot}}. \quad (2.42)$$

‘Reasonable’ means either a sky coverage of  $f_{\text{sky}} > 50\%$  or a mask like the Tetrad Mask, where very distinct directions are observed. It is important to observe at least four distinct directions since four parameters need to be estimated, the monopole and the three dipole components. If we observed less than four small patches, the shot noise dipole amplitudes and directional biases would be found to be much larger.

Having discussed the shot noise leakage, we continue with the leakage of the intrinsic clustering. Similar to the result (2.42), we approximate the dipole power expected on the masked sky  $\tilde{C}_1^{\text{int}}$  by the dipole power in the full sky angular power spectrum  $C_1^{\text{int}}$  as

$$\tilde{C}_1^{\text{int}} = C_1^{\text{int}} + \text{leakage} \gtrsim C_1^{\text{int}}/f_{\text{sky}}. \quad (2.43)$$

Here, we rely on the angular power spectrum being relatively smooth, i.e. higher multipoles are of the same order as the dipole power  $C_1^{\text{int}}$ , which is usually the case (compare for example to Figure 3.5).

In writing (2.42) and (2.43), i.e. replacing the full sky dipole power with a larger dipole power on the masked sky, we neglect any directional bias through leakage. Also, these two

expressions are by far not accurate but rather serve as a rule of thumb how the typical intrinsic dipole amplitude depends on the sky coverage

$$d_{\text{int}} \gtrsim \sqrt{\frac{9C_1^{\text{int}}}{4\pi f_{\text{sky}}}} \quad (2.44)$$

as well as that the typical shot noise dipole amplitude is better specified by the total number of sources than the number density

$$d_{\text{SN}}^N \gtrsim \sqrt{\frac{9}{N_{\text{tot}}}}. \quad (2.45)$$

In order to be exact when comparing the expectations of the cosmic matter dipole to the distribution of observed sources, we use simulations with the same survey sky coverage.

In the next section, when discussing how the different parts of number count dipole combine, we use (2.42) and (2.43) as an approximation, such that the results also serve as an approximation for incomplete sky coverages.

## 2.5 Combined Dipole

We established the three contributions of the number count dipole

$$\mathbf{d}^N = \mathbf{d}_{\text{kin}}^N + \mathbf{d}_{\text{int}} + \mathbf{d}_{\text{SN}}^N. \quad (2.46)$$

Since we only observe the total number count dipole  $\mathbf{d}^N$  and want to compare it to expectations from the  $\Lambda$ CDM model, in this section, we discuss how the kinematic dipole combines with the two random dipoles. This is non-trivial because we cannot simply add the amplitudes of the contributions  $d_{\text{kin}}^N$ ,  $d_{\text{int}}$  and  $d_{\text{SN}}^N$  found in the previous sections but have to consider their directions. In the following the probability density functions (PDFs) for amplitude and direction of the dipole are derived. Additionally, we give the formulas for the mean and standard deviation that can be inferred from the PDFs.

As described in Section 2.2 and Section 2.3, both the intrinsic clustering and the scatter due to shot noise are characterized by the angular power spectrum. In particular, for the dipole we only need the respective first multipoles  $C_1^{\text{int}}$  and  $C_1^{\text{SN}}$ , if we consider a full sky coverage. As discussed in Section 2.4, when dealing with a partial sky coverage, there is leakage from higher multipoles, so we use  $\tilde{C}_1^{\text{int}}$  and  $\tilde{C}_1^{\text{SN}}$  as an approximation (see (2.42) and (2.43)). Doing so, we ignore biases in the random dipole direction. The results therefore only hold for the full sky, but also serve as an approximation for partial sky coverages with  $f_{\text{sky}} > 50\%$ .

In Appendix A.3, it is shown that the components of both random dipoles can be described by independent Gaussian variables with zero mean and variance  $3C_1/(4\pi)$ , see (A.16). The vanishing mean is a consequence of isotropy. The variance follows from the definition of the multipoles  $C_l \equiv \langle |a_{lm}|^2 \rangle$ . In the case of the intrinsic clustering, nonlinearities are small on large scales (compare to Figure B.1), so a Gaussian distribution of

the  $a_{lm}$  is a good approximation. For the shot noise, which follows a Poissonian distribution, it is safe to invoke the central limit theorem since we are interested on the large scale distribution of many sources  $N_{\text{tot}} > 10^5$ . Therefore, fluctuations in the number density can also be considered as Gaussian.

In summary, the dipole components of the shot noise and the intrinsic clustering dipole are well described as normally distributed independent variables with zero mean and variance

$$\sigma_{\text{SN}}^2 = \frac{3\tilde{C}_1^{\text{SN}}}{4\pi} = \frac{3}{N_{\text{tot}}} \quad (2.47)$$

$$\sigma_{\text{int}}^2 = \frac{3\tilde{C}_1^{\text{int}}}{4\pi} = \frac{3C_1^{\text{int}}}{4\pi f_{\text{sky}}}, \quad (2.48)$$

respectively. This is exact for  $f_{\text{sky}} = 1$  and an approximation otherwise.

### PDF of Amplitude and Deviation Angle

Before including the kinematic dipole, we first combine the two dipoles from intrinsic clustering and shot noise into one random dipole, denoted as  $\mathbf{d}_r = \mathbf{d}_{\text{SN}}^N + \mathbf{d}_{\text{int}}^N$ . Its components are also normal variables with zero mean and variance

$$\sigma_r^2 = \sigma_{\text{SN}}^2 + \sigma_{\text{int}}^2. \quad (2.49)$$

The random dipole amplitude is distributed accordingly to a  $\chi(3)$ -distribution (A.17)

$$P(d_r) = \frac{d_r^2}{\sigma_r^3} \exp\left(-\frac{d_r^2}{2\sigma_r^2}\right) \sqrt{\frac{2}{\pi}} \quad (2.50)$$

(for a visualisation, see ‘Theory’ in the left panel of Figure 2.3 where  $\sigma_r^2 = 3 \times 10^{-6}$ ). Since we assume a full sky coverage, the random dipole’s direction follows an isotropic distribution, just like its two constituents, the intrinsic and the shot noise dipole. Instead of considering both the declination and right ascension, we can describe its direction by the angle  $\theta_r$  relative to the kinematic dipole, where  $\cos \theta_r = \hat{\mathbf{d}}_{\text{kin}} \cdot \hat{\mathbf{d}}_r$  (for readability, we drop the superscript  $N$  of the kinematic number count dipole in the remainder of this section). There is no preferred direction of the random dipole, hence

$$P(\cos \theta_r) = 1/2. \quad (2.51)$$

To specify the direction of the combined dipole  $\mathbf{d} = \mathbf{d}_{\text{kin}} + \mathbf{d}_r$ , we define the deviation angle  $\theta$  between the kinematic dipole and the combined dipole

$$\cos \theta = \hat{\mathbf{d}}_{\text{kin}} \cdot \hat{\mathbf{d}} = (d_r \cos \theta_r + d_{\text{kin}})/d. \quad (2.52)$$

Since the only special direction is defined by the kinematic dipole, it is sufficient to consider only the deviation angle. The amplitude of the combined dipole is

$$d = \sqrt{d_r^2 + d_{\text{kin}}^2 + 2d_r d_{\text{kin}} \cos \theta_r}, \quad (2.53)$$

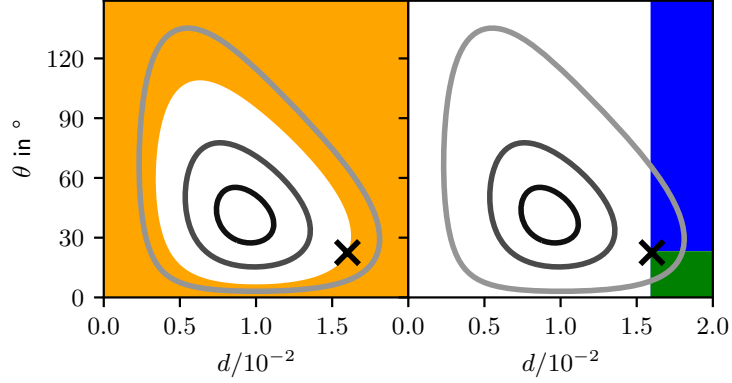


Figure 2.4: In both panels, the contour lines show where the PDF  $P(d, \theta)$  of dipole amplitudes  $d$  and deviation angles  $\theta$  is 90%, 60% and 13% of its maximum. The cross marks the example discussed in the main text of  $d_{\text{obs}} = 0.016$  and  $\theta_{\text{obs}} = \pi/8$ .

Left: The orange region shows all values, which occur with a probability smaller than the probability of the example dipole and deviation angle.

Right: The blue and green region together show all values with an amplitude larger than the observed one. The green region shows all the outcomes with an amplitude larger and a deviation angle smaller than the example dipole and deviation angle.

Using (2.50) to (2.53), we find for the PDF of combined dipole amplitude and deviation angle

$$\begin{aligned}
 P(d, \theta) &= \sin \theta P(d_r) P(\cos \theta_r) \left| \frac{d(d_r, \cos \theta_r)}{d(d, \cos \theta)} \right| = \sin \theta P(d_r) P(\cos \theta_r) \frac{d^2}{d_r^2} = \\
 &= \sin \theta \frac{d^2}{\sigma_r^3} \exp \left( - \frac{d^2 + d_{\text{kin}}^2 - 2 \cos \theta d d_{\text{kin}}}{2\sigma_r^2} \right) \sqrt{\frac{1}{2\pi}}.
 \end{aligned} \tag{2.54}$$

To give some intuition about this result, Figure 2.4 displays  $P(d, \theta)$  with  $d_{\text{kin}} = \sigma_r = 0.005$  (the colored regions in this figure will be relevant in the next section). These values are motivated by the data analysis in Section 3.2. It is clearly visible that the resulting dipole is not expected to point exactly in the direction of the kinematic dipole, but rather at some angle  $\theta \approx \pi/4$ . Also, the amplitude is biased to larger values  $d \approx 0.01$  than the kinematic amplitude. This bias immediately follows from (2.53). If the random dipole which consists of shot noise and intrinsic dipole points in the same direction as the kinematic dipole, then the resulting amplitude is larger. On the other hand, if the random dipole points in the opposite direction, the resulting dipole amplitude is smaller. This explains the anti-correlation between amplitude and deviation angle that can be seen in Figure 2.4.

### PDF, Mean and Variance of the Dipole Amplitude

Let us define the coordinate system for this section in such a way that the kinematic dipole points in the  $z$ -direction. The components of the random dipole are normally

distributed with zero mean. The components of the combined dipole, however, also include the kinematic dipole. Therefore, the mean of the  $z$ -component is not zero

$$d_{x,y} \sim \mathcal{N}(0, \sigma_r^2), \quad d_z \sim \mathcal{N}(d_{\text{kin}}, \sigma_r^2). \quad (2.55)$$

The PDF  $P(d)$  of the combined dipole's amplitude  $d = \sqrt{d_x^2 + d_y^2 + d_z^2}$  is the non-central  $\chi(3)$ -distribution, being displaced by the kinematic dipole amplitude in comparison to the central  $\chi(3)$ -distribution. It can be expressed as [45]

$$P(d) = \sqrt{\frac{2}{\pi}} \frac{d}{d_{\text{kin}} \sigma_r} \exp\left(-\frac{d^2 + d_{\text{kin}}^2}{2\sigma_r^2}\right) \sinh(d_{\text{kin}} d / \sigma_r^2). \quad (2.56)$$

Integrating (2.54) over all  $\theta$  also gives this result,  $\int d\theta P(d, \theta) = P(d)$ . In the limit  $d_{\text{kin}} \rightarrow 0$  the non-central  $\chi(3)$ -distribution (2.56) reduces to central one (2.50) using  $\lim_{x \rightarrow 0} \sinh(ax)/x = a$ .

The mean and the variance of  $d$  can be computed [45, 46] and expressed with the associated Laguerre function  $L$  as

$$\begin{aligned} \langle d \rangle &= \sigma_r \sqrt{\frac{\pi}{2}} L_{1/2}^{1/2}\left(-\frac{d_{\text{kin}}^2}{2\sigma_r^2}\right) \approx \sqrt{8\sigma_r^2/\pi + d_{\text{kin}}^2} \\ \sigma_d^2 &= 3\sigma_r^2 + d_{\text{kin}}^2 - \langle d \rangle^2 \sim 0.4\sigma_r^2. \end{aligned} \quad (2.57)$$

The approximation in the first line is motivated by the fact that the random dipole alone has an expected amplitude of  $\langle d_r \rangle = \sigma_r \sqrt{\pi/2} L_{1/2}^{1/2}(0) = \sigma_r \sqrt{8/\pi}$ . The naive approach of  $\langle d \rangle \approx \sqrt{\langle d_r \rangle^2 + d_{\text{kin}}^2}$  turns out to be a good approximation and is accurate for all  $\sigma_r, d_{\text{kin}} < 0.1$  within 3%. The approximation in the second line of (2.57), however, can be arbitrarily bad as it concerns the difference between two larger numbers. Throughout this work, we use the exact results in (2.57).

### Mean and Variance of the Deviation Angle

One can integrate  $P(d, \theta)$  over all  $d$  to find the PDF of the deviation angle  $P(\theta) = \int dd P(d, \theta)$ . However, the resulting analytic expression is lengthy and therefore not stated here. Instead, we directly skip to the mean and variance of  $\theta$ . They can be computed numerically like

$$\begin{aligned} \langle \theta \rangle &= \frac{1}{2} \int_{-1}^1 d \cos \theta_r \int_0^\infty dd_r P(d_r) \theta \\ \sigma_\theta^2 &= \frac{1}{2} \int_{-1}^1 d \cos \theta_r \int_0^\infty dd_r P(d_r) (\theta - \langle \theta \rangle)^2. \end{aligned} \quad (2.58)$$

There is no analytic expression available for these two integrals.

### Conclusion

To give some intuition about the results (2.57) and (2.58), we show the mean and variance of the combined dipole amplitude and the deviation angle in Figure 2.5. Additionally, we compare these results to simulations. To do so, we use the methods described in Appendix A.2, which include the intrinsic clustering and shot noise. Also a kinematic

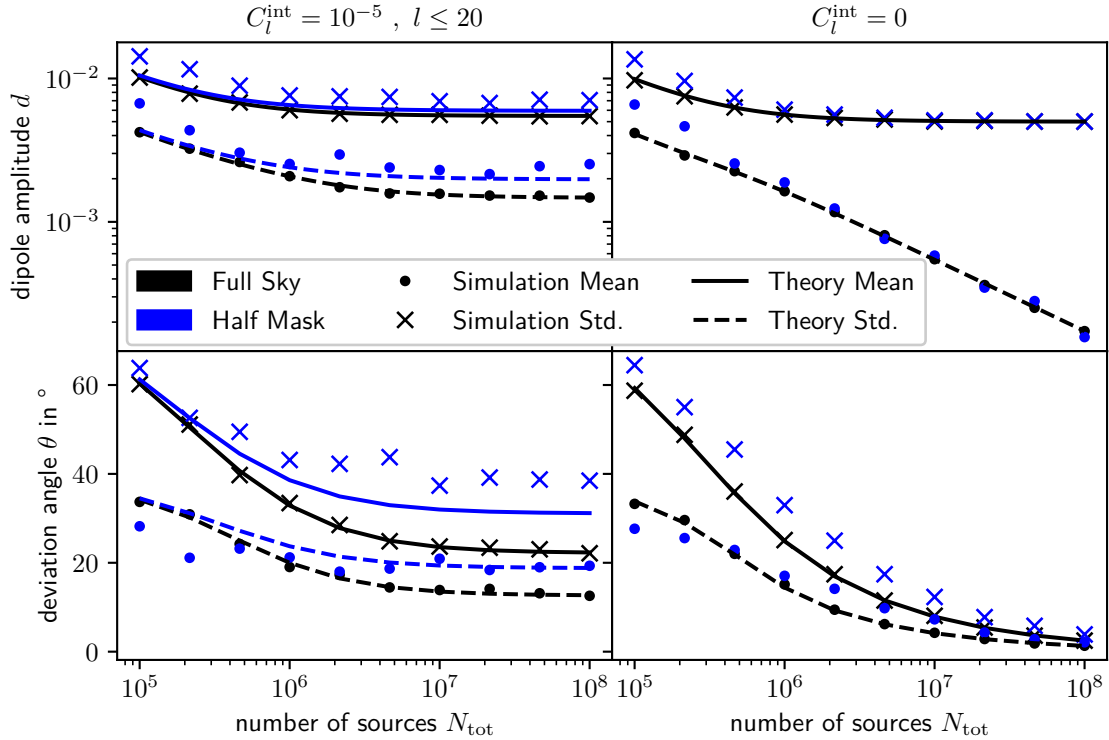


Figure 2.5: Comparison of the theoretical results (2.57) and (2.58) for mean and standard deviation of the combined dipole’s amplitude  $d$  and deviation angle  $\theta = \arccos \hat{\mathbf{d}}_{\text{kin}} \cdot \hat{\mathbf{d}}$  with simulations for different number of sources  $N_{\text{tot}}$ . The kinematic dipole is included pointing towards declination  $\delta = 90^\circ$  with an amplitude  $d_{\text{kin}} = 5 \times 10^{-3}$ . Only in the left column, intrinsic clustering is included with  $C_l^{\text{int}} = 10^{-5}$  for  $l \leq 20$  and zero otherwise. The Half Mask is displayed in Figure 2.2. For the theory, when only half of the sky is observed (solid and dashed blue lines), (2.43) is used to approximate the leakage effect. In the right column, the theory of the full sky is the same as for the half sky since the same number of source  $N_{\text{tot}}$  are distributed on the observable region (2.42). The simulations follow the procedure described in Section 3.2.2 and also include the kinematic dipole (see main text).

dipole with  $d_{\text{kin}} = 0.005$  pointing towards  $\delta = 90^\circ$  is included. To do this, we replace each pixel value

$$m_p \rightarrow m_p(1 + d_{\text{kin}} \cos \delta_p). \quad (2.59)$$

The details of these simulations are not relevant here. They are explained in more depth in Section 3.2.2. We compare the results obtained with an intrinsic clustering,  $C_l = 10^{-5}$  for  $l \leq 20$ , to the results setting  $C_l^{\text{int}} = 0$ . Both contain the shot noise and we let the total number of sources  $N_{\text{tot}}$  vary. Lastly, in Figure 2.5, one can also see the difference between a full sky coverage and a partial sky coverage, in this case using the Half Mask from Figure 2.2.

We begin to discuss the results of the full sky coverage. First, we notice that the theory agrees perfectly with the simulations. This confirms the calculations leading to (2.57) and (2.58). We see that an increasing amount of sources reduces the shot noise as expected.

Therefore, for increasing  $N_{\text{tot}}$ , the mean of the dipole amplitude converges to the kinematic dipole amplitude  $d_{\text{kin}} = 0.005$ , the standard deviation decreases and the deviation angle becomes smaller.

Through the presence of intrinsic clustering, the combined dipole does not approach the values from the kinematic dipole for  $N_{\text{tot}} \rightarrow \infty$ . Instead, the standard deviation of the dipole amplitude and the deviation angle converge to a fixed value. Without intrinsic clustering, the standard deviation of the amplitude and the deviation angle continue to decrease with increasing  $N_{\text{tot}}$ . Thus, intrinsic clustering limits the precision with which the kinematic dipole amplitude and direction can be determined.

Next, we turn our focus to the results from the analysis where half of the sky is masked. To obtain the theoretical values for this case, we use the approximation (2.43) to include leakage. When  $C_l^{\text{int}} = 0$ , the theory of the full sky is the same as the one of the Half Mask, which is a consequence of the approximation (2.42), i.e. the fact that the same number of sources  $N_{\text{tot}}$  is distributed in the observed region. Obviously, the agreement between simulations and theory is not as good as for the full sky analysis. This is especially visible for the deviation angle, which is due to the fact that in this approximation, directional biases are completely neglected.

At this point, the consequences of the  $\Lambda$ CDM model on the number count dipole have been completely quantified. We have derived the full  $\Lambda$ CDM prediction for the number count dipole in the form of a PDF for amplitude and direction.

## 2.6 Evaluation of the Significance

Whenever measuring a quantity, one would like to characterize the agreement or disagreement between observation and theoretical expectation in one number. Typically the number of standard deviations  $\sigma$  between the two values is used. For example in particle physics,  $5\sigma$  corresponds to a discovery and  $3\sigma$  is considered evidence. In this section, we deal with the question how to analyse the significance of the observed dipole.

When observing the dipole, its amplitude as well as its direction are computed. Again, instead of considering two coordinates for the direction, it is sufficient to only consider the deviation angle  $\theta \equiv \arccos(\hat{\mathbf{d}}_{\text{kin}}^N \cdot \hat{\mathbf{d}})$  between the kinematic dipole  $\hat{\mathbf{d}}_{\text{kin}}^N$  and the observed dipole  $\hat{\mathbf{d}}$ . Amplitude and deviation angle are not independent (see (2.54)), so they need to be analysed together.

In order to fully include the effects of the partial sky coverage, we use simulations to assess the significance of the observations in Chapter 3 and Chapter 4. This means that many ( $10^3 \sim 10^7$ ) mock catalogs with all the properties that are relevant to the dipoles are generated. The dipoles of all mock distributions are computed and counted in small bins to find the distribution  $P(d, \theta)$  which gives the probability to observe a dipole amplitude  $d$  and a deviation angle  $\theta$  given all the assumptions by the  $\Lambda$ CDM model. This is a better approach than using the PDF (2.54), which only approximates the effect of the incomplete sky coverage.

Here, the PDF (2.54) serves as an example of  $P(d, \theta)$  usually obtained through simulations. The kinematic dipole amplitude is set to  $d_{\text{kin}} = 0.005$  and the contributions from

intrinsic and shot noise dipoles are characterized by  $\sigma_r = 0.005$ . In Figure 2.4, where the PDF is shown, a cross marks an example observation  $d_{\text{ex}} = 0.016$  and  $\theta_{\text{ex}} = \pi/8$  (motivated by the analysis done in Chapter 3). We first assess the significance of this particular outcome by the  $p$ -value, which is defined as the probability to obtain an outcome as extreme as the observed one. This means the  $p$ -value is the integral of  $P(d, \theta)$  over the region where  $P(d, \theta) \leq P(d_{\text{ex}}, \theta_{\text{ex}})$ . This is indicated in the left panel of Figure 2.4 by the orange region.

Commonly used in the literature is another way of obtaining the  $p$ -value. Noticing that in this example as well as in later data analyses, the deviation angle by itself matches our expectation very well, one can consider the excess in amplitude only. This corresponds to integrating  $P(d, \theta)$  over the blue and green region shown in the right panel of Figure 2.4. In other words, the  $p$ -value is the number of simulations, where the amplitude is found to be at least the observed amplitude, divided by the total number of simulations.

In the recent analysis of the dipole in the distribution of quasars [27], yet another approach is taken. Only simulation outcomes with an amplitude larger than the observed one and a deviation angle smaller than the observed one are counted to obtain the  $p$ -value. This corresponds to the green region in Figure 2.4.

The  $p$ -value is then converted to a number  $s$  of standard deviations  $\sigma$ , as if the distribution was a Gaussian one. For the first discussed case, the relation is

$$p(s) = \int_0^{2\pi} d\phi \int_{s\sigma}^{\infty} dr g(x, \sigma) g(y, \sigma) = \exp \frac{-s^2}{2}, \quad (2.60)$$

where  $r = \sqrt{x^2 + y^2}$  and  $g(x, \sigma)$  is a Gaussian PDF with zero mean and standard deviation  $\sigma$ . When the  $p$ -value is determined by the amplitude only, it depends on  $s$  by

$$p(s) = \int_{s\sigma}^{\infty} dx g(x, \sigma) = \frac{1}{2} [1 - \text{erf}(s/\sqrt{2})], \quad (2.61)$$

using the error function. In the quasar dipole analysis [27], this expression is used as well. Inverting above expressions gives

$$s(p) = \sqrt{-2 \ln p} \quad (2.62)$$

$$s(p) = \sqrt{2} \text{erf}^{-1}(1 - 2p). \quad (2.63)$$

Returning to our example, we compute these values for the different approaches and find

$$\text{(orange, 'as extreme')} : p = 0.25 \rightarrow s = 1.7 \quad (2.64)$$

$$\text{(blue + green, 'only amplitude')} : p = 0.05 \rightarrow s = 1.7 \quad (2.65)$$

$$\text{(green, 'amplitude and angle')} : p = 0.01 \rightarrow s = 2.3. \quad (2.66)$$

The first two methods agree on  $1.7\sigma$ , because the significance arises only due to the large amplitude. However, with the third method, one would conclude a larger significance of  $2.3\sigma$ . In the data analysis of Chapter 3 and Chapter 4, the second method is used, since

only the amplitude exceeds the expectations. However, the first method is applicable to all outcomes and should be used, if both amplitude and deviation angle differ from the  $\Lambda$ CDM model expectations.

## 2.7 Dipole Estimator

In this section, the estimator that is used throughout this work to measure the dipole is introduced. The estimator returns the best fit values of the dipole for a given field.

We use the estimator provided by the `fit_dipole` method in `healpy` (a Python package based on HEALPix) [47, 48]. HEALPix provides a pixelisation scheme on the sphere, where each pixel covers the same area. The field of observed sources is computed by counting the number of sources  $N_p$  within the flux cut in each pixel  $p$ . From this pixelised field, the estimator minimises the quantity

$$\sum_p (N_p - \mathbf{D} \cdot \mathbf{r}_p)^2 \quad (2.67)$$

to find the best fit variables for the monopole  $m$  and the three dipole components denoted as the vector  $\mathbf{D} = (m, D_x, D_y, D_z)$ . The sum runs over all unmasked pixels  $p$ ; the components of  $\mathbf{r}_p = (1, \hat{\mathbf{r}}_p)$  are one and the coordinates of the pixel  $p$  on the unit sphere. The minimum of (2.67) is determined by the linear equation

$$\mathbf{D} = \mathbf{M}^{-1} \sum_p \mathbf{r}_p N_p, \quad M_{ij} = \sum_p r_{p,i} r_{p,j}. \quad (2.68)$$

Since we define the dipole in (2.2) to be the fluctuation relative to one, we need to divide by the monopole. Our estimator for the number count dipole is therefore

$$\mathbf{d}_{\text{est}}^N = (D_x/m, D_y/m, D_z/m). \quad (2.69)$$

Instead of this estimator, one can also consider the estimator advocated in [20] which minimises the quantity  $\chi^2 = \sum_p [N_p - \mathbf{D} \cdot \mathbf{r}_p]^2 / (\mathbf{D} \cdot \mathbf{r}_p)$  and thus only differs by the normalization of the summand. This is more appropriate to use, if the number of sources per pixel differs significantly from pixel to pixel, because the normalization properly takes into account the shot noise variance. However, in our case, the number of sources per pixel varies very little, since the dipole and other fluctuations are small. Since the minimum of the  $\chi^2$ -expression cannot be found analytically, a numerical minimisation needs to be performed, which involves a larger computational effort. Therefore, we prefer the simpler version with a linear solution.

We tested the two estimators for both complete and incomplete sky coverages. On simulated shot noise fields, the dipole amplitudes found by the two estimators agree for each realization of shot noise within on average 6% and the directions within 5°. Also, the mean and variance of all observed outcomes are equal for both estimators. Therefore, we conclude that they are unbiased with respect to each other and work equally well.

## 3 NVSS Radio Sources Dipole

Having presented all the relevant theory, in this chapter, actual data is analysed. A survey conducted with the Very Large Array (VLA) of the National Radio Astronomy Observatory (NRAO) between 1993 and 1996, called NRAO VLA Sky Survey (NVSS) [11] is yet the most suitable radio survey to analyse the cosmic matter dipole. There are several reasons, why the source catalog of the NVSS is more suitable than other catalogs of radio sources. Firstly, the NVSS covers the full region above declination  $\delta = -40^\circ$  and thus a large fraction of the sky. Secondly, the survey has a high sensitivity, such that one expects fainter radio sources at cosmic distances to dominate over the local structure. In this chapter, we will discuss the survey in more detail and estimate the dipole in the distribution of sources of the NVSS catalog. We simulate mock catalogs, which include the intrinsic dipole, the kinematic effects and shot noise, in order to compare the observed dipole with theory.

### 3.1 Measuring the Dipole

To analyse the dipole, a subsample of the full catalog that is free of any observational artefacts needs to be created. Therefore, in this section, we discuss possible contaminations and how to eliminate them.

#### 3.1.1 Data

The NVSS provides a catalog<sup>1</sup> of approximately  $1.8 \times 10^6$  sources. Each of these is described by its flux  $F$  as well as the right ascension  $\alpha$  and the declination  $\delta$  in the J2000.0 equatorial coordinate system to express its position on the sky. Additionally, estimated uncertainties in the flux  $\sigma_F$  and in the two positional coordinates  $\sigma_\alpha$ ,  $\sigma_\delta$  are specified for each source. However, there is no estimate of the redshift. Thus, the distance to each source is not known but only the direction is. This becomes an issue when calculating the expected angular power spectrum in Section 3.2.1.

The distribution of the sources' fluxes and the distribution of the relative uncertainties are shown in Figure 3.1. The distribution of the sources' positions is well visualized by a Mollweide projection (see left panel of Figure 3.2). One can clearly see the higher density of sources in the galactic plane which appears like an arc in equatorial coordinates. Also, there is a horizontal stripe at around  $\delta = -12^\circ$  (see also right panel of Figure 3.2). Due

---

<sup>1</sup>available at <ftp://ftp.cv.nrao.edu/nvss/CATALOG/FullNVSSCat.text>

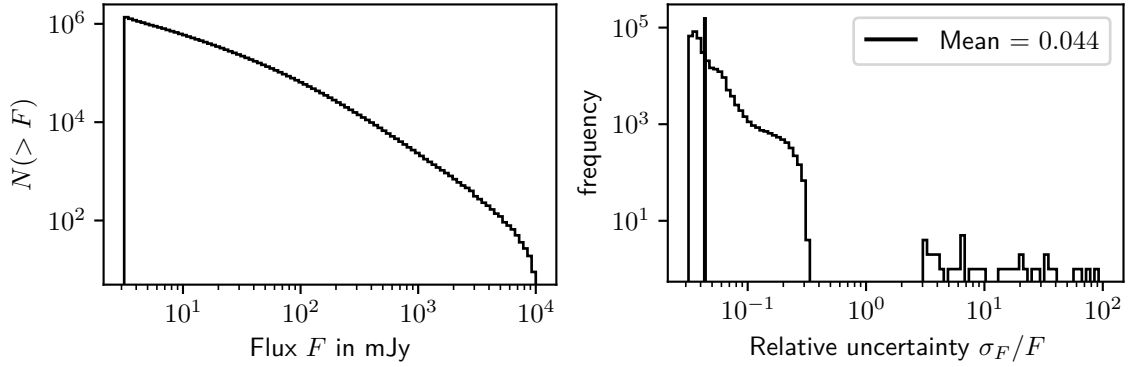


Figure 3.1: *Left:* The cumulative source count of all sources in the NVSS catalog. *Right:* The distribution of the relative flux uncertainties of all sources with a flux larger than 15mJy.

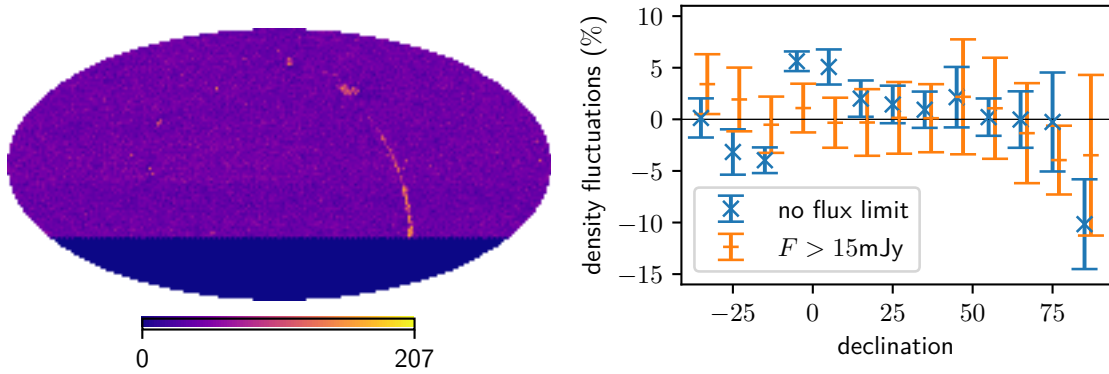
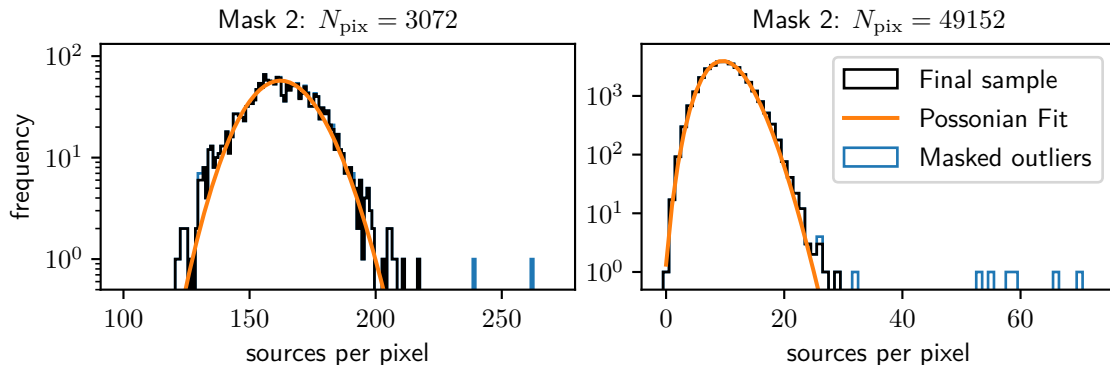


Figure 3.2: *Left:* The distribution of the positions of all sources in the NVSS catalog in equatorial coordinates. Each of the 49,152 equal area pixels shows the number of sources in that pixel. For the conventions used in the projection, see Figure 2.2. *Right:* The error bars show mean and standard deviation of the relative fluctuations in the surface density in declination bins of  $20^\circ$ . The sudden change at  $\delta \approx -12^\circ$  is eliminated by setting a lower flux limit.

to different telescope array configurations at different declinations [10], there are surface density fluctuations that are an observational artefact. Therefore, even though the NVSS is estimated to be 99% complete above a flux of 3.4mJy, a larger minimum flux cut needs to be applied, such that these observational anisotropies vanish. In the following analysis, we consider two different cuts

$$\begin{aligned} F &> 15\text{mJy} \\ F &> 20\text{mJy}. \end{aligned} \tag{3.1}$$

In previous works, an upper flux cut of 1000mJy is often applied, in order to suppress the contribution from sources that are very close to us. Since it is not possible to distinguish between a very luminous but faint or less luminous but closer source, we do not apply this cut. Imposing this upper cut would lead the observed dipole amplitude to be 2% larger.



*Figure 3.3:* The histograms show the distribution of numbers of sources per pixel for Mask 1 in the left panel and Mask 2 in the right panel after applying the flux cut  $F > 15\text{mJy}$ . Also shown is a Poissonian fit to the distribution. The pixels that are removed because of sidelobe contamination as described in the main text are colored blue.

### 3.1.2 Mask

The NVSS does not cover the full sky, but only the region with a declination larger than  $\delta = -40^\circ$ . In addition, the Milky Way blocks the view of distant sources. Both of these regions cannot be used in the analysis, hence a mask is introduced. The mask covers the region south of  $\delta = -40^\circ$  as well as the region within  $\pm 10^\circ$  around the galactic plane. The masks are created using the HEALPix pixelisation scheme [47, 48]<sup>2</sup>. No parts of the unmasked HEALPix pixels should lie in the region that is desired to be masked. To ensure this, all masks are created slightly larger than with the values stated above. For the resolution parameter  $N_{\text{side}} = 16$  and  $N_{\text{side}} = 64$ , this corresponds to an offset of  $3.8^\circ$  and  $0.95^\circ$ , respectively.

In Figure 3.3, we show a histogram of the number of sources per pixel after masking the galactic plane and the part of the sky not covered by the NVSS. For nearly all pixels, it closely follows a Poissonian distribution. However, a few outliers contain much more sources than expected. As detailed in [49], these outliers are likely to be a survey artefact. The observing beam has sidelobes (see Fig. 16 of [11]), such that bright sources could lead to false detections of artificial sources. We identify two regions around  $(\delta, \alpha) \approx (-7.2^\circ, 84^\circ)$  and  $(12^\circ, 186^\circ)$  in which several bright sources with  $S > 2.5\text{ Jy}$  are found. It is very likely that these lead to the contamination as indicated by the unexpectedly large pixel counts in this region. Thus, we exclude an area of  $\approx (3.7^\circ)^2$  around both of these regions to eliminate the artificial sources. If these two regions were not masked, the observed dipole amplitude would be approximately 10% larger.

The regions south of  $\delta = -40^\circ$ , within  $\pm 10^\circ$  around the galactic plane and these two additional patches constitute Mask 1. For it, a resolution of  $N_{\text{side}} = 16$  is chosen, such that there are  $N_{\text{pix}} = 3072$  pixels, sufficient to resolve a dipole.

We additionally introduce a second mask, following [17]. The goal of the second mask is to remove as much of the local structure as possible, and thereby to eliminate a large

<sup>2</sup><http://healpix.sf.net/>

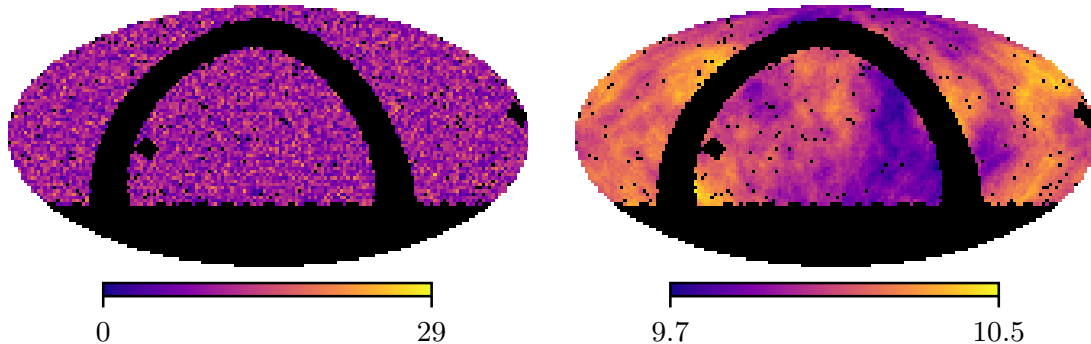


*Figure 3.4:* Distribution of NVSS sources in equatorial coordinates after applying the cut  $F > 15\text{mJy}$  and masking with Mask 2. Mask 2, which covers 35% of the sky is shown as black pixels. Mask 1 is very similar, covering as well the region south of  $\delta = -40^\circ$ , the galactic plane, which appears as an arc and the two large patches. The difference aside from the higher resolution is that Mask 2 additionally covers 108 small regions to suppress the influence of local structure.

*Left:* Number of sources per pixel.

*Right:* Each pixel shows the average of all unmasked pixels within  $20^\circ$  to make the dipolar distribution visible. The figure on the English title page shows the same data in galactic coordinates averaged over all unmasked pixels within  $90^\circ$ , i.e a full hemisphere.

fraction of the intrinsic dipole. Since this involves covering many small regions, we increase the resolution to  $N_{\text{side}} = 64$  with  $N_{\text{pix}} = 49\,152$  pixels, such that masks can be applied more precisely.

Again, the regions south of  $\delta = -40^\circ$ , within  $\pm 10^\circ$  around the galactic plane and the two additional patches are masked. We then exclude the pixels within a disc of  $0.1^\circ$  around 8 local superclusters (see Table 1 of [17]). Secondly, we mask the same small discs around 575 local and bright ( $F > 213\text{mJy}$ ) radio galaxies, catalogued in [50]. Both of these steps together mask an additional 904 pixels and thus 1.8% of the sky. This mask is called Mask 2 in the following and is displayed in Figure 3.4 together with the distribution of the final sample of sources. A detailed discussion about different masks is given in [17]. There, it is found that additional masks to remove local sources or masking the supergalactic plane does not change the observed dipole significantly.

The remaining number of sources for the two flux limits (15mJy and 20mJy) and the two masks (Mask 1 and Mask 2) are

$$\begin{aligned} N_{15}^{\text{M1}} &= 310128, & N_{15}^{\text{M2}} &= 322076, \\ N_{20}^{\text{M1}} &= 242012, & N_{20}^{\text{M2}} &= 251252. \end{aligned} \tag{3.2}$$

Even though Mask 2 covers more distinct patches of the sky, more sources remain than in Mask 1, because the applied cuts are more precise due to the higher resolution.

Mask	$F_{\min}/\text{mJy}$	$d/10^{-2}$	$\delta$ [°]	$\alpha$ [°]	$\theta$ [°]
1	15	$1.32 \pm 0.05$	$2.3 \pm 2.7$	$147 \pm 2$	$23.5 \pm 2.5$
		1.30	-1.0	146	22.9
1	20	$1.53 \pm 0.06$	$-15.7 \pm 2.4$	$150 \pm 2$	$20.6 \pm 2.2$
		1.58	-16.6	148	24.0
2	15	$1.25 \pm 0.04$	$9.3 \pm 2.6$	$150 \pm 2$	$24.3 \pm 2.3$
		1.23	6.3	148	23.6
2	20	$1.43 \pm 0.05$	$-12.1 \pm 2.4$	$154 \pm 2$	$14.8 \pm 2.0$
		1.47	-12.4	152	16.8
$\mathbf{d}_{\text{kin}}^N$		0.43-0.44	-6.944	167.942	0

*Table 3.1:* NVSS dipole amplitude and direction for different masks and flux cuts. The last column shows the deviation angle  $\theta$  between the dipole and the velocity direction (1.1). The first line in each row shows the mean and standard deviation of the values observed in 500 random catalogs including the flux uncertainty. The second line shows the original value observed in the NVSS data. For comparison we also show the values for the kinematic dipole (3.7) as expected from the CMB (1.1) .

### 3.1.3 Results

In our dipole analysis, we also include the uncertainty in the observed quantities of each source. The mean relative uncertainty in the flux is 4.4% (Figure 3.1). The uncertainty of the positions are of order  $\sigma_{\alpha,\delta} \lesssim 1$  arcsec. The effect of the latter on the observed dipole is tested to be negligible ( $< 0.1\%$ ) compared to the effect of the uncertainties in the sources' fluxes. These are included into the analysis, similar to the method of [28].

From the original catalog, we create a random new catalog by replacing each flux with a random Gaussian variable. Its mean is the original flux and the standard deviation is the flux uncertainty. For this new catalog, the amplitude and the direction of the dipole is measured using the estimator described in Section 2.7. This procedure is repeated 500 times to get an estimate how the flux error influences the observed dipole amplitude and direction.

Table 3.1 lists the mean and standard deviation of amplitude and direction from the 500 random catalogs, as well as the value obtained with the original data. As discussed in Section 2.5, the two coordinates can be combined into the deviation angle  $\theta$  between the dipole direction and the CMB dipole. While there is no significant difference between the two masks, there is a difference between the two flux cuts. First, the amplitude is larger for the flux cut of 20mJy. This trend is expected because the shot noise contribution is larger due to a smaller number of sources. Secondly, we note a change in the declination between the two flux cuts. This is possibly an artifact of residual biases due to the different telescope configurations (see right panel of Figure 3.2).

## 3.2 Simulations

In order to compare the observed dipole to the expectations from the  $\Lambda$ CDM model, we simulate mock catalogs including the same sky coverage, kinematic effects, intrinsic clustering and shot noise. These mocks are intended to mimic all the relevant properties of the NVSS. Next to the intrinsic dipole, higher multipoles of the intrinsic angular power spectrum can also affect the observed dipole because of the incomplete sky coverage (see Section 2.4). Therefore, we start by computing the angular power spectrum.

### 3.2.1 Angular Power Spectrum

To calculate the angular power spectrum with CLASS (see Section 2.2), we need to estimate the bias relation  $b(z)$ , which can depend on the redshift  $z$ , and the redshift distribution  $n(z)$ . For the bias, we use the model given in [51]

$$b(z) = 1.6 + 0.85z + 0.33z^2. \quad (3.3)$$

Since the radio telescope does not measure the redshift of the sources, it is very difficult to estimate  $n(z)$ . This is the main systematic uncertainty in the analysis. One way to overcome this problem is finding NVSS sources in catalogs of other surveys, that provide information on the redshift. This was done in [15, 51], where the NVSS catalog was crossmatched with the Combined EIS-NVSS Survey as well as the Hercules survey. 131 sources brighter than 10mJy with spectroscopic redshift measurements were found in these surveys that cover a much smaller fraction of the sky of  $\sim 10\text{deg}^2$ . To these redshifts, the function

$$n(z) \propto z^{a_1} \exp[-(z/a_2)^{a_3}] \quad (3.4)$$

has been fitted, finding the parameters  $a_1 = 0.74$ ,  $a_2 = 0.71$ ,  $a_3 = 1.06$ . In the fitting procedure, also higher multipoles observed in the distribution of NVSS sources have been used. Fitting only the redshifts of the crossmatched sources yields an angular power spectrum which is approximately two times smaller on large scales.

In this work, we follow a different approach and use the simulation T-RECS [52] to estimate the redshift distribution. Catalogs produced with T-RECS provide a realistic model of the observable radio sky. We use both the simulated star forming galaxies (SFG) as well as the active galactic nuclei (AGN) of the publicly available ‘wide catalog’<sup>3</sup> to find the redshift distribution of all sources above the two flux limits (3.1), respectively. The distribution of the redshifts is shown in the left panel of Figure 3.5. AGN dominate at large redshifts, whereas a small amount of SFG dominate at smaller distances. We compare this distribution to the fitted function (3.4), which we call the N&T fit after the authors A. Nusser and P. Tiwari [51]. The multipoles  $C_l$  are calculated with CLASS and the result is seen in the right panel of Figure 3.5. Note that the local kinematic dipole due to our velocity is not part of this calculation.

<sup>3</sup><http://cdsarc.u-strasbg.fr/viz-bin/qcat?VII/282>

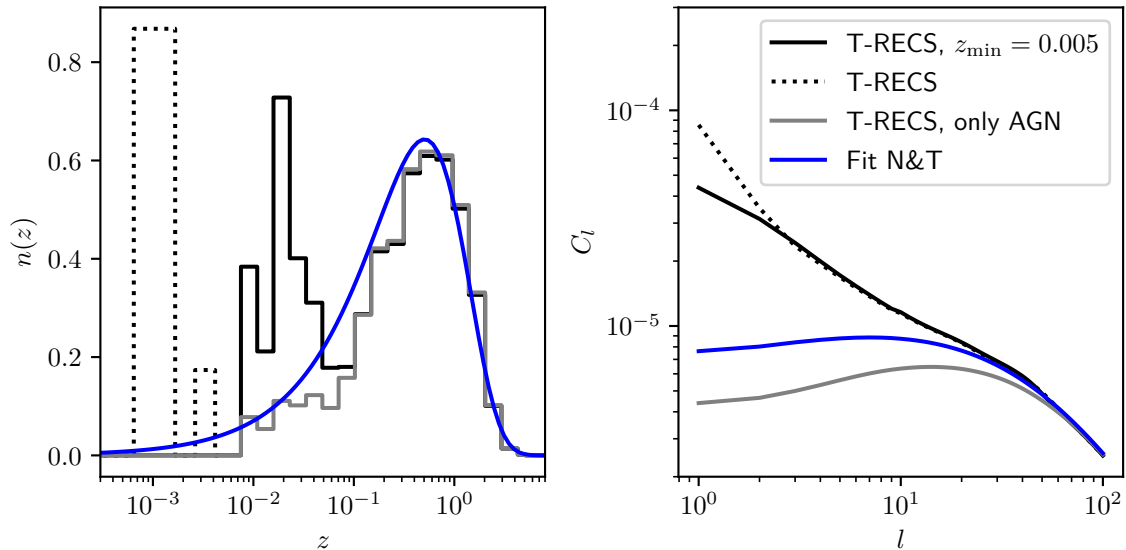


*Figure 3.5: Left:* Comparison of different redshift distributions. For T-RECS, all sources above  $F = 15\text{mJy}$  have been used. The blue lines show the N&T fit (3.4) [51]. The logarithmic scaling of the redshift axis better illustrates the differences in the amount of local sources.

*Right:* The corresponding angular power spectra calculated with CLASS. The result for T-RECS with the flux cut  $F = 20\text{mJy}$  is very similar. For the computation, the bias given in (3.3) is used. The magnification bias is set to  $s = x/2.5 = 0.85/2.5$ , motivated by the fit of  $x$  in (3.6). The evolution bias is set to zero. For an overview of the different contributions to the angular power spectrum, see the discussion in Appendix B and in particular Figure B.1.

Comparing the redshift distributions and the corresponding angular power spectra, we notice that the anisotropies on the largest scales  $l < 10$  strongly depend on the amount of local sources. We make this explicit by imposing a redshift cut of  $z > 0.005$  to the T-RECS redshift distribution. The existence of very few sources closer than this cutoff changes the intrinsic dipole  $C_1$  by a factor of 2. Since removing local sources for example by masking the supergalactic plane does not change the dipole significantly [17], we argue that such sources with redshift smaller than  $z_{\min} = 0.005$  are successfully removed in the NVSS data. Therefore, in the following analysis we use the angular power spectrum found with the redshift distribution of simulated T-RECS sources above  $z_{\min} = 0.005$ . Even so, the small number of local sources with  $0.005 < z < 0.1$  which make up 1.5% of all T-RECS sources and are not present in the N&T fit lead to an increase of the angular power spectrum on large scales by a factor of 5. To compare to previous studies, we will therefore also discuss the results using the fit of N&T.

### 3.2.2 Mock Catalogs

The mock catalogs are simulated in such a way that they represent what we would expect to observe assuming the  $\Lambda\text{CDM}$  model. Thus, they include the intrinsic clustering calculated

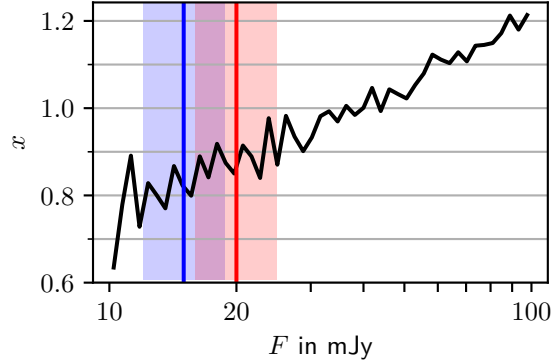


*Figure 3.6:* The fitted logarithmic slope  $x$  of the cumulative source count  $N(> F) \propto F^{-x}$  at different minimum flux cuts  $F$ . For both flux cuts 15mJy (blue) and 20mJy (red) we take  $x$  to be the average over the shaded region. Here, the analysis is done for all sources not covered by Mask 1. The results are the nearly the same for Mask 2.

above, the kinematic dipole with the velocity and direction inferred from the CMB (1.1), shot noise and are masked in the same way as the data.

The kinematic dipole is given by (2.12)  $\mathbf{d}_{\text{kin}}^N = [2 + x(1 + \alpha)]\boldsymbol{\beta}$ . In order to calculate its amplitude, we need to know the frequency dependence of the flux  $F \propto \nu^{-\alpha}$  to find the spectral index  $\alpha$  and the slope of the cumulative source counts with flux larger than  $F_{\text{min}}$  to find  $x$ .

By crossmatching sources from the LOFAR [53] survey (150MHz) with sources from the NVSS, the median spectral index  $\alpha$  is found to be  $\alpha = 0.78 \pm 0.015$  [54]. Crossmatching NVSS with SUMSS [23] (843MHz) sources gives a distribution of spectral indices  $0.83 \pm 0.35$  [55]. Typically,  $\alpha$  is simply set to 0.75 [33]. To include the remaining uncertainty, we use

$$\alpha = 0.78 \pm 0.05. \quad (3.5)$$

The parameter  $x$  can be found in the data itself. Figure 3.6 shows a fit of the logarithmic slope of the number of sources  $N(> F) \propto F^{-x}$  using all sources that are not masked. For  $F_{\text{min}} = 15\text{mJy}$  and  $F_{\text{min}} = 20\text{mJy}$ , we average the slope in the interval  $[F_{\text{min}}/1.25, 1.25 \times F_{\text{min}}]$  (see Figure 3.6) and find

$$x_{15} = 0.84 \pm 0.05, \quad x_{20} = 0.89 \pm 0.05. \quad (3.6)$$

In previous works, an average of the slope over the full flux range  $F > F_{\text{min}}$  has been used. Since the slope increases towards larger fluxes, values of  $x \approx 1.0$ – $1.1$  are found (e.g. [14, 28]). However, we argue that the slope at the flux cut is the relevant one, since this is where a source might enter or leave the catalog due to Doppler effects. We are confirmed by the fact that using a more sophisticated fitting function than a power law [15, 20] leads to results similar to (3.6). In conclusion, we expect the kinematic dipole to be

$$d_{\text{kin}}^N = 4.3 \times 10^{-3} (F_{\text{min}} = 15\text{mJy}) \quad \text{and} \quad d_{\text{kin}}^N = 4.4 \times 10^{-3} (F_{\text{min}} = 20\text{mJy}). \quad (3.7)$$

With that, we are able to create the mock catalogs. To do so, we follow the procedure described in Appendix A.2, but also list all the relevant steps here. First, we generate a realization of the angular power spectrum by using the method `synfast` provided by HEALPix, where random normally distributed  $a_{lm}$  are drawn, such that  $\langle |a_{lm}|^2 \rangle = C_l$  (see (A.7)). With these  $a_{lm}$ , the intrinsic fluctuations  $\Delta(\hat{\mathbf{n}})$  on the sky are calculated as in (A.2). Each pixel value is set to

$$m_p = [1 + \Delta(\hat{\mathbf{n}}_p)] N_{\text{tot}} / (N_{\text{pix}} f_{\text{sky}}), \quad (3.8)$$

where  $N_{\text{tot}}$  is given in (3.2). This ensures that the total number of sources after masking is the same as for the NVSS data. Next, shot noise is included by replacing each pixel value with a random Poissonian number with the mean given by the original pixel value

$$m_p \rightarrow \mathcal{P}(m_p). \quad (3.9)$$

Lastly, the effect of our local motion is simulated by multiplying each pixel value by the expected change of the number density (2.10). In order to include the uncertainty of the spectral index and the logarithmic slope, we draw random Gaussian variables  $\alpha_r$  and  $x_r$  for each mock catalog

$$\alpha_r = \mathcal{N}(\bar{\alpha}, \sigma_\alpha) \quad (3.10)$$

$$x_r = \mathcal{N}(\bar{x}, \sigma_x) \quad (3.11)$$

$$m_p \rightarrow m_p \delta(\hat{\mathbf{n}}_p)^{2+x_r(1+\alpha_r)} \approx (1 + [2 + x_r(1 + \alpha_r)]\beta \cos \theta_p) m_p, \quad (3.12)$$

where the bar and  $\sigma$  denote the mean and uncertainty as given in (3.5) and (3.6), respectively.

For both masks, for both flux cuts and for the two angular power spectra, this procedure is repeated 10 000 times to create a large number of mock catalogs for each of the 8 cases.

### 3.3 Results

For each simulated mock catalog, the dipole amplitude  $d$  and the deviation angle  $\theta$  between the dipole and the direction of our velocity is computed using the estimator described in Section 2.7. The results of all mock catalogs are shown in Figure 3.7. We display the results for the two different flux cuts as well as for two different input angular power spectra using Mask 2 (Figure 3.4). The results for Mask 1 are not shown, since they are very similar.

We proceed to compare the observed dipole amplitude and direction in the distribution of NVSS sources (see Table 3.1) with the results from the mock catalogs. In general, the angle between the NVSS dipole and the CMB dipole agrees well with the simulations. Therefore, we focus only on the amplitude of the NVSS dipole. Comparing the results for the two different flux cuts, the observed dipole amplitude is smaller for the flux cut at 15mJy than for the cut at 20mJy. The same is true for the mock catalogs. The higher flux cut leads to less sources and thus a larger shot noise contribution, so that the mock

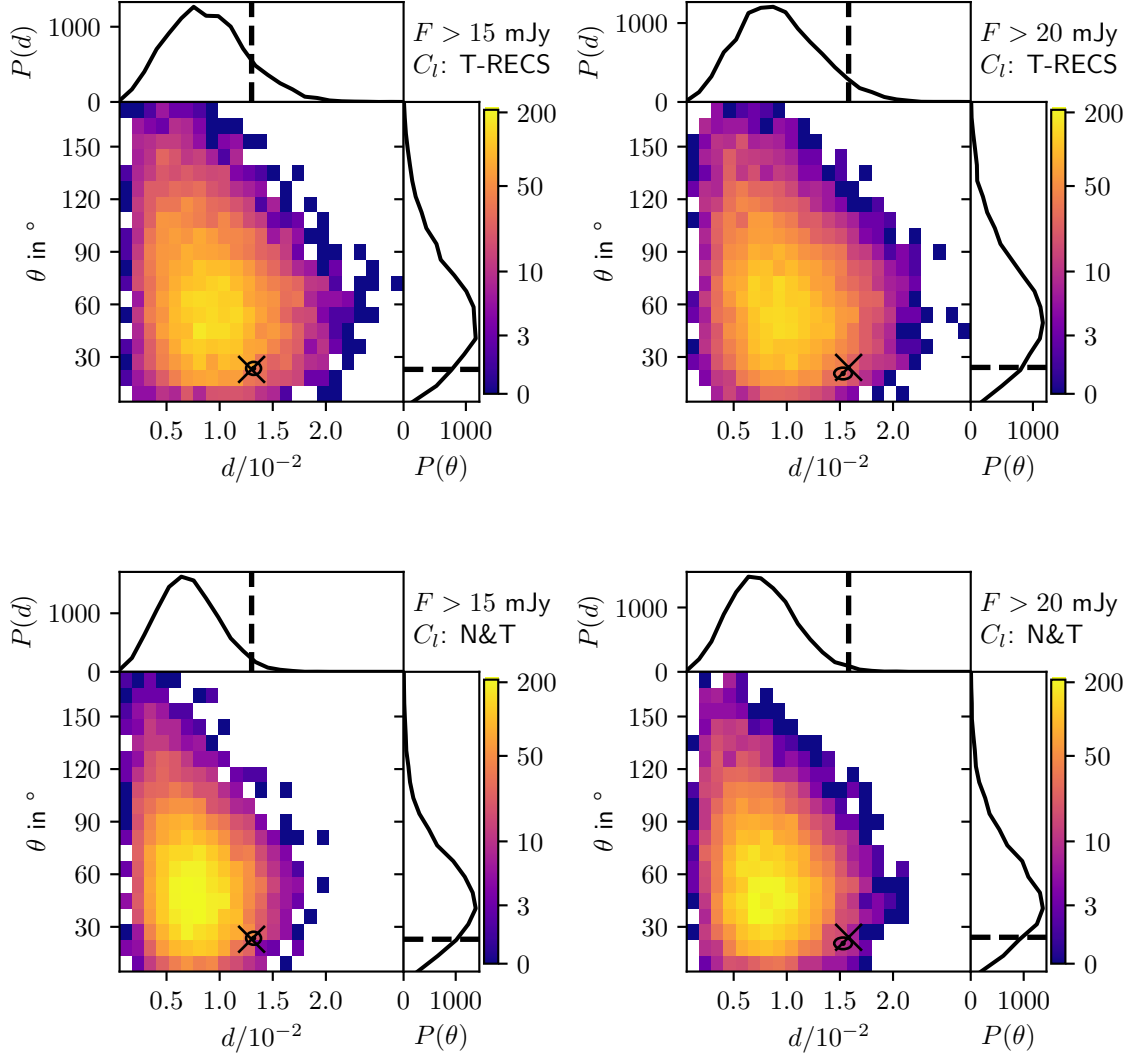


*Figure 3.7:* The results of 10 000 simulations in a two dimensional histogram showing the distribution  $P(d, \theta)$  of mock dipole amplitudes  $d$  and deviation angles  $\theta$  in a logarithmic scale. The results are shown for the two flux cuts (left and right column) and using the different angular power spectra, T-RECS with  $z > 0.005$  (top row) and the N&T fit (3.4) (bottom row).

In each figure, the upper and right side panels show the histogram of the amplitudes  $d$  and the deviation angles, respectively. The cross in the main panel and the dashed lines in the side panels mark the values of  $d$  and  $\theta$  observed in the distribution of NVSS sources. The ellipse shows the mean and  $3\sigma$  contour of the observed dipole including flux errors as listed in Table 3.1.

$C_l$	T-RECS				N&T			
	15mJy		20mJy		15mJy		20mJy	
$F_{\min}$	1	2	1	2	1	2	1	2
Mask	1	2	1	2	1	2	1	2
$p$ in %	13	12	7.2	6.7	2.9	2.1	1.5	1.3
# of $\sigma$	1.1	1.2	1.5	1.5	1.9	2.0	2.2	2.2

*Table 3.2:*  $p$ -value and significance in numbers of standard deviations  $\sigma$  for the different analyses. This shows the (dis)agreement between theory and observation. The  $p$ -value is obtained by counting the number of mock catalogs with a dipole amplitude larger than the one observed in the NVSS data. It is converted into the number of  $\sigma$  for a one-sided distribution with (2.63).

dipoles then to be larger. We also compare the results using the angular power spectrum computed from the T-RECS simulation with  $z > 0.005$  (solid black line in Figure 3.5) with the results using the N&T fit (blue line in Figure 3.5). Since the intrinsic clustering is smaller in the latter, the dipole amplitudes found in the mock catalogs also tend to be smaller.

This has a strong impact on the comparison between theory and observation. Because the observed deviation angle  $\theta$  agrees well with the mock catalogs, we decide to only use the amplitude of the results to evaluate the significance. Counting the number of mock catalogs with a dipole amplitude larger than the one in the NVSS data and dividing by the total number of mock catalogs gives the  $p$ -value. This is converted to the number of standard deviations for a one-sided distribution by (2.63). The results for the different scenarios are listed in Table 3.2.

In conclusion, the consistency between the dipole observed in the distribution of sources of the NVSS and the  $\Lambda$ CDM model, in particular the cosmological principle and the exclusive kinematic interpretation of the CMB dipole, depends strongly on the presence of local structure. If there are sources closer than  $z \sim 0.1$ , the intrinsic dipole is expected to be so large that the observed dipole amplitude is consistent with the theory with 1.1 to 1.5 $\sigma$ . If this local structure does not play a significant role, then the observed dipole amplitude is larger than expected at 1.9 to 2.2 $\sigma$ . In both cases, the observation is not very significant, since the typical shot noise dipole is as large as the kinematic dipole. We find that more sources and a different way to deal with intrinsic clustering are needed. An attempt to overcome the second problem is analysing the angular power spectrum on smaller scales, i.e. higher multipoles.

### 3.4 Higher Multipoles

Estimating multipoles with  $l > 1$  serves as a meaningful check of the dipole analysis. Ideally, we would like to decide on the question how much local structure is observed, since this not only causes a large intrinsic dipole but also a large quadrupole, octopole etc. (see right panel of Figure 3.5). For sure, we are able to test whether the dipole has an outstanding excess of power or if other higher multipoles are equally large.

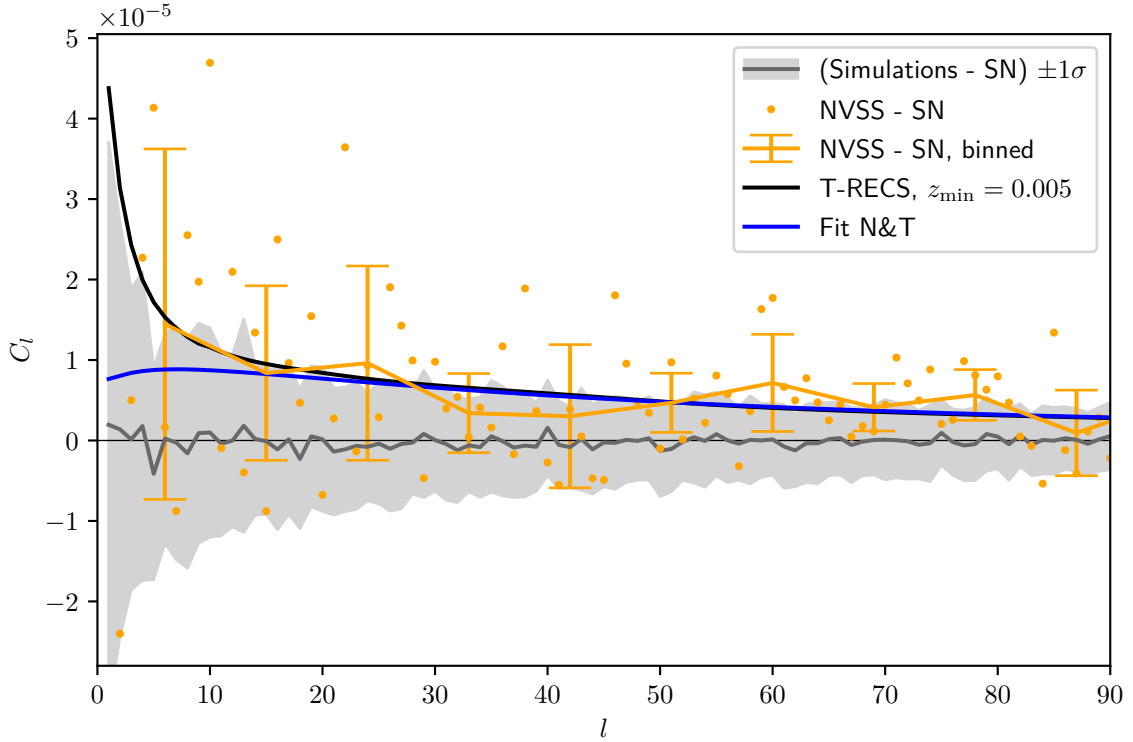


*Figure 3.8:* The angular power spectrum observed in the NVSS source distribution after subtracting the simulated shot noise (with the same mask and number of sources as NVSS). The grey line and the grey band show mean and standard deviation of the angular power spectrum of 100 simulations after subtracting their mean. The dots show each multipole in the NVSS data ( $F_{\min} = 15\text{mJy}$  and Mask 2). The error bars show the mean and standard deviation of 9 neighboring multipoles, starting with  $l = 2$ . The dipole is not included, its value minus shot noise is observed to be  $C_1 = 25 \times 10^{-5}$ . For comparison, we also show the angular power spectra used in the NVSS dipole analysis from the right panel of Figure 3.5.

We use the estimator for the multipoles presented in Appendix C based on [56]. We simulate 100 mock catalogs containing only shot noise with the same number of sources and the same sky coverage as the NVSS to compare their angular power spectrum to the observation. From both the simulations and from the data, the mean shot noise  $C_{\text{SN}} = 2.6 \times 10^{-5}$  of the simulations is subtracted. This mean shot noise agrees with the expected shot noise (2.39) of  $4\pi f_{\text{sky}}/N_{\text{tot}}$  within 5%. The remaining angular power spectrum of the simulations is therefore scattered around zero. The residuals in the angular power spectrum of the NVSS source distribution contain only the intrinsic clustering and the kinematic dipole. In Figure 3.8, we show the results for  $F_{\min} = 15\text{mJy}$  and Mask 2. The results for the other scenarios with different flux cut and mask are similar. First of all, we notice that the angular power spectrum is on average indeed larger than only shot noise. Due to the large shot noise and incomplete sky coverage, there is a lot of scatter in

the individual multipoles. We approximate the mean of the multipoles for different ranges of  $l$  (including the results from other masks and flux cuts)

$$2 \leq l \leq 10 : \quad \langle C_l \rangle \approx (1.5\text{--}2.5) \times 10^{-5} \quad (3.13)$$

$$10 < l < 90 : \quad \langle C_l \rangle \approx (6.5\text{--}7.5) \times 10^{-6}. \quad (3.14)$$

The observed dipole power, however, ranges between  $C_1 \approx (23 \sim 34) \times 10^{-5}$  and is thus more than 10 times larger than the multipoles for  $l > 1$ . The dipole is confirmed to be the outlier and is not fully explained by the expected kinematic  $C_1^{\text{kin}} = 4\pi(d_{\text{kin}}^N)^2/9 = 2.7 \times 10^{-5}$ .

The angular power spectrum found in this work is compatible with the results of [40] as well as [57]. Due to the large amount of scatter, it is not possible to differentiate between the two different angular power spectra used in the analysis of the dipole (see Figure 3.8). Both the one motivated by T-RECS sources and the N&T fit are consistent with the observed multipoles. A new method to overcome the issue of intrinsic clustering is presented in Chapter 5. Before that, in the next chapter, a catalog with four times the number of sources is analysed, thus reducing shot noise by a factor of 2. This allows for a more significant determination of the cosmic matter dipole.

# 4 Quasar Dipole

In [27], a subsample of the CatWISE 2020 source catalog [58] based on data from the WISE mission [59] is created. The sources have been observed in the near-infrared at wavelengths of a few micrometers and instead of the flux, their magnitudes have been measured. The theory presented in Chapter 2 can nevertheless be applied converting the magnitude of each source to a flux (see [27]). In [27], a magnitude limit and a sophisticated mask have been applied to create a sample of distant quasars suitable for the analysis of the cosmic matter dipole. This means to ensure that there are no observational effects in the sample that create an artificial dipole as well as to remove local sources with  $z < 0.1$  as well as possible. The dipole was analysed and a discrepancy between its large amplitude and the assumptions of isotropy and the kinematic interpretation of the CMB dipole was found at  $4.9\sigma$ .

In this chapter, we first apply the methods described in detail when analysing the NVSS data in Chapter 3.2.2 to this sample of quasars, confirming the excess in dipole amplitude. The procedure to create the sample described in [27] is not studied here. Instead, we use the final sample that is publicly available [27]<sup>1</sup>. We show the distribution of sources and the mask in Figure 4.1.

In Section 4.2, we study the angular power spectrum on smaller scales. With this, we test the assumption that the intrinsic clustering dipole is negligible which is made in [27]. Finally, a possible intrinsic dipole is included into the analysis and its impact on the significance discussed.

## 4.1 Dipole

To begin, we will discuss the amplitude the kinematic, intrinsic and shot noise dipole. To compute the expected kinematic dipole amplitude (2.13),  $x$  and  $\alpha$  are needed. Fitting a power law to the cumulative source counts at the flux cut corresponding to a cut of  $W1 < 16.4$  ( $W1$  is the magnitude in the  $3.4\mu\text{m}$  band) yields  $x = 1.75$ . Since the quasars are observed at different wavelengths, it is possible to estimate  $\alpha$  for each source by comparing the magnitude measurements at these wavelengths [27]. The mean value of the spectral

---

<sup>1</sup><https://zenodo.org/record/4448512>

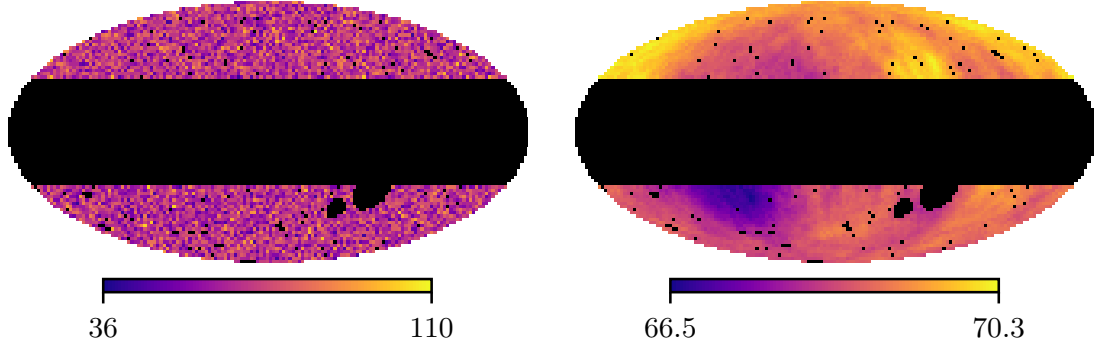


*Figure 4.1:* The distribution of quasars in galactic coordinates. The mask developed in [27] is shown as black pixels. It covers 53% of the sky. Most notable is the mask around  $\pm 30^\circ$  of the galactic plane. Galactic longitude and latitude are zero in the center. The former increases towards the left and the latter increases towards the top. *Left:* Number of sources per pixel in the final catalog.

*Right:* Each pixel shows the average of all unmasked pixels within  $20^\circ$  to make the dipolar distribution visible. The figure on the German title page shows the same data when averaged over all unmasked pixels within  $90^\circ$ , i.e. a full hemisphere.

index of all sources in the final catalog is  $\alpha = 1.26$ . Therefore, we can estimate the kinematic dipole amplitude to be

$$d_{\text{kin}} = [2 + x(1 + \alpha)]\beta \approx 7.4 \times 10^{-3}, \quad (4.1)$$

where  $\beta$  is again the velocity inferred from the CMB dipole (1.1).

In the original analysis, the intrinsic clustering dipole is estimated to be  $C_1^{\text{int}} = 8 \times 10^{-8}$ . Therefore, it is claimed that typical intrinsic clustering dipole  $d_{\text{int}} = \sqrt{9C_1^{\text{int}}/(4\pi)} = 2.4 \times 10^{-4}$  is negligible compared to the kinematic dipole amplitude. As we have seen in Section 3.2.1, the amount of local sources strongly influences the intrinsic dipole. Therefore, even though the sources are in general very distant,  $z \sim 1$ , it might be possible that there are some local sources leading to a notable clustering. Nevertheless, we first follow the original analysis neglecting the intrinsic clustering dipole. This topic will be addressed in Section 4.2.

With a total amount of  $N_{\text{tot}} = 1.3 \times 10^6$  sources distributed on  $f_{\text{sky}} = 47\%$  of the sky, the shot noise dipole is approximately (see (2.40) and (2.42))

$$d_{\text{SN}} \gtrsim 2.6 \times 10^{-3}. \quad (4.2)$$

The observed quasar dipole amplitude and deviation angle between the dipole and the CMB dipole are found with the estimator from Section 2.7

$$d = 1.55 \times 10^{-2} \quad (4.3)$$

$$\theta = 27.8^\circ \quad (4.4)$$

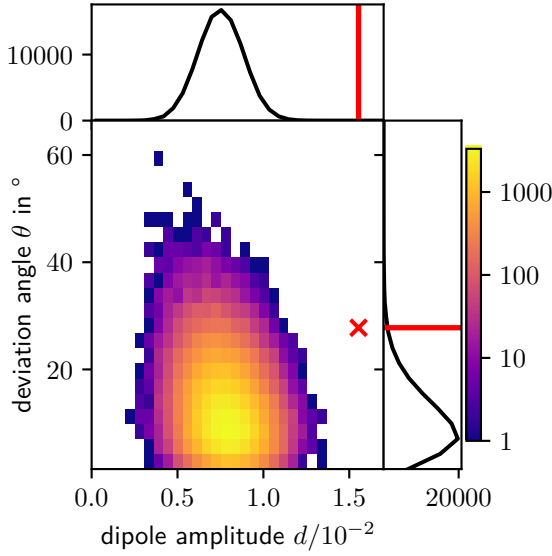


Figure 4.2: The distribution of the dipole amplitudes  $d$  and the deviation angles  $\theta$  between the kinematic dipole and the resulting dipole of  $10^5$  simulations in a logarithmic scale. The side panels show the distributions  $P(d)$  and  $P(\theta)$ , respectively. The dipole observed in the quasar sample is marked with a red cross in the main panel and with red lines in the side panels.

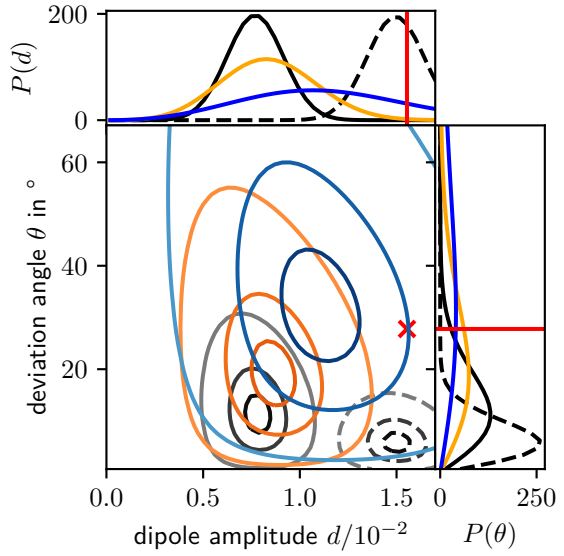
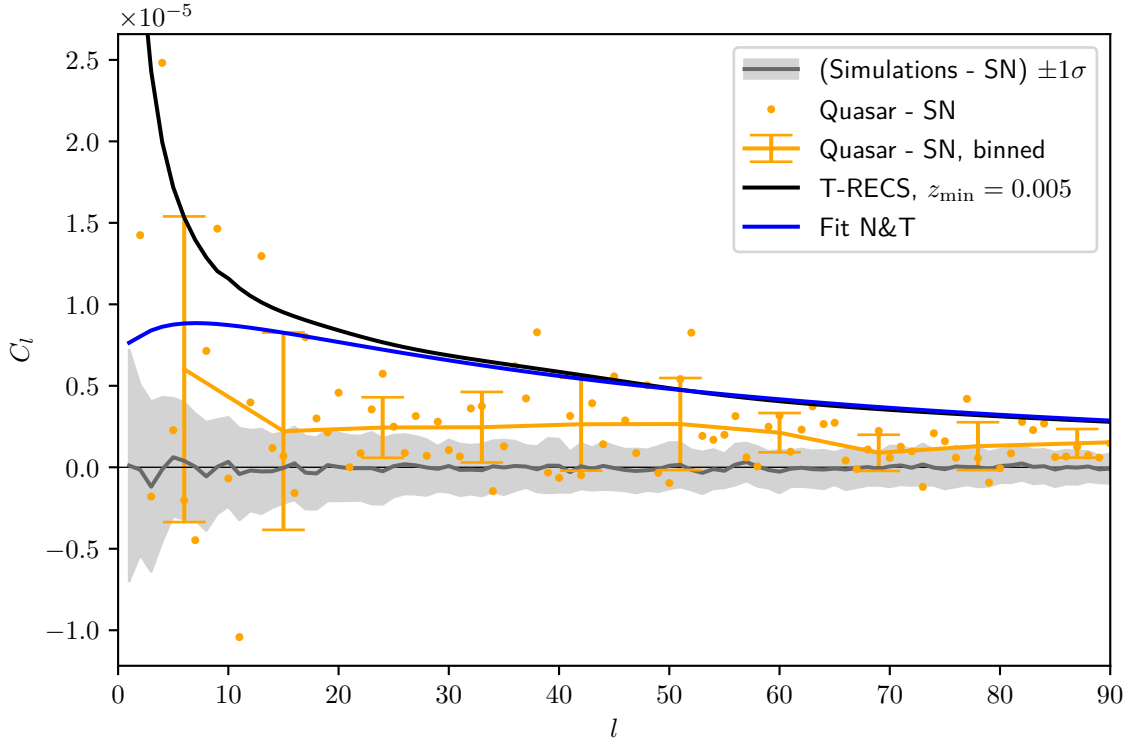


Figure 4.3: The PDF of dipole amplitudes and deviation angles  $P(d, \theta)$  (2.54) with  $d_{\text{kin}} = 7.4 \times 10^{-3}$ ,  $\sigma_{\text{SN}} = 1.5 \times 10^{-3}$  and  $\sigma_{\text{int}} = 3\tilde{C}^{\text{int}}/4\pi$ , where  $\tilde{C}^{\text{int}}$  is zero (black),  $2 \times 10^{-5}$  (orange) and  $10^{-4}$  (blue). The black dashed line shows  $P(d, \theta)$  for zero intrinsic clustering but twice the CMB velocity, thus  $d_{\text{kin}} = 14.8 \times 10^{-3}$ . The red cross and the red lines in the side panels mark the dipole observed in the distribution of quasars. Each set of three lines shows the contours where  $P(d, \theta)$  is 90%, 60% and 13% of its maximum.

For comparison, we simulate  $10^5$  mock catalogs using the methods described in Section 3.2.2. The resulting distribution of the dipole amplitudes and deviation angles found in the mocks is shown in Figure 4.2. The dipole amplitude observed in the data clearly exceeds the expectation. An amplitude as large as the observed one was not found in any mock catalog. Also, the deviation angle is larger than expected. To evaluate the significance, we focus on the excess in amplitude and fit the probability density function from equation (2.56) to the distribution of mock amplitudes. The fitted values are  $d_{\text{kin}} = 7.3 \times 10^{-3}$  and  $\sigma_r = 1.3 \times 10^{-3}$ , corresponding to  $d_{\text{SN}} = \sqrt{3}\sigma_r = 2.3 \times 10^{-3}$ , in good agreement with equations (4.1) and (4.2). The remaining difference in the shot noise dipole amplitude is due to the effect of masking. Integrating the fitted probability function, we find that an amplitude as large as the one found in the quasar sample only occurs with a probability of  $p = 8 \times 10^{-8}$ , corresponding to  $6\sigma$ . This is an even stronger disagreement than the one found in [27].



*Figure 4.4:* The angular power spectrum observed in the distribution of quasars after subtracting the simulated shot noise (with the same mask and number of sources as the quasar sample). The grey line and grey band show mean and standard deviation of the angular power spectrum of 100 simulations after subtracting their mean. The dots show each multipole of the quasar distribution. The error bars show the mean and standard deviation of 9 neighboring multipoles, starting with  $l = 2$ . The dipole is not included, its value minus shot noise is  $C_1 = 26 \times 10^{-5}$ . For comparison, we show the angular power spectra used in the NVSS dipole analysis from the right panel of Figure 3.5.

## 4.2 Intrinsic Clustering

To test the assumption that the intrinsic dipole and hence clustering is negligible, we examine the higher multipoles of the angular power spectrum of the quasar distribution. Using the same method as in Section 3.4 and the estimator described in Appendix C, we find an angular power spectrum which is shown in Figure 4.4. Even though the estimator is not very precise for individual multipoles, we can estimate the average of the multipoles after subtracting the shot noise contribution to be

$$2 \leq l \leq 10 : \quad \langle C_l \rangle \approx 6 \times 10^{-6} \quad (4.5)$$

$$10 < l \leq 64 : \quad \langle C_l \rangle \approx 2.3 \times 10^{-6} \quad (4.6)$$

$$64 < l < 90 : \quad \langle C_l \rangle \approx 1.1 \times 10^{-6} \quad (4.7)$$

The observed dipole power is much larger with  $C_1 \approx 2.6 \times 10^{-4}$ . It is also worth noting that in the original data not shown here, a very large quadrupole with  $C_2 \approx 6 \times 10^{-4}$  is

observed. This is an artefact of the WISE scanning pattern which is corrected for in [27]. The correction which removes this quadrupole has nearly no effect on the dipole, since the quadrupole is symmetric and the mask is nearly symmetric under a parity transformation, whereas the dipole is antisymmetric.

Our estimate of the intrinsic angular power spectrum yields values much larger than the estimate of  $C_1 = 8 \times 10^{-8}$  made in [27]. Hence, neglecting the intrinsic clustering might not be a good approximation. Therefore, we study the impact of intrinsic clustering by using the formalism derived in Section 2.5. Motivated by Figure 4.4, multipoles with  $l < 10$  can be as large as  $10^{-5}$ . Including leakage from higher multipoles due to the partial sky coverage by a factor of  $1/f_{\text{sky}}$  as in (2.43), a realistic choice of the intrinsic clustering is  $\tilde{C}_1^{\text{int}} = 2 \times 10^{-5}$ . Using equation (2.54), we plot the resulting PDF  $P(d, \theta)$  in Figure 4.3. Additionally, we also show the case if the intrinsic clustering is even larger than expected,  $\tilde{C}_1^{\text{int}} = 10^{-4}$ . For  $\tilde{C}_1^{\text{int}} = 0$ ,  $\tilde{C}_1^{\text{int}} = 2 \times 10^{-5}$  and  $\tilde{C}_1^{\text{int}} = 10^{-4}$ , amplitudes larger than the observed one are expected with a probability of  $p = 4.8 \times 10^{-8}$ ,  $p = 2.2 \times 10^{-3}$  and  $p = 0.13$ , corresponding to  $5.3\sigma$ ,  $2.8\sigma$  and  $1.1\sigma$ , respectively.

In summary, we find that care needs to be taken when there is the possibility of local structure that causes a large intrinsic dipole. By including a realistic intrinsic dipole into the analysis, the tension between the fundamental assumptions of the  $\Lambda$ CDM model and the dipole observed in the quasar distribution is alleviated from over  $5\sigma$  to  $2.8\sigma$ . A 5 times larger clustering dipole power of order  $\tilde{C}_1^{\text{int}} \sim 10^{-4}$  would be necessary to completely explain the excess in dipole amplitude.

Another possible explanation for the excess in dipole amplitude is that the velocity is larger than expected through the kinematic interpretation of the CMB dipole. In Figure 4.3, we show the expectations if we were moving with twice the velocity inferred from the CMB dipole. One can see that to be consistent with the observed deviation angle, the direction of motion would have to be different than the CMB dipole direction by  $\approx 30^\circ$ . In order to be consistent with the observation of the CMB dipole, there would have to be an equally large  $\sim 10^{-3}$  intrinsic CMB dipole to compensate the kinematic dipole, which is not expected within the  $\Lambda$ CDM model.

With this kind of analysis, it is not possible to decide which of these two resolutions, a larger amount of clustering or a different velocity vector is the true one. The method presented in the next chapter is aimed to resolve this issue.

# 5 New Method with Weighted Dipoles

Elaborating on an idea suggested in [15], this chapter presents a new method to separate the kinematic dipole from the intrinsic clustering dipole. As we have seen in the analysis of the distribution of NVSS radio sources and CatWISE quasars, the intrinsic dipole can strongly influence the number count dipole analysis. Especially so, if there are no redshift measurements of the sources and the amplitude of the intrinsic dipole is hence hardly known. Therefore it is of great advantage if the intrinsic dipole can be distinguished and measured independently of the kinematic dipole.

In [15], the dipole in sky brightness was computed, i.e. the dipole in the distribution of sources weighted by their flux. In both this dipole and the number count dipole, the intrinsic dipole is the same. In contrast, the kinematic dipole enters differently, as we will discuss in the following section. Measuring both the dipole in sky brightness and the dipole in number counts, they can be used to infer the kinematic contributions to the dipole, and thus our velocity  $\beta$ , and the intrinsic dipole  $\mathbf{d}_{\text{int}}$  independently. As it turns out, the kinematic dipole in sky brightness is very similar to the kinematic dipole in the number counts. This is a consequence of the cumulative number density above a flux threshold  $N(> F) \propto F^{-x}$  following a power law very closely (see Eq. 11 in [15]). We will discuss in Section 5.4 and Section 5.6, why therefore, the uncertainty in estimating  $\beta$  and  $\mathbf{d}_{\text{int}}$  is large.

In this work, the idea is extended by using that not only the flux and the positions of the sources are affected by Doppler effects and aberration, which leads to the kinematic number count dipole, but also other properties are measured differently by a moving observer. These other properties are used to gain more information about the intrinsic dipole and our velocity.

## 5.1 Possible Weights

To begin, we list the effects of our motion on some other properties than the flux and the observed position. The Doppler boost of the flux and the aberration have been studied in Section 2.1. As before, observed quantities are denoted as the bare variables, while quantities in the rest frame of the source are indicated so explicitly.

The redshift  $z$  of a source in direction  $\hat{\mathbf{n}}$  is changed because of the Doppler effect,  $(1+z) = \delta^{-1}(\hat{\mathbf{n}})(1+z_{\text{rest}})$ , where we define the factor

$$\delta(\hat{\mathbf{n}}) = (1 + \beta \cos \theta) / \sqrt{1 - \beta^2} \quad (5.1)$$

and  $\cos \theta = \hat{\boldsymbol{\beta}} \cdot \hat{\mathbf{n}}$  as usual. Spectroscopic or photometric redshift measurements thus yield biased results in different directions because of our local motion. This is one of the signals that we use in the following to distinguish the kinematic from the intrinsic dipole.

Also, the projected angular size of a source is changed because of special relativistic aberration as can be seen in (2.5), so  $A = \delta^{-2}(\hat{\mathbf{n}})A_{\text{rest}}$ . This similarly concerns the projected one dimensional extension of a source. We refer to it as the length  $L$ , the angle under which a one dimensional object is seen on the sky. If  $L \ll 1$ , then the aberrated length is  $L = \delta^{-1}(\hat{\mathbf{n}})L_{\text{rest}}$  to first order in  $\beta$ . To see this, let us consider a small one dimensional source whose centre is positioned at an angle  $\theta_{\text{rest}}$  to the direction of motion. The source's endpoints are defined to be  $\theta_{\text{rest}}^1$  and  $\theta_{\text{rest}}^2$  and lie in the plane spanned by the midpoint of the source and the direction of motion (in other words the azimuthal angles of the two endpoints are the same). The rest frame length of the source is  $L_{\text{rest}} = \theta_{\text{rest}}^1 - \theta_{\text{rest}}^2$ . To lowest order in  $\beta$ , the two endpoints are aberrated like  $\theta^{1,2} = \theta_{\text{rest}}^{1,2} - \sin \theta_{\text{rest}}^{1,2} \beta$ . To lowest order in  $L$  and  $\beta$ , the observed length is

$$L = \theta^1 - \theta^2 = L_{\text{rest}}(1 - \beta \cos \theta). \quad (5.2)$$

Since we know that the area is changed to lowest order by the factor  $(1 - 2\beta \cos \theta)$  from (2.5), we can conclude that a source oriented perpendicular to the one we just examined (endpoints at same angle  $\theta$  but at different azimuthal angle) must change in the same way (5.2). For  $L \ll 1$ , the length of a source oriented in any direction can be written with these two orthogonal directions. Hence, it must follow for all sources that for a moving observer, their one dimensional extension is changed by  $(1 - \beta \cos \theta)$  for  $L \ll 1$ .

We summarize how flux, redshift and length are changed due to our motion depending on the angle  $\theta$  between our direction of motion and the direction of observation:

$$\begin{aligned} \{F, 1+z, L\} &= \delta_{F,z,L}(\hat{\mathbf{n}})\{F, 1+z, L\}_{\text{rest}} \\ \delta_F(\hat{\mathbf{n}}) &= \delta(\hat{\mathbf{n}})^{1+\alpha} \approx 1 + (1+\alpha)\beta \cos \theta \\ \delta_z(\hat{\mathbf{n}}) &= \delta(\hat{\mathbf{n}})^{-1} \approx 1 - \beta \cos \theta \\ \delta_L(\hat{\mathbf{n}}) &= \delta(\hat{\mathbf{n}})^{-1} \approx 1 - \beta \cos \theta. \end{aligned} \quad (5.3)$$

From the second line of this equation also follows for the apparent magnitude  $m = -2.5 \log(F/F_0)$  defined by some reference flux  $F_0$  that

$$m = m_{\text{rest}} - 2.5 \log \delta_F(\hat{\mathbf{n}}) \approx m_{\text{rest}} - \frac{2.5}{\ln 10} (1+\alpha)\beta \cos \theta. \quad (5.4)$$

There may also be other observables that are interesting to consider (for example flux measurements at various frequencies where the spectral indices  $\alpha$  are different) but we focus

on these four only. In the next section, the field of sources weighted by these properties and its dipole are studied.

## 5.2 Weighted Dipole

Let us consider the distribution of sources weighted by some function  $W$ , which can depend on any combination of properties that are measured for each source. Thereby, we extend the number density  $dN/d\Omega(\hat{\mathbf{n}})$  to the weighted field

$$\frac{dN_W}{d\Omega}(\hat{\mathbf{n}}) \equiv \int_{\text{cut}} \frac{dN}{d\Omega}(\hat{\mathbf{n}}, F, z, L, \dots) W(F, z, L, \dots) \quad (5.5)$$

$$= \sum_{i \in \text{cut}} W_i(F_i, z_i, L_i, \dots) \delta(\hat{\mathbf{n}}_i - \hat{\mathbf{n}}) \quad (5.6)$$

$$= (1 + \mathbf{d}^W \cdot \hat{\mathbf{n}}) \bar{N}_W + \mathcal{O}(n_j^2). \quad (5.7)$$

Here, we denote as  $dN/d\Omega(\hat{\mathbf{n}}, F, z, L, \dots)$  the observed number density of sources in a direction  $\hat{\mathbf{n}}$  per flux, per redshift, per length and possibly other properties. To indicate the density of all sources independent of direction, we use  $n(F, z, L, \dots) = \int d\Omega dN/d\Omega(\hat{\mathbf{n}}, F, z, L, \dots)$ . The integral in (5.5) implicitly includes all the cuts in any of the observed properties, i.e. one integrates over the range of properties within all possible thresholds, which usually include at least a minimum flux cut. Equivalently, the sum runs over all sources within the cuts. From this sum, by averaging over small angular regions, the field  $dN_W/d\Omega(\hat{\mathbf{n}})$  can be reconstructed from observations. Of all the anisotropies in this weighted field, only the weighted dipole  $\mathbf{d}^W$  is of interest to us and higher multipoles  $\mathcal{O}(n_j^2)$  are ignored.

For  $W = 1$ , the weighted field reduces to the number density and the weighted dipole to the number count dipole studied in Chapter 2,  $\mathbf{d}^{W=1} = \mathbf{d}^N$ . The case  $W = F$  corresponds to the dipole in sky brightness, which was first computed in [12] and is also described in [15]. Both the number count dipole and any weighted dipole contain a kinematic contribution, the intrinsic clustering dipole and a random shot noise dipole

$$\mathbf{d}^N = \mathbf{d}_{\text{kin}}^N + \mathbf{d}_{\text{int}} + \mathbf{d}_{\text{SN}}^N \quad (5.8)$$

$$\mathbf{d}^W = \mathbf{d}_{\text{kin}}^W + \mathbf{d}_{\text{int}} + \mathbf{d}_{\text{SN}}^W. \quad (5.9)$$

Of the three contributions, the intrinsic dipole is the only one that is equal in both expressions, because both include the exact same sources and their clustering. Here, we neglect an intrinsic dipole in the weights and correlations between the intrinsic clustering in the number density and the weights. In short, we assume that a source's weight is independent of its position. This is addressed in Section 5.7, arguing that this approximation is sufficient for the applications that we consider. Although both dipoles contain the same sources, the respective contributions from shot noise are different because of the randomness in the weights (see Section 5.4).

The kinematic contribution to the number count dipole and the one to the weighted dipole both point in the same direction as our velocity  $\beta$ . Their amplitudes, however, can differ.

Next to the intrinsic dipole being present equally in both dipoles, this is the key idea behind introducing the weighted dipole. As the simplest example, we consider every source to have the same property  $y_{\text{rest}}$  in their rest frame and through Doppler effects, a moving observer sees  $y = \delta_y(\hat{\mathbf{n}})y_{\text{rest}}$ , where  $\delta_y(\hat{\mathbf{n}}) = (1 + \mathbf{d}_y \cdot \hat{\mathbf{n}})$  is known from special relativity, like for the quantities in (5.3). Since  $y_{\text{rest}}$  is the same for all sources, when weighting by  $W = y$ , (5.5) becomes

$$\frac{dN_W}{d\Omega}(\hat{\mathbf{n}}) = y \int_{\text{cut}} \frac{dN}{d\Omega}(\hat{\mathbf{n}}, F, z, L, \dots) = y_{\text{rest}} \delta_y(\hat{\mathbf{n}}) \frac{dN}{d\Omega}(\hat{\mathbf{n}}) \quad (5.10)$$

To first order in the dipoles, we find  $\mathbf{d}_{\text{kin}}^W = \mathbf{d}_y + \mathbf{d}_{\text{kin}}^N$ . Since we know how  $\mathbf{d}_y \equiv B^y \boldsymbol{\beta}$  depends on our velocity, by measuring  $\mathbf{d}^N$  and  $\mathbf{d}^W$ , we can infer  $\boldsymbol{\beta}$  by the difference of these two dipoles divided by  $B^y$  (compare to (5.8) and (5.9)). In this ideal example, the shot noise in the number count field and the weighted field is also the same, which allows to determine  $\boldsymbol{\beta}$  shot noise free.

True source properties differ from such an ideal weight  $y$  in two ways. First, the possible properties of the sources all correlated to some extent. This makes it more difficult to predict the amplitude of the kinematic dipole analytically. Compared to the number count dipole, where one fits  $N(> F) \propto F^{-x}$  to the data and thereby models  $n(F) \propto F^{-x-1}$ , here, one would have to model and fit how the number density depends on all the properties used in the weight function.

Secondly, there is no weight that is the same for all sources in the rest frame and at the same time affected by Doppler effects or aberration. If there was, then the shot noise dipoles in  $\mathbf{d}^N$  and  $\mathbf{d}^W$  would be the same and the velocity could be determined shot noise free. We illustrate this by considering the correlation between redshift and flux as an example. Redshifts are anticorrelated with flux, but not to 100%. If there was a one to one map between flux and redshift, then one could construct a weight of these two properties, which is equal for all sources in the rest frame but also changed due to our velocity, similar to the ideal weight  $y$ . Obviously, not all the sources are equally luminous and this one to one map does not exist. This intrinsic randomness is the cause of the remaining shot noise, which will be computed in Section 5.4.

Next, we discuss how to compute the expected kinematic dipole of the weighted dipole  $\mathbf{d}_{\text{kin}}^W$ , when it is not possible to give an analytic expression for it. The expected direction of  $\mathbf{d}_{\text{kin}}^W$  is known, so we need to find only the amplitude  $B^W$  defined by  $\mathbf{d}_{\text{kin}}^W = B^W \boldsymbol{\beta}$ . We also introduce  $\mathbf{d}_{\text{kin}}^N = B^N \boldsymbol{\beta}$ , where we know that  $B^N = 2 + (1 + \alpha)x$  from (2.12). However, as mentioned above, it is not possible to find an analytic expression for  $B^W$  without assuming how  $n(F, z, L, \dots)$  depends on the flux, redshift, length... Instead, one can find the amplitudes by computing (5.6) numerically. Even though the observed properties of the sources already contain the effects of our motion and some measurement error, to do so, we assume that the observed source density  $n(F, z, L, \dots)$  is close to the one in the rest frame. In Section 5.5, we will see how measurement errors break this assumption and can lead to a bias in the computed amplitudes and thus also in the estimated quantities  $\boldsymbol{\beta}$  and  $\mathbf{d}_{\text{int}}$ . Note that this is also the case for the kinematic dipole in number counts. There, one fits the slope of the cumulative source count, which is also only reliable when the fluxes are measured accurately.

We find  $B^W$  and  $B^N$  by boosting the observed sources properties with an artificial velocity  $\beta_{\text{test}}$  accordingly to (5.3) and computing the value of the weighted field in the forward (+) and backward (-) direction

$$N_W^\pm = \sum_{i \in \text{cut}} W_i (\delta_F^\pm F_i, \delta_z^\pm z_i, \delta_A^\pm L_i), \quad (5.11)$$

where  $\delta_{F,z,L}^\pm = \delta_{F,z,L}(\hat{\mathbf{n}} = \pm \hat{\beta}_{\text{test}})$ . The implicit cut is imposed after boosting the sources in the two different directions, respectively. This is why for finding  $B^N$ , i.e. for  $W = 1$ ,  $N^+$  and  $N^-$  also differ. We then compute the expected amplitude as

$$B^W = \frac{N_W^+ - N_W^-}{N_W^+ + N_W^-} \beta_{\text{test}}^{-1} + 2, \quad (5.12)$$

where the last term comes from the aberration (2.5).

Being able to compute the kinematic dipole amplitudes we now proceed to construct estimators to measure the speed and the direction of our motion as well as amplitude and direction of the intrinsic clustering dipole separately.

### 5.3 Velocity and Intrinsic Dipole Estimators

In order to measure the weighted dipole  $\mathbf{d}_W$  in the field  $N_W(\hat{\mathbf{n}})$ , we generalize the estimator introduced in Section 2.7 to weight every observed source  $i$  with the quantity  $W_i(F_i, z_i, L_i, \dots)$ . The estimator for the weighted dipole is obtained by simply replacing number of sources per pixel  $N_p$  with  $w_p = \sum_{i \in p} W_i$ , i.e. the sum of the weights of all the sources in the pixel  $p$ .

Defining  $\Delta = B^W - B^N$  as the difference between the kinematic dipole amplitudes, we introduce the estimators for our velocity and the intrinsic dipole

$$\beta_{\text{est}} = \frac{\mathbf{d}_{\text{est}}^W - \mathbf{d}_{\text{est}}^N}{\Delta} \quad (5.13)$$

$$\mathbf{d}_{\text{est}}^{\text{int}} = \frac{B^W \mathbf{d}_{\text{est}}^N - B^N \mathbf{d}_{\text{est}}^W}{\Delta}. \quad (5.14)$$

Comparing with equations (5.8) and (5.9), the two estimators eliminate the corresponding other contribution as desired. However, the shot noise is not removed and we will calculate the resulting shot noise in the next section.

### 5.4 Shot Noise

As can be seen by comparing (5.5) to (5.7) with (5.13), to estimate our velocity, we are actually looking for the dipole in the field

$$\beta(\hat{\mathbf{n}}) \equiv \frac{1}{\bar{N}\Delta} \left( \bar{W}^{-1} \frac{dN_W}{d\Omega}(\hat{\mathbf{n}}) - \frac{dN}{d\Omega}(\hat{\mathbf{n}}) \right) = \frac{1}{\bar{N}\Delta} \sum_i \delta(\hat{\mathbf{n}}_i - \hat{\mathbf{n}}) \left( \frac{W_i}{\bar{W}} - 1 \right). \quad (5.15)$$

The dipole of this field is  $\beta$  plus a shot noise contribution. The amplitude of the shot noise is found by calculating the constant angular power spectrum of  $\beta(\hat{\mathbf{n}})$  which we call  $C_\beta^{\text{SN}}$ . To do so, we extend the calculation of Section 2.3 to the general field  $f(\hat{\mathbf{n}}) = \sum_i \delta(\hat{\mathbf{n}}_i - \hat{\mathbf{n}}) f_i / \bar{N}$ , where any two of all  $f_i$  and  $\hat{\mathbf{n}}_j$  are uncorrelated. Its angular power spectrum for  $l \geq 1$  is

$$C_l = \frac{1}{2l+1} \sum_m \sum_{i,j} \langle Y_{lm}(\hat{\mathbf{n}}_i) Y_{lm}^*(\hat{\mathbf{n}}_j) f_i f_j \rangle / \bar{N}^2 = \langle f^2 \rangle / \bar{N}. \quad (5.16)$$

For  $f_i = 1$ , we recover (2.39),  $C_l^{\text{SN}} = 1/\bar{N}$ . For the velocity,  $f_i = (W_i/\bar{W} - 1)/\Delta$  and we find

$$C_\beta^{\text{SN}} = \left( \frac{\sigma_W}{\bar{W}\Delta} \right)^2 \frac{1}{\bar{N}}. \quad (5.17)$$

Using the results from Section 2.5, in particular (2.57) replacing  $\sigma_r^2$  with  $3C_\beta^{\text{SN}}/4\pi$  and  $d_{\text{kin}}$  with  $\beta_{\text{CMB}}$ , the mean and standard deviation of  $\beta_{\text{est}}$  are

$$\begin{aligned} \langle \beta_{\text{est}} \rangle &= \sqrt{\frac{3C_\beta^{\text{SN}}}{8}} L_{1/2}^{1/2} \left( -\frac{2\pi\beta_{\text{CMB}}^2}{3C_\beta^{\text{SN}}} \right) \approx \sqrt{\frac{6}{\pi^2} C_\beta^{\text{SN}} + \beta_{\text{CMB}}^2} \\ \sigma_\beta^2 &= \frac{9}{4\pi} C_\beta^{\text{SN}} + \beta_{\text{CMB}}^2 - \langle \beta_{\text{est}} \rangle^2 \sim 0.11 C_\beta^{\text{SN}}. \end{aligned} \quad (5.18)$$

This tells us about the bias and the uncertainty of the velocity estimator. Notice that there is no contribution from intrinsic clustering.

The shot noise in estimating  $\beta$  is different from the one of the dipole in number counts (2.39) by a factor  $\sigma_W/(\bar{W}\Delta)$ . Therefore, we are looking for a weight function  $W(F, z, L, \dots)$ , that when evaluated for all sources has a small spread (small  $\sigma_W/\bar{W}$ ) and at the same time gives a large difference  $\Delta$  between the two dipole amplitudes. We define the norm of this important quantity as

$$\Delta_W \equiv \left| \Delta \frac{\bar{W}}{\sigma_W} \right|, \quad (5.19)$$

so the shot noise in the velocity field is simply  $C_\beta^{\text{SN}} = 1/(\bar{N}\Delta_W^2)$ . The typical shot noise contribution to  $\beta$  is  $3/(\Delta_W\sqrt{N_{\text{tot}}})$ , given a total number of  $N_{\text{tot}}$  sources. The signal to noise ratio, which is

$$S/N = \Delta_W \beta \sqrt{N_{\text{tot}}}/3, \quad (5.20)$$

can not only be optimised by modifying the weight function, but also by adjusting the cuts that are applied to the data, for example the minimum and maximum flux. Here, the trade-off is between cuts that constrain the range of possible weights leading to a small variance (large  $\Delta_W$ ) and the resulting smaller number of sources  $N_{\text{tot}}$ .

For the shot noise in the intrinsic dipole estimator, we use (5.16) with  $f_i = (B^W - B^N W_i/\bar{W})/\Delta$  and find

$$C_{\text{int}}^{\text{SN}} = \frac{1}{\bar{N}} \left[ 1 + \left( \frac{B^N}{\Delta_W} \right)^2 \right] \quad (5.21)$$

and with that

$$\begin{aligned} \langle d_{\text{est}}^{\text{int}} \rangle &= \sqrt{\frac{3C_{\text{int}}^{\text{SN}}}{8}} L_{1/2}^{1/2} \left( -\frac{2\pi d_{\text{int}}^2}{3C_{\text{int}}^{\text{SN}}} \right) \approx \sqrt{\frac{6}{\pi^2} C_{\text{int}}^{\text{SN}} + d_{\text{int}}^2} \\ \sigma_{\text{int}}^2 &= \frac{9}{4\pi} C_{\text{int}}^{\text{SN}} + d_{\text{int}}^2 - \langle d_{\text{est}}^{\text{int}} \rangle^2 \sim 0.11 C_{\text{int}}^{\text{SN}}. \end{aligned} \quad (5.22)$$

To clarify, the quantity  $C_{\text{int}}^{\text{SN}}$  is not related at all to the intrinsic angular power spectrum. Rather, it is the shot noise power spectrum of the field that we use to estimate  $\mathbf{d}_{\text{int}}$ . The same applies to  $C_{\beta}^{\text{SN}}$ .

We are also able to calculate how much the estimated directions of the velocity and the intrinsic dipole deviate from the respective true values by using (2.58), respectively. This requires to simply replace  $d_{\text{kin}}$  with  $\beta_{\text{CMB}}$  and  $\sigma_r^2$  with  $3C_{\beta}^{\text{SN}}/(4\pi)$  for the deviation angle of the velocity as well as  $d_{\text{kin}}$  with the expected intrinsic dipole amplitude  $d_{\text{int}}$  and  $\sigma_r^2$  with  $3C_{\text{int}}^{\text{SN}}/(4\pi)$  for the deviation angle of the intrinsic dipole. With that one obtains expressions for

$$\langle \theta_{\beta} \rangle, \quad \langle \theta_{\text{int}} \rangle, \quad (\sigma_{\theta}^{\beta})^2 \quad \text{and} \quad (\sigma_{\theta}^{\text{int}})^2, \quad (5.23)$$

which we do not repeat here.

All the results in this section only hold for a full sky coverage, but also serve as an approximation for partial sky coverages. This is discussed in Section 2.4 and we will come back to it when discussing the results in Section 5.8.

In the next sections, we forecast the precision with which we can measure both, the local velocity  $\beta$  and the intrinsic dipole  $\mathbf{d}_{\text{int}}$  using this weighting scheme in two different simulated sky surveys. We show how to find optimal weights to minimize the shot noise and confirm the calculations leading to (5.18), (5.22) and (5.23) by simulations.

## 5.5 Applications

We consider two applications, an optical survey with redshift measurements and a survey measuring the size of radio galaxies. We begin by describing how mock catalogs for the two applications are created. These mock catalogs are intended to contain all the relevant properties for the dipole analysis. In particular, the mocks are first created in the rest frame of the sources and afterwards, kinematic effects with the fiducial velocity  $\beta_{\text{CMB}}$  given by (1.1) are applied to each source. In contrast to the mock catalogs created for the NVSS and quasar analyses, where the kinematic effects are simulated on the number density in each pixel, here, each source is simulated individually. The mocks contain a realistic distribution of source properties, which are magnitudes and redshifts in the first application and fluxes and lengths in the second application. They also contain the intrinsic clustering through the angular power spectrum expected from the  $\Lambda$ CDM model as well as the respective survey sky coverages.

### 5.5.1 LSST/Euclid

We first consider an optical galaxy survey similar to Euclid [60] or the one planned with the Vera C. Rubin Observatory, the Legacy Survey of Space and Time (LSST) [61]. We let

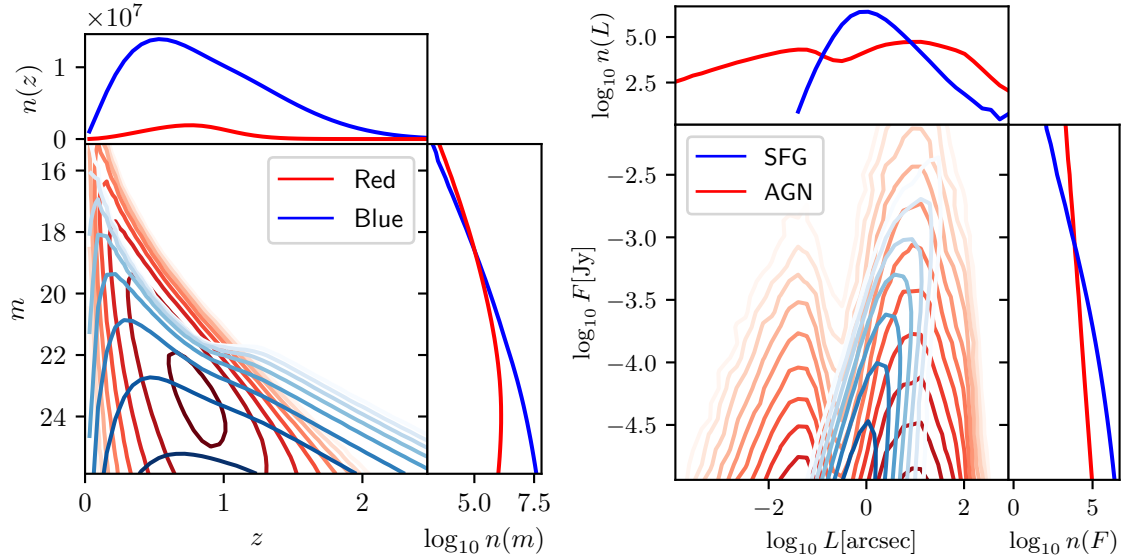


Figure 5.1: The source distributions for the two applications, LSST/Euclid (*left*) and SKA (*right*). The contour lines show equal values of the source density per redshift and magnitude  $n(z, m)$  and per length and flux  $n(L, m)$  in a logarithmic scale. The more transparent the line, the smaller the density. Additionally, the side panels show the projected source density integrated over one of the two parameters, respectively. On the right, one can recognize the two different models for the size of the AGN depending on the viewing angle as described in [52].

the number of observed galaxies  $N_{\text{tot}}$  vary. For each galaxy we assume that a magnitude in the AB system and redshift  $z$  is measured. We consider a measurement error of  $\sigma_z$  in the redshift to demonstrate how such an uncertainty affects the analysis. It can range from typical spectroscopic uncertainties with  $\sigma_z \approx 0.001(1+z)$  [60] to photometric uncertainties  $\sigma_z \approx (0.05-0.1)(1+z)$ . We use the same procedure to create the mock catalogs for the LSST as well as for the Euclid survey. To do so, models for the LSST are being used. The difference between the LSST and Euclid simulations is only in their sky coverages.

**Source properties** To create the mock catalogs we use the luminosity functions and redshift distributions modelled for the LSST described in [39] for blue and red galaxies. Their implementation which is used in this work is publicly available. In the following  $m$  refers to the r-band magnitude. We impose a magnitude limit of  $m_{\text{lim}} = 26$  [39]. The following procedure allows to create sources with a magnitude and a redshift such that the resulting distribution of sources respects the correlation between magnitude and redshift. We start by computing the redshift distribution  $n_{b,r}(z)$  for blue and red galaxies, respectively, and normalize them to yield in total  $N_{\text{tot}}$  galaxies. In 100 redshift bins between 0 and 3.5, for each galaxy type, we draw  $n_{b,r}(z)$  random absolute magnitudes accordingly to the respective luminosity function at the redshift. We force the random absolute magnitude to be larger than  $m_{\text{lim}}$ , when converted to the apparent magnitude (using the luminosity distance and including  $k$ -correction, see [39]). To each of these magnitudes, a random redshift in the corresponding bin sampled accordingly to  $n_{b,r}(z)$  is associated. The left panel of Figure 5.1 shows the resulting distribution of magnitudes and



Figure 5.2: From left to right: LSST, Euclid and SKA masks in equatorial coordinates with sky coverages of 40%, 38% and 61%, respectively. Grey indicates the observed regions and black the masked regions. The masks are described in the main text.

redshifts for such a catalog. From here on, we do not differentiate between red and blue galaxies.

**Mask** The LSST covers only the southern hemisphere in equatorial coordinates. Additionally, we mask the region within  $\pm 10^\circ$  of the galactic plane. We also study the case if the sources were distributed on the part of the sky observed by Euclid [60]. Our Euclid mask consists of the regions within  $\pm 20^\circ$  of the ecliptic plane and  $\pm 20^\circ$  of the galactic plane. The masks are shown in Figure 5.2. Both surveys have a similar sky coverage of approximately  $16\,000\text{ deg}^2$ , however Euclid observes more distinct directions than the LSST. As we have seen in Section 2.4, this is an advantageous property for the dipole analysis.

**Realizing the Mocks** We include the intrinsic large-scale clustering by computing the angular power spectrum and realizing a Gaussian density field on the sphere accordingly (similar to the procedure described in Section 3.2.2). A Gaussian realization is a good approximation because non-linearities have only a small ( $\sim \%$ ) effect on large scales (see Figure 3.2.1). The LSST angular power spectrum (see Figure 5.3) is calculated with CLASS using  $n(z) = n_b(z) + n_r(z)$  in the range  $z = 0$  to  $z = 3.5$ , the bias  $b(z) = 1 + 0.84z$ , the magnification bias and the evolution bias all from [39]. Again, this angular power spectrum is also used for the Euclid simulations.

To distribute the sources, first, a density field is realized from the multipoles with  $l < 64$  on the pixelised sky using healpy with  $N_{\text{side}} = 64$ , i.e. 49 152 pixels. The pixel values are normalized such that the sum over all the unmasked pixel values  $m_p$  yields  $N_{\text{tot}}$ . To include shot noise, each pixel value is replaced by a Poissonian random number with mean of the original pixel value

$$m_p \rightarrow \mathcal{P}(m_p). \quad (5.24)$$

In each pixel,  $m_p$  sources with random properties  $m$  and  $z$  as described above are distributed isotropically. Therefore, the realization includes clustering down to the scale of the resolution  $\sim 0.9^\circ$ .

So far, we have simulated a catalog in the rest frame of the sources. Next, we include the kinematic effects due to our motion by shifting each source positions according to the special relativistic aberration (2.4) (see Appendix A of [14] for the implementation) and boosting each redshift and magnitude according to (5.3) and (5.4). To do so, we model the frequency dependence of the magnitudes by the one of the flux  $F \propto \nu^{-\alpha_{\text{opt}}}$  (see discussion in Section 2.1). We assume that the distribution of  $\alpha_{\text{opt}}$  is known, for example

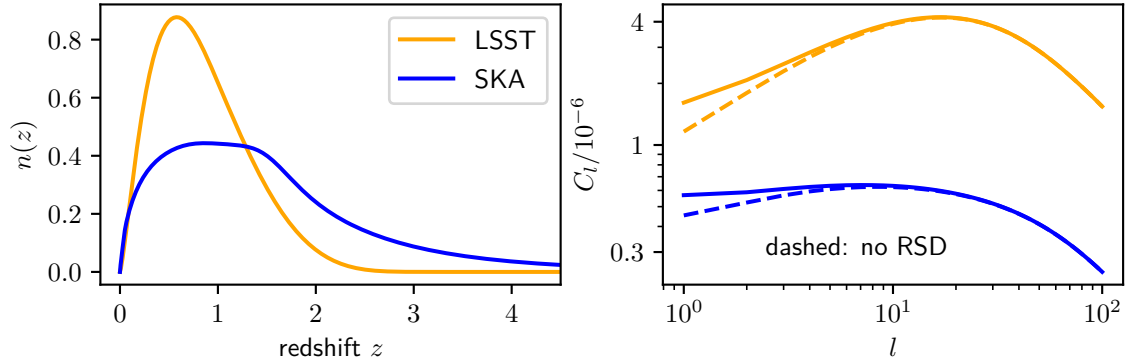


*Figure 5.3: Left:* The expected redshift distribution of the LSST sources and the SKA sources.

*Right:* The expected angular power spectrum for LSST and SKA (calculated with CLASS and following [39]). For the simulations, we only use  $l < 64$ . Also shown is the angular power spectrum not including redshift space distortions (RSD) as dashed lines. This stresses again their important contribution on large scales of nearly 30%.

from measurements of the magnitude in different frequency bands. Motivated by the colors shown for example in [62], we simply fix  $\alpha_{\text{opt}} = 1$ . With that, we include the kinematic effects by setting for each source (see (5.3) and (5.4))

$$z + 1 \rightarrow (z + 1)\delta^{-1}(\hat{\mathbf{n}}) \quad (5.25)$$

$$m \rightarrow m - 2.5 \log \delta(\hat{\mathbf{n}})^{1+\alpha_{\text{opt}}}. \quad (5.26)$$

Finally, redshift measurement errors are simulated by replacing the redshift for each source with the absolute value of a random normal variable  $z \rightarrow |\mathcal{N}(z, \sigma_z)|$ . The absolute value is used to avoid negative redshifts. Only afterwards, cuts are applied. For the main analysis, we use a slightly smaller magnitude limit than  $m_{\text{lim}} = 26$  so that there are no boundary effects and all redshifts

$$m < 25.9, \quad \text{all } z. \quad (5.27)$$

In Section 5.8, we touch on the possibility of a minimum redshift cut.

### 5.5.2 SKA

We also consider the radio continuum survey of the SKA [63]. We use the measurements of the flux  $F$  and the projected size of the major axis of the observed sources. We refer to the latter as the length  $L$ . Since  $L$  is the most critical measurement, we include an uncertainty  $\sigma_L$ , that ranges from  $\sigma_L = 0.1$  arcsec to  $\sigma_L = 1$  arcsec motivated by the resolution at 1.4GHz of 0.3 arcsec [63].

**Source properties** As a model of the observed sources, the T-RECS simulations [52] are used. In their simulation, the flux and size of active galactic nuclei (AGN) and star forming galaxies (SFG) are modelled. We use all the AGN and SFG above  $9\mu\text{Jy}$  at 0.7GHz in the 'wide catalogue' of T-RECS. For the AGN, we use the projected apparent size of the

core+jet emission as the length  $L$ . For the SFG, we use twice the half light radius  $r_{\text{SFG}}$ , i.e.  $L = 2 \times r_{\text{SFG}}$ . Observationally, both of these quantities correspond to the fitted major diameter, independent of the source type. For each mock realization, we draw  $N_{\text{tot}}$  random tuples of flux and size from the combined data set of SFG and AGN (see Figure 5.1). From here on, AGN and SFG are not distinguished.

**Mask** We use the maximum possible sky coverage expected by the SKA survey, masking the region above the equatorial declination of  $30^\circ$  and the region within  $\pm 10^\circ$  of the galactic plane [28] (see Figure 5.2).

**Realizing the mocks** The angular power spectrum is calculated with CLASS (see Figure 5.3). Redshift distribution, bias, magnification bias and evolution bias are all modelled with the public code developed in [39]. With the angular power spectrum, a Gaussian density field is realized as described for the LSST/Euclid mocks. The kinematic effects (5.3) are included by aberrating all positions and by boosting the flux and size of each source

$$F \rightarrow F\delta(\hat{\mathbf{n}})^{1+\alpha_{\text{SKA}}} \quad (5.28)$$

$$L \rightarrow L\delta(\hat{\mathbf{n}})^{-1} \quad (5.29)$$

with  $\alpha_{\text{SKA}} = 0.75$  [63]. Unbiased measurement errors are included by replacing each length with a random normal variable  $L \rightarrow \mathcal{N}(L, \sigma_L)$ . Only afterwards, cuts to length and flux are applied. In this case, we choose

$$0.3 < L[\text{arcsec}] < 100, \quad 10^{-5} < F[\text{Jy}] < 10^{-2}. \quad (5.30)$$

The minimum length and minimum flux are imposed because of the limiting resolution and sensitivity of the telescope. The upper limits are chosen since they allow to find a better signal to noise ratio (5.20) by decreasing the variance in the weights (see Section 5.4).

## 5.6 Optimal Weights

As can be seen from (5.17), and (5.21), the shot noise in the estimation of both  $\beta$  and the intrinsic dipole  $\mathbf{d}_{\text{int}}$  is minimal when  $\Delta_W$  is maximal. The signal to noise ratio for estimating our velocity is given by (5.20)  $\text{S/N} = \Delta_W \beta_{\text{CMB}} \sqrt{N_{\text{tot}}}/3$ . To find an optimal estimator, we therefore look for a weight function  $W(z, m)$  (LSST/Euclid) and  $W(L, F)$  (SKA) for which  $\Delta_W$  is at its maximum. Even more generally, the cuts in the properties can be optimized and a larger signal to noise ratio might be found. However, this is not tested to a great extent in this work, where we settled for the cuts (5.27) and (5.30) after finding reasonable values for  $\Delta_W$  without discarding too many sources.

We begin with the LSST/Euclid mock catalogs. In principle, any function of the magnitude and redshift can be constructed. For simplicity, we only consider functions of the form  $W(z, m) = (1+z)^{x_z} m^{x_m}$ , weighting each source by a combination of its redshift and magnitude with the redshift exponent  $x_z$  and the magnitude exponent  $x_m$  as free param-

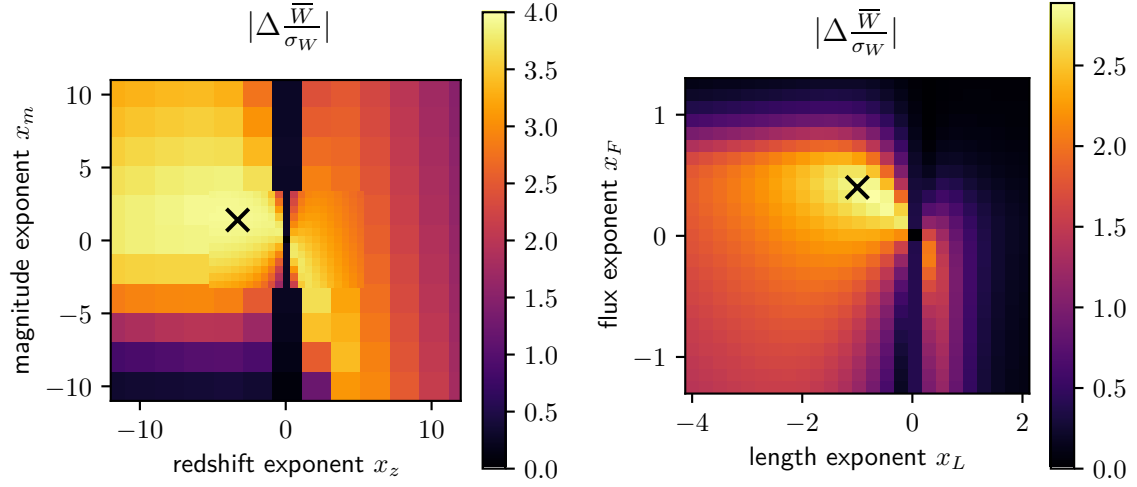


Figure 5.4:  $\Delta_W = |\Delta\bar{W}/\sigma_W|$ , the expected amplitude divided by the scatter in the weight for two different parameters of the weight function. This quantity is related to the signal to noise ratio by  $S/N = \Delta_W \beta_{\text{CMB}} \sqrt{N_{\text{tot}}}/3$ .

Left: LSST/Euclid: the weight function is  $W(z, m) = (1+z)^{x_z} m^{x_m}$ . The cross marks the maximum, which is found for  $x_z = -3.3$  and  $x_m = 1.4$ , where  $\Delta_W = 3.91$ .

Right: SKA: the weight function is  $W(L, F) = L^{x_L} F^{x_F}$ . The cross marks the maximum, which is found for  $x_L = -1$  and  $x_F = 0.4$ , where  $\Delta_W = 2.84$ .

eters. While this gives good enough results, one might try to search for more complex weight functions that gives even larger values of  $\Delta_W$ .

In the left panel of Figure 5.4, we show the value of  $\Delta_W$  for different exponents. One can clearly see that for  $x_z = 0$ , i.e. weighting only by the magnitude, this quantity is very small. This is related to the discussion from the beginning of this chapter. A power law in the source count per flux interval  $n(F)$  lets the dipole weighted by any power of the flux be the same as the number count dipole. For an exact power law, one therefore finds  $\Delta = 0$  and thus  $\Delta_W = 0$ . For magnitudes, such a power law corresponds to a linear relation between  $\log n(m)$  and  $m$ . As can be seen in Figure 5.1, for our model, their relation is in fact close to linear. This explains why weighting only by the magnitude does not give as large signal to noise ratios. This is the reason why we also include the redshifts of the sources.

We find that there is a flat maximum, where small changes in the parameters do not change the value of  $\Delta_W$  significantly. We use the exponents  $x_z = -3.3$  and  $x_m = 1.4$  where  $\Delta_W = 3.91$ .

For the SKA mock catalogs, we proceed very similarly. A weight function of the form  $W(L, F) = L^{x_L} F^{x_F}$  is chosen, with the length exponent  $x_L$  and the flux exponent  $x_F$  as free parameters. With this choice of a weight function, we find reasonable results for some combinations of  $x_L$  and  $x_F$  as can be seen in Figure 5.4. Again, the region for  $x_L = 0$  where  $\Delta_W$  is small is very noticeable. Similar to before, this is because the source density

per flux interval closely follows a power law, i.e. the relation between  $\log n(F)$  and  $\log F$  is close to linear, which can be seen in Figure 5.1.

Varying  $x_L$  and  $x_F$ , we find a maximum at around  $x_L = -1$  and  $x_F = 0.4$ . These are the exponents which we use in our analysis, for which  $\Delta_W = 2.84$ .

Let us also briefly explore the original idea of [15], which is weighting only by the flux. This might be of advantage if a large fraction of the sources are not resolved in their spatial extension, i.e. the lengths have a large uncertainty and cannot be used in the analysis. For the LSST/Euclid surveys, the case of weighting only by the magnitude is not as interesting since redshifts will be measured much more precisely than the sizes of small radio sources by the SKA.

For the SKA, setting  $x_L = 0$ , we find a flat maximum of  $\Delta_W \approx 0.4$  for  $x_F \approx -1$ . For  $x_F = 1$ , which corresponds to the dipole in sky brightness,  $\Delta_W < 0.1$  is even smaller. These values can possibly be optimized by also testing different flux cuts, which is not tested in this work. We compare the maximum possible  $\Delta_W = 2.84$  when the lengths are used with the maximum of  $\Delta_W = 0.4$  when no lengths are involved. The signal to noise ratio scales with  $\sqrt{N_{\text{tot}}}\Delta_W$ . Therefore, to achieve the same precision without using lengths, one would need  $(2.84/0.4)^2 \approx 50$  times the number of sources when analysing with the sources' lengths. In other words, as soon as more than a fraction  $1/50$  of the sources are resolved well enough, weighting by a combination of flux and length becomes a better choice than weighting by some power of the flux to measure  $\beta$ .

For the intrinsic dipole, the shot noise term (5.21) depends differently on  $\Delta_W$ . Hence, one finds that to measure  $\mathbf{d}_{\text{int}}$ , it is better to weight by only the inverse flux if thereby, 32 times as many sources are available.

In Section 5.8, we only show the results for including both lengths and fluxes. Nonetheless, the theory presented in Section 5.2 to Section 5.4 is also applicable to an analysis including only the flux. As a rule of thumb, any results from the SKA simulations for a number of  $N_{\text{tot}}$  sources presented in the following section also hold for the case when only the flux is considered and a number  $50 \times N_{\text{tot}}$  sources is available. For results concerning the intrinsic dipole, the factor is 34 instead of 50.

## 5.7 Caveats

Before analysing the results, we clearly state the approximations and assumptions that have been made in realizing the mock catalogs. We discuss why they are not significant for our main results presented in the next section.

In principle, all effects and relativistic corrections that give rise to fluctuations in the observed number density within the  $\Lambda$ CDM model are taken into account through the angular power spectrum [38]. However, some of these effects also perturb the redshift and the size of the sources. For example, the redshift space distortions are properly included in how they change the clustering of the sources but not in how they change the redshift that we observe. Similarly, angular perturbations are taken into account concerning the

realization of the source density through the angular power spectrum but not in the way how they affect the observed sizes.

Additionally, any correlations between the source properties and the source clustering are also not included. To illustrate this, let us consider the magnification bias and the peculiar velocities of the sources. There are some sources whose flux is increased to above the flux limit through Doppler effects due to their peculiar velocity, and they are only observed in the survey, i.e. above the lower flux limit, because of this. Therefore, the number density in this region is enhanced. Sources that are present in the survey because of such effects have special properties compared to other sources. In this case of increased clustering because of peculiar velocities, one could expect that the relative number of sources with a flux just above the lower flux limit is larger than in other regions. Any such correlations between source properties and the clustering are neglected in our mock catalogs.

Having stated this approximation, we continue to reason why it does not influence our results. First of all, perturbations on small angular scales are not relevant since we are interested in the dipole only. We therefore only show why large scale perturbations are expected to be small. To do so, we explicitly calculate one effect, the bulk flow velocity. The bulk flow velocity refers to the expected root mean square velocity of all observed sources. In other words, this is the deviation of the mean rest frame of the observed sources from the CMB rest frame as expected within the  $\Lambda$ CDM model. It is calculated in Appendix D, where we find for the LSST redshift distribution  $v_{\text{bulk}} \approx 2.4 \times 10^{-5}$ . This is approximately 2% of the CMB velocity. For the SKA, we find  $v_{\text{bulk}} \approx 2.0 \times 10^{-5}$ .

The effect of the bulk flow velocity is similar to the effects of our own motion. In particular, each source is not only affected by the Doppler effects and relativistic aberration due to our motion but also by the same effects due to the bulk flow, which points in some random direction. Therefore, the bulk flow leads to a systematic uncertainty of approximately 2% in comparing our velocity with the velocity inferred from the CMB dipole.

Other effects giving relativistic corrections are expected to be of the same order of magnitude or even smaller. For example gravitational potentials, which have similar effects on the observables as a relative velocity, are the source of peculiar velocities. Having constrained these velocities, the potentials are expected to be of the same order of magnitude. Also, lensing is small scale effect, as can be seen in Figure B.1. Therefore, a relevant correction from lensing is not expected for the dipole. Lastly, the redshift space distortions which contain a derivative term of the peculiar velocities are expected to be of the same order (see Section 2.2). Hence, neglecting all these perturbation when sampling the sources properties such as magnitude and redshift or flux and length is a reasonable approximation.

Another possible caveat should be discussed. When calculating the angular power spectrum, we do so for the full redshift range. Of course, in smaller redshift bins, the anisotropies are larger, especially for small  $z$  (see Figure 2.1). These larger clustering anisotropies become smaller when averaging over the full redshift range. Nevertheless, larger perturbations in smaller bins concern not only the clustering of the sources but also the sources' properties (magnitude, redshift, flux and length). Here, we make the reasonable assumption

that these effects become negligible when averaging over the full redshift range, such as the above mentioned bulk flow.

## 5.8 Results

In this section, the results of our new method using the weighted dipoles applied to the LSST/Euclid and SKA simulations are discussed and compared to the method employing only the number count dipole. We begin with the measurement of our velocity  $\beta$ .

### 5.8.1 Measuring our Velocity

The results of measuring our velocity can be seen for the LSST in Figure 5.5 and for the SKA in Figure 5.6. In the following, these two figures will be discussed in detail. They show the mean and standard deviation of the estimated velocities  $\beta$  and the deviation angles  $\theta$  in 100 mock catalog realizations. These values tell us about the bias and the uncertainty with which the velocity and its direction can be observed. Of course, the number count method does not estimate the velocity directly but rather the combined dipole that includes the intrinsic dipole. Nevertheless, to compare to the new weighing method, the number count dipole amplitudes are divided by  $B^N$  to give the best estimate for the velocity. The relative uncertainty in  $\beta$  and the number count dipole amplitude is the same.

To better understand the influence of shot noise, we show the results for a range of  $N_{\text{tot}}$ . Since each source is simulated individually, due to computational effort, we are limited to  $N_{\text{tot}} \approx 2 \times 10^7$ . Additionally, the results are shown when using the LSST sky coverage, the Euclid sky coverage but also when using the full sky. In any case,  $N_{\text{tot}}$  refers to the total number of sources in the observable region.

We also want to compare the results to the theory of the shot noise. Therefore, we show the mean and standard deviation of both  $\beta$  and  $\theta$  calculated with (2.57) and (2.58) in the case of the number count method. In the case of the new weighting method, we compare with (5.18) and (5.23). The theoretical results for the shot noise only hold for the full sky. As one can see in Figure 5.5 and Figure 5.6, the agreement between theory and simulations on the full sky is excellent. Therefore, we are confident to extrapolate the results obtained by the theory to larger number of sources.

Let us first discuss the full sky results before then focusing on the deviations because of partial sky coverage. For both LSST and SKA results, the trend is of course that the more sources are observed, the bias, the uncertainty and the deviation angle all decrease. The measurements of velocity amplitude and direction become more accurate and more precise. However, there is a crucial difference between the number count method and the new weighting method. This is best visible in the uncertainty of estimating the velocity  $\sigma_\beta$ . Clearly, for the number count method, the uncertainty converges to a constant, whereas for the weighting method, the uncertainty continues to decrease like  $1/\sqrt{N_{\text{tot}}}$ . This is also seen in the bias, i.e. for the number count method,  $\langle\beta\rangle$  does not converge exactly to the CMB velocity, which is the input of the simulations, as well as in the deviation angle, which becomes much closer to zero for the weighting method.

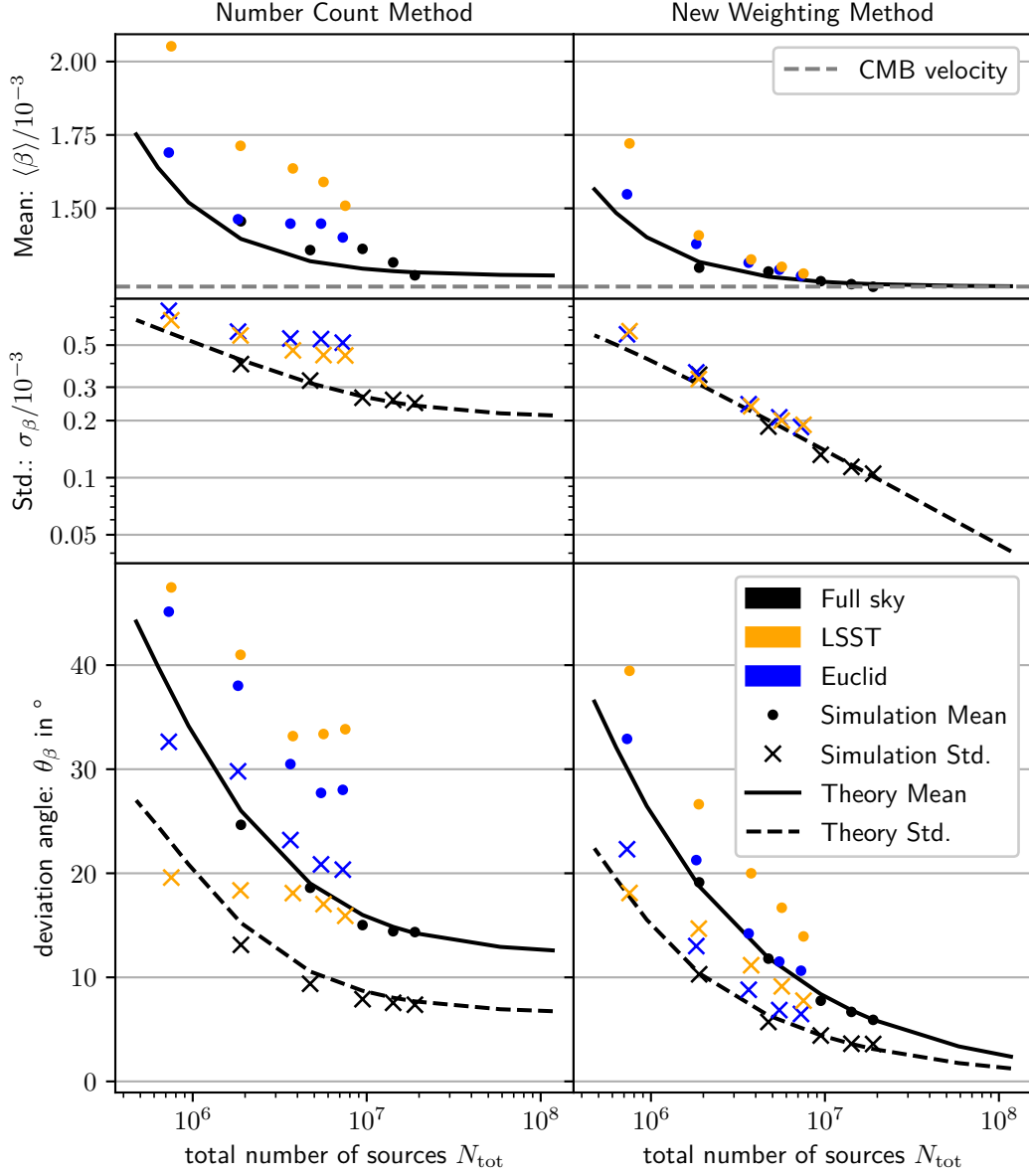


*Figure 5.5:* The results for estimating the velocity  $\beta$  (top and middle row) and the angle between the input velocity and the estimated direction, the deviation angle  $\theta$  (bottom row), for different total number of sources  $N_{\text{tot}}$ . The results from the number count method (left column, the velocity is the dipole divided by  $B^N$ ) are compared to the new weighting method (5.13) (right column). For each choice of  $N_{\text{tot}}$ ,  $\beta$  and  $\theta$  are estimated in 100 mock catalogs and the mean and standard deviation of these results are shown here as dots and crosses. The color indicates, with which sky coverage the analysis was performed. In addition, we show as solid and dashed lines the theoretical mean and standard deviation, respectively. They are calculated with (2.57), (2.58) and (5.18) and indicate the expectations for the behaviour of the full sky forecast. Note that these results assume perfect measurements of magnitude and redshift. A detailed discussion of the results is given in the main text.

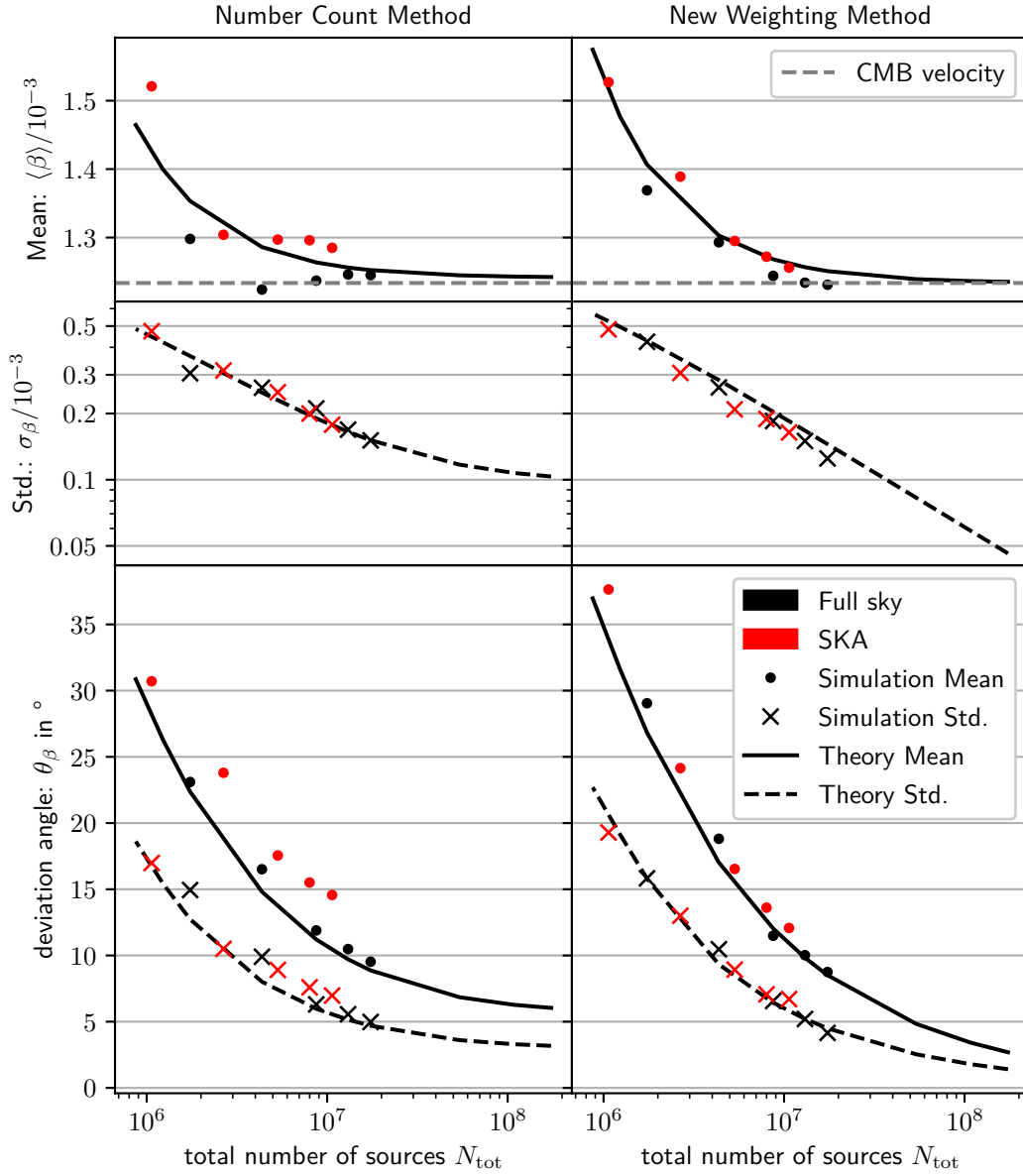


Figure 5.6: Similar to Figure 5.5, but for the SKA mock catalogs. Note that these results assume perfect measurements of flux and lengths. The inclusion of measurement errors is studied separately (see Figure 5.7).

The reason for this improvement is that the combined number count dipole has two random contributions. While the shot noise contribution indeed goes to zero for large  $N_{\text{tot}}$ , the intrinsic clustering dipole remains. Hence, even in the limit  $N_{\text{tot}} \rightarrow \infty$ , the number count dipole does not converge to the kinematic dipole, but has an unknown contribution from the random intrinsic dipole. Contrarily, the weighting method separates the intrinsic dipole from the kinematic effect and is thus only affected by shot noise, which can be arbitrarily small. This allows to measure our velocity amplitude and direction with a much higher precision, given enough sources. This difference between the two methods is smaller in the SKA forecast than in the LSST or Euclid forecasts because the intrinsic dipole is larger in the latter (see Figure 5.3). Therefore, for the SKA forecast, the uncertainty in the velocity inferred through the number count dipole converges to approximately  $10^{-4}$  instead of  $2 \times 10^{-4}$  for the LSST/Euclid full sky forecasts.

Continuing, we discuss why the results on the partial sky coverages deviate from the full sky results in different ways. As studied in Section 2.4, due to an incomplete sky coverage, there is a bias in the direction of the random dipoles as well as leakage from higher multipoles into the random dipole amplitudes. This is true for the shot noise and for the intrinsic clustering. The directional bias is the reason why the effect of an incomplete sky coverage is greater when analysing the deviation angle than when analysing the velocity.

Since we keep the total number of sources distributed on the observed region on the sky fixed, the number density is larger for a smaller sky coverage, which partly cancels the shot noise leakage (see Eq. (2.42)). The total leakage effect is thus dominated by the intrinsic clustering.

This explains why for the weighting method, the partial sky analyses (LSST, Euclid and SKA) all deviate less from the full sky analyses than for the number count method. The former is, as explained above, not at all affected by intrinsic clustering. Therefore, the new weighting method is not affected as much by the leakage effect. The directional bias through leakage is largest for the LSST mask, which covers only part of one hemisphere. Hence, the largest deviation from the full sky analysis of the new weighting method is seen in the LSST deviation angle (see bottom right of Figure 5.5). Since the SKA covers the largest fraction of the sky and because the intrinsic clustering is smallest in these simulations, the full sky analysis and the partial sky analysis of the SKA are very similar compared to the difference between full sky and Euclid or even LSST sky coverages.

The excellent agreement between theory and full sky results validate extrapolating the results to larger  $N_{\text{tot}}$  which are computationally expensive to simulate. For the cases of partial sky coverages that deviate significantly from the full sky case, we can nevertheless estimate how they behave for larger  $N_{\text{tot}}$  with Figures 5.5 and 5.6.

Next, we compare our analysis of the number count dipole in the SKA with the forecast [28]. Assuming  $N_{\text{tot}} = 3.3 \times 10^8$  above  $10\mu\text{Jy}$ , in their analysis, a relative uncertainty of the number count dipole amplitude of 12% is found. Similarly, we find an uncertainty of  $\sigma_\beta/\beta \approx 12\%$ . In [28], the galactic longitude and latitude can be determined with an uncertainty of  $13^\circ$  and  $6^\circ$ , respectively. Combining these, the mean deviation angle is

approximately  $10^\circ$ . Inspecting the trend of the mean deviation angles towards larger  $N_{\text{tot}}$  (see Figure 5.6, bottom left), this agrees well with our results for the SKA sky coverage.

Comparing these results to the weighting method, the same accuracy and precision can be achieved with approximately  $4 \times 10^7$  sources for which the length is perfectly measured. If the lengths of all the  $3.3 \times 10^8$  were available, we could measure  $\beta$  within approximately 2% and its direction within  $2^\circ$ . Similarly good results can be achieved if the redshift of the same number of sources was measured perfectly in the LSST or Euclid survey. We continue to show, that a small error ( $\sim 3\%$ ) does not degrade these results.

### 5.8.2 Effect of Measurement Uncertainty

Of course, the observations will not be perfect. Any measurement of the quantities magnitude, flux, redshift and length might deviate from their true value. To see how this affects estimating our velocity with the weighting method, we include such errors as described in Section 5.5. For simplicity, for the two applications, only a redshift uncertainty  $\sigma_z$  and an uncertainty in the length estimate  $\sigma_L$  are considered, respectively. In the LSST/Euclid (SKA) simulations, after including the kinematic effects, each redshift (length) is replaced by a random normal variable with mean of the original value and standard deviation  $\sigma_z$  ( $\sigma_L$ ). To avoid negative redshifts, we take the absolute value of the random redshift. It is important for the analysis that the telescope does not observe differently in any direction. Hence, we assume that neither the uncertainty nor the bias (which we take to be zero in general) is direction dependent.

We repeat the analysis including the measurement errors. The results can be seen in Figure 5.7. This time, we show mean and standard deviation of the velocity and the deviation angle as one errorbar. For comparison, also the outcome without any errors is shown.

In both the LSST/Euclid and SKA forecasts, small errors do not affect the results, while for a large enough error, the results become biased. This is because calculating the kinematic weighted dipole amplitude does not give correct results if the observed source density  $n(F, L)$  or  $n(m, z)$  differs significantly from the rest frame density due to measurement errors as discussed in Section 5.2.

For the LSST/Euclid forecasts, imposing an additional redshift cut of  $z > 0.2$  is tested. Since the error is proportional to  $(1 + z)$ , the relative error is largest for small redshifts. Therefore, this cut suppresses the bias. However, the scatter increases because less sources are available for the analysis. The SKA simulations already include a cut of  $L > 0.3$  arcsec. Applying a more stringent cut could also decrease the bias but greatly increase the shot noise, since there are many sources with  $L \sim 0.3$  arcsec (see Figure 5.1). If the behaviour of the observational uncertainties are well characterized, it might be possible to include these into the simulations and improve the analysis.

### 5.8.3 Measuring the Intrinsic Dipole

We also test how well the intrinsic dipole can be measured using the estimator (5.14). To do so, we compare the estimated intrinsic dipole with the true one. The true intrinsic

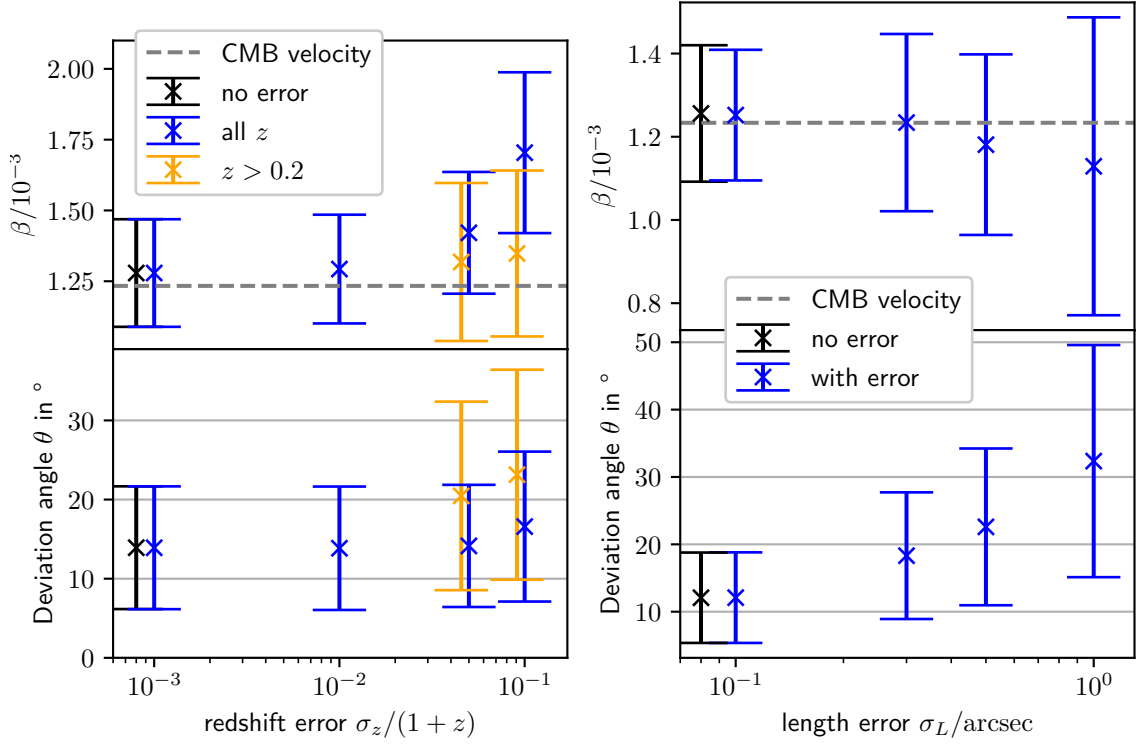


*Figure 5.7:* The effect of a simulated observational uncertainty on the accuracy and precision of the velocity estimator (5.13). The error bars show the mean and standard deviation of the velocity  $\beta$  and deviation angle  $\theta$  estimated in 100 mock catalogs. For comparison, the case without any error is also shown as a black error bar. This corresponds to the results for the largest  $N_{\text{tot}}$  shown in Figures 5.5 and 5.6, respectively. *Left:* LSST simulations: a redshift error  $\sigma_z = (10^{-3} \sim 10^{-1})(1+z)$  has been imposed on the mock catalogs, as described in the main text. The blue error bars show the results when including all sources. The orange error bars show the results when only using sources with redshift larger than 0.2 for the analysis. *Right:* SKA simulations: an error in the length  $\sigma_L$  has been included.

dipole is different for each mock catalog, as each is a random realization of the angular power spectrum. By comparing the amplitude and direction of the estimated values with the true values of the respective mock catalog, we can test the uncertainty by the standard deviation. The results for both LSST/Euclid and SKA simulations are shown in Figure 5.8.

We begin with discussing the full sky simulations. First, we notice that they agree well with the theory (5.21), (5.22) and (5.23). Comparing to the velocity estimates discussed above, the intrinsic dipole estimates are more biased and less precise. This is because the shot noise in the intrinsic dipole  $C_{\text{int}}^{\text{SN}}$  is larger than the shot noise in the velocity  $C_{\beta}^{\text{SN}}$  (compare (5.17) with (5.21)). Even so, given a large number of sources and a large enough sky coverage, it is possible to detect the intrinsic dipole to a high precision.

We turn our focus to the effect of incomplete sky coverage. In the LSST/Euclid forecast, the estimation of the dipole amplitude and direction is limited by the leakage from higher intrinsic multipoles to the intrinsic dipole due to the incomplete sky coverage as discussed

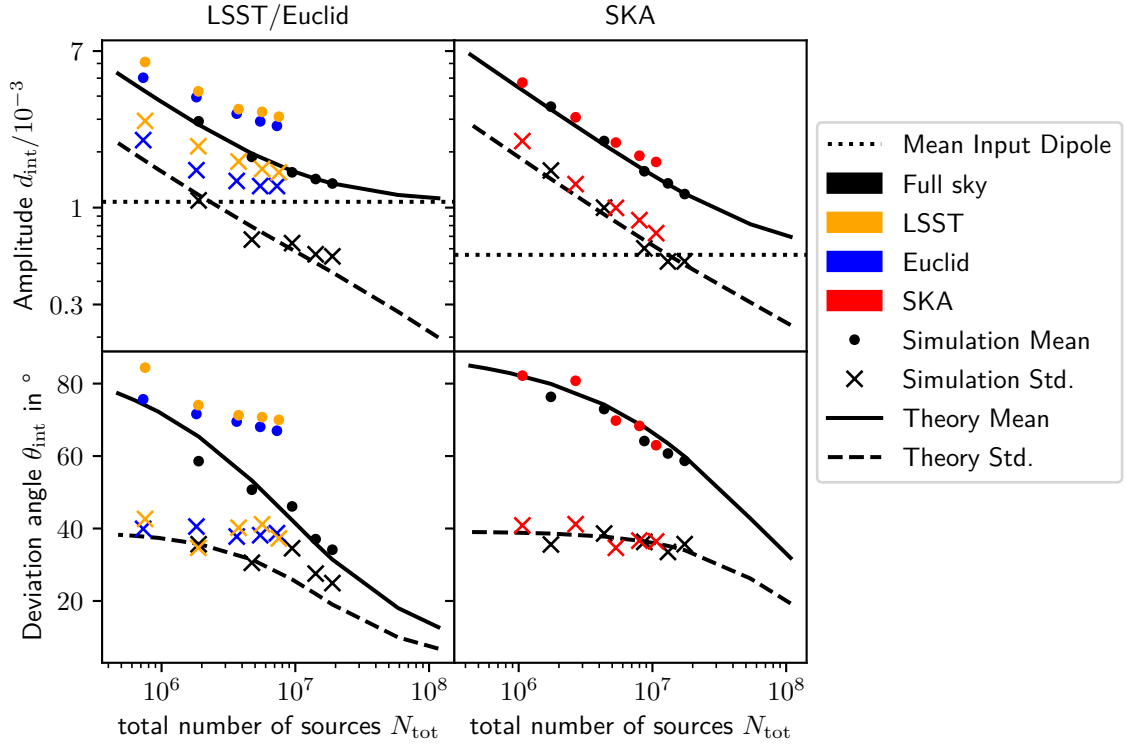


Figure 5.8: The results of estimating the amplitude and direction of the intrinsic dipole with the weighting method (5.14). The top panels show the mean and standard deviation of estimating the intrinsic dipole amplitude. The bottom panels show the deviation angle  $\theta_{\text{int}}$ , which indicates how well the direction of the intrinsic dipole amplitude can be inferred.

in Section 2.4. From (2.44), we expect that the leakage enhances the intrinsic dipole by approximately a factor of  $\gtrsim f_{\text{sky}}^{-1/2}$ , which in this case is  $\gtrsim \sqrt{2.5}$ . This explains why the estimated amplitudes are biased by approximately a factor of 2 and the estimated directions differ by more than  $60^\circ$ .

For the SKA forecast, the results on the masked sky are nearly equally good as the full sky results, because the sky coverage of the SKA survey is much larger. However, this is only tested up to  $10^7$  sources, where the shot noise dipole still dominates over the leakage into the intrinsic dipole. Therefore, in comparison to the LSST/Euclid results, where the clustering and thus the leakage is larger, for the SKA, we do not see a divergence from the full sky in the simulations. With these results only, it is thus difficult to say how well the intrinsic dipole itself can be determined. To make such a statement, the simulations should be repeated with a larger number of sources.

Obtaining an estimate of the intrinsic dipole with a small sky coverage is possibly a too ambitious endeavor. Instead of comparing the estimated intrinsic dipole to the true intrinsic dipole, one could compare it to the expected value of intrinsic dipole plus the leakage from higher multipoles. The leakage can be estimated by realizing fields from the angular power spectrum, masking them, and then estimating the dipole. Even though the leakage is not deterministic, one could possibly constrain the isotropy better this way.

---

The influence of measurement errors is not studied. However, similar effects as discussed for the velocity estimator are expected for estimating the intrinsic dipole.

To summarize, we have shown that the intrinsic dipole can indeed be measured independently of our velocity. Nevertheless, incomplete sky coverage and hence leakage from higher clustering multipoles strongly biases this observation.

## 6 Conclusions

In the following, the main results of this work are summarized. The relevant theory of observing the cosmic matter dipole as the number count dipole was discussed. We introduced its three contributions, through kinematic effects, intrinsic clustering and shot noise. The statistics of how these three contributions, the first of them being fixed in direction, the latter two pointing in random directions, combine to one dipole were studied in detail. Thereby, we were able to quantify the consequences of the assumptions stated in the introduction and turn them into a prediction of the cosmic matter dipole in the  $\Lambda$ CDM model. These assumptions are the interpretation of the CMB dipole as a purely kinematic effect and isotropy by the cosmological principle.

While from the former follows a straightforward prediction of the kinematic dipole amplitude and direction, quantifying the consequences of the latter is more involved. Deviations in the matter distribution on the largest scale are indeed expected to be small, if the observed sources are distant. However, the distances to the sources are often not well known.

By analysing the dipoles in the distribution of NVSS radio sources and in a sample of Quasars from the CatWISE 2020 data, we found that a large systematic uncertainty arises through the ignorance of the sources' redshift distribution. In particular, a small percentage of nearby sources ( $z < 0.1$ ) can lead to a large intrinsic dipole. Depending on the amount of local structure observed in the NVSS, the large amplitude of the NVSS dipole is found to be in agreement or slight disagreement with the  $\Lambda$ CDM model at  $1.1\sigma$  to  $2.2\sigma$ . The disagreement is confirmed since the same excess in the amplitude is also found in other radio surveys (see Section 1.3). Concerning the quasar sample, by including a realistic clustering in the analysis, we found that the large amplitude of the dipole in the distribution of quasars is inconsistent with the  $\Lambda$ CDM model at  $2.8\sigma$ , but not at  $4.9\sigma$  which is claimed in the original publication [27] where clustering is neglected.

With that, we come back to the two questions posed in the introduction. Is there a matter anisotropy on the largest scale, unknown to the  $\Lambda$ CDM model? Is the CMB dipole truly a purely kinematic effect and any intrinsic CMB dipole is negligible? Both dipole analyses could be explained with either of the two deviations from the  $\Lambda$ CDM model.

Future large scale surveys, observing  $\sim 100$  times more sources than currently available might find that the large dipole amplitudes were observed by chance or due to unknown systematic effects. They might, however, also show with a much higher accuracy that the cosmic matter dipole does not agree with the  $\Lambda$ CDM model expectations.

If so, one would like to know which of the two assumptions, isotropy or the purely kinematic interpretation of the CMB dipole, is violated.

The method presented in the final Chapter 5 can be decisive in that matter. By incorporating other observed properties of galaxies, we are able to measure the velocity and the intrinsic dipole separately. We have shown the potential of this method in forecasts for the LSST and the Euclid survey, including redshift measurements, and the SKA survey, including the sources' sizes. Since in this method, the intrinsic dipole is distinguished from the kinematic dipole, our velocity and direction of motion can be determined to a much higher precision, given enough sources with a small uncertainty in the observed redshifts and sizes. Also, we showed that with this method, the intrinsic dipole amplitude can be constrained independently if additionally a large fraction of the sky is observed. This new method thus has the potential to allow for a more precise test of the fundamental assumptions in the standard model of cosmology.

# A Spherical Harmonics

We briefly present some important concepts and formulas concerning the expansion of a field in spherical harmonics  $Y_{lm}$  and the angular power spectrum denoted by the multipoles  $C_l$  (see for example [42], Appendix 4.2 or [64] and references therein).

## A.1 Basics

The spherical harmonic coefficients  $a_{lm}$  of a field  $f(\hat{\mathbf{n}})$  defined on the sphere are

$$a_{lm} = \int d\Omega Y_{lm}^*(\hat{\mathbf{n}}) f(\hat{\mathbf{n}}). \quad (\text{A.1})$$

The reverse transformation is

$$f(\hat{\mathbf{n}}) = \sum_{l=0}^{\infty} \sum_{m=-l}^l a_{lm} Y_{lm}(\hat{\mathbf{n}}). \quad (\text{A.2})$$

Here,  $\hat{\mathbf{n}}$  denotes both spherical coordinates  $\theta$  and  $\phi$  and  $\int d\Omega = \int_0^{2\pi} d\phi \int_0^\pi d\theta \sin\theta$ .

A few identities used in this work are the orthonormality of the spherical harmonics

$$\int d\Omega Y_{lm}(\hat{\mathbf{n}}) Y_{l'm'}^*(\hat{\mathbf{n}}) = \delta_{m,m'} \delta_{l,l'}, \quad (\text{A.3})$$

their mean value

$$\int d\Omega Y_{lm}(\hat{\mathbf{n}}_i) = \begin{cases} \sqrt{4\pi} & , l = 0 \\ 0 & , l > 0. \end{cases}, \quad (\text{A.4})$$

and the expansion of the exponential using spherical Bessel functions of the first kind  $j_l$

$$\exp(i\mathbf{k} \cdot \mathbf{r}) = 4\pi \sum_{l=0}^{\infty} \sum_{m=-l}^l i^l j_l(kr) Y_{lm}^*(\hat{\mathbf{n}}) Y_{lm}(\hat{\mathbf{k}}). \quad (\text{A.5})$$

For a real field  $f(\hat{\mathbf{n}}) = f^*(\hat{\mathbf{n}})$  (the star denotes complex conjugation)

$$a_{lm}^* = (-1)^m a_{l-m}. \quad (\text{A.6})$$

The angular power spectrum, i.e the multipoles  $C_l$  are defined to be the variance of the  $a_{lm}$

$$C_l = \langle |a_{lm}|^2 \rangle. \quad (\text{A.7})$$

With the ensemble average  $\langle \dots \rangle$ , one refers to the average over many realizations of  $a_{lm}$  from the  $C_l$ . Of course, we are only able to observe one universe, so we cannot measure  $C_l$  directly. Instead, we can observe only one realization of the  $a_{lm}$ . From this, the angular power spectrum is estimated as

$$C_l = \frac{1}{2l+1} \sum_{m=-l}^l |a_{lm}|^2. \quad (\text{A.8})$$

To estimate a  $C_l$ , one can measure  $(2l+1)$  independent numbers through the  $a_{lm}$ . Therefore, the uncertainty becomes larger for small  $l$ .

## A.2 Realizing Fluctuations from the Angular Power Spectrum

In reverse, from an angular power spectrum, one can realize a random real field with the expected amount of fluctuations. In this work, we always assume Gaussian fluctuations. For the intrinsic clustering on large scales this is a good approximation because nonlinearities are small on these scales (compare to Figure B.1). Also, for the shot noise, the Poissonian distribution is well approximated by a Gaussian distribution through the central limit theorem since we are interested in the distribution of many sources.

To realize a field, one draws random normal variables for the real and imaginary part of  $a_{lm}$  with zero mean and variance  $C_l/2$  for  $m > 0$  and one variable for the real  $a_{l0}$  with zero mean and variance  $C_l$ . The coefficients for  $m < 0$  follow from (A.6). The mean has to be zero because of the assumption of isotropy. Through the choice of the variance, the definition, (A.7), is satisfied. From the random spherical harmonic coefficients, one can compute the density fluctuations by (A.2). In particular, a field of relative fluctuations  $\Delta(\hat{\mathbf{n}})$  is obtained by using only  $a_{lm}$  with  $l \geq 1$  drawn from the angular power spectrum with the convention that the angular power spectrum is normalized to  $C_0 = 4\pi$ .

With that, one can compute a field with fluctuations around the mean number density  $\bar{N}$ . On a pixelised sphere, this corresponds to setting the value for each pixel  $p$  to

$$m_p = (1 + \Delta(\hat{\mathbf{n}}_p))\bar{N}. \quad (\text{A.9})$$

To do so, we use healpy (a Python package based on HEALPix<sup>1</sup>) [47, 48], which provides a pixelisation scheme on the sphere, where each pixel has the same area. To include shot noise, we simply replace each pixel value by a Poissonian random variable with its mean being the original pixel value

$$m_p \rightarrow \mathcal{P}(m_p). \quad (\text{A.10})$$

---

<sup>1</sup><http://healpix.sf.net/>

Simulating only shot noise corresponds to setting  $\Delta(\hat{\mathbf{n}}) = 0$  in (A.9).

### A.3 Relation with the Dipole

Lastly, we want to discuss the relation between the dipole, the spherical harmonic coefficients and the first multipole, the dipole power  $C_1$ . Consider the field containing a dipole

$$(1 + \mathbf{d} \cdot \hat{\mathbf{n}})\bar{N} + \mathcal{O}(n_j^2) = \bar{N}(a_{00}Y_{00}(\hat{\mathbf{n}}) + a_{10}Y_{10}(\hat{\mathbf{n}}) + a_{11}Y_{11}(\hat{\mathbf{n}}) + a_{1-1}Y_{1-1}(\hat{\mathbf{n}}) + \mathcal{O}(l > 1)). \quad (\text{A.11})$$

We use the convention that the  $a_{lm}$  are relative fluctuations and do not include the monopole. By explicitly writing

$$\begin{aligned} \hat{\mathbf{n}} &= (\sin \theta \cos \phi, \sin \theta \sin \phi, \cos \theta), & Y_{00} &= 1/\sqrt{4\pi}, \\ Y_{10}(\hat{\mathbf{n}}) &= \sqrt{\frac{3}{4\pi}} \cos \theta, & Y_{1-1}(\hat{\mathbf{n}}) &= \sqrt{\frac{3}{8\pi}} \sin \theta e^{-i\phi}, & Y_{11}(\hat{\mathbf{n}}) &= -Y_{1-1}^*(\hat{\mathbf{n}}), \end{aligned}$$

we find

$$a_{00} = \sqrt{4\pi}, \quad d_x = -i(a_{1-1} + a_{11})\sqrt{\frac{3}{8\pi}}, \quad (\text{A.12})$$

$$d_y = (a_{1-1} - a_{11})\sqrt{\frac{3}{8\pi}}, \quad d_z = a_{10}\sqrt{\frac{3}{4\pi}}. \quad (\text{A.13})$$

Measuring a dipole with amplitude  $d = \sqrt{d_x^2 + d_y^2 + d_z^2}$ , by (A.8), we can conclude about the dipole power

$$C_1 = \frac{4\pi d^2}{9}. \quad (\text{A.14})$$

Concerning a random realization of an angular power spectrum, using (A.7), the squared dipole amplitude is related to the dipole power by

$$\langle d^2 \rangle = \langle d_x^2 + d_y^2 + d_z^2 \rangle = \frac{9C_1}{4\pi}. \quad (\text{A.15})$$

Invoking isotropy, for the individual dipole components follows

$$\langle d_{x,y,z} \rangle = 0, \quad \langle d_{x,y,z}^2 \rangle = \frac{3C_1}{4\pi}, \quad (\text{A.16})$$

respectively. Since the  $a_{lm}$  are independent and well approximated by a Gaussian distribution, the dipole components are, too. Therefore, the dipole amplitude found in a random field realized from the angular power spectrum is also random and follows a  $\chi(3)$ -distribution (also Maxwell-Boltzmann distribution)

$$P(d) = \frac{d^2}{\sigma^3} \exp\left(\frac{-d^2}{2\sigma^2}\right) \sqrt{\frac{2}{\pi}}, \quad (\text{A.17})$$

where we introduced  $\sigma = 3C_1/(4\pi)$ . (A.17) can be derived by performing a variable transformation on the product of three normal distributions  $P(\mathbf{d}) = P(d_x)P(d_y)P(d_z)$

$$P(\mathbf{d})d\mathbf{d} = P(\mathbf{d})4\pi d^2 dd \equiv P(d)dd. \quad (\text{A.18})$$

## B Contributions to the Angular Power Spectrum

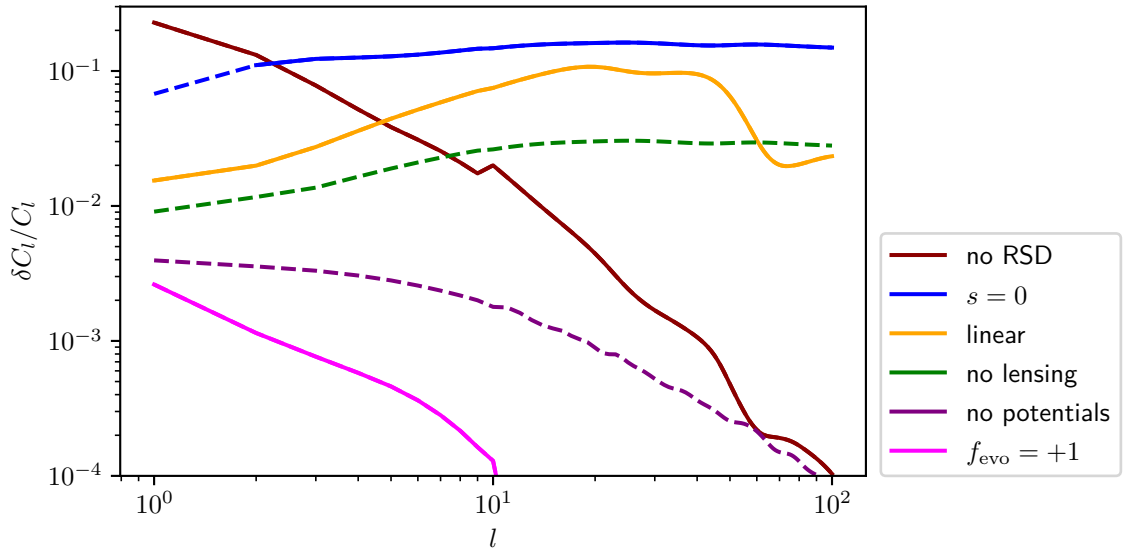


*Figure B.1:* In order to estimate the contributions to the full angular power spectrum  $C_l$ , we show the relative difference  $\delta C_l / C_l = |C_l^{\text{mod}} - C_l| / C_l$ , when modifying one input parameter of the calculation to get  $C_l^{\text{mod}}$ . Dashed lines are used when  $C_l^{\text{mod}} - C_l > 0$  and straight lines are used when  $C_l^{\text{mod}} - C_l < 0$ . This means that for example RSD give a positive contribution to the angular power spectrum. The fiducial angular power spectrum  $C_l$  used here is the one expected for the NVSS with the T-RECS model for the redshift distribution, with  $s = 0.85/2.5$  and  $f_{\text{evo}} = 0$ . It is displayed in the right panel of Figure 3.5. A detailed discussion about the various effects and contributions is found in this appendix.

We discuss the various effects on the angular power spectrum (see Figure B.1). One can see that for the largest scales (smallest  $l$ ), redshift space distortions (RSD) are the most important contribution with about 20% of the full angular power spectrum including all effects. Neglecting the influence of gravitational potentials influences the multipoles only below 1%. Lensing is a small effect similar on all scales, when setting the magnification bias to 0.85/2.5 which is the expected value for the NVSS angular power spectrum. This is because lensing terms mostly appear in the combination  $(2 - 5s)$ . In other words, if the cumulative number density above a minimum flux  $F$  is precisely in the form of

---

$N(> F) \propto F^{-1}$ , then the magnification bias is  $1/2.5$  and these terms cancel exactly. To illustrate this, we also show the calculation of the power spectrum setting  $s = 0$ . Then, lensing is much more relevant, especially on small scales. The evolution bias  $f_{\text{evo}}$  characterizes the change of the source density with time (see (2.15)). We approximate it to be 0 in the calculation for the NVSS power spectrum. The deviation in the angular power spectrum using  $f_{\text{evo}} = 1$  is small. Since the evolution bias is typically of order 1 (compare e.g. to Fig. 2 in [39]), we conclude that setting  $f_{\text{evo}} = 0$  is a good approximation. Finally, we compare the full angular power spectrum which is computed with the halofit model to include non-linearities with the results using the linear power spectrum. On large scales, this affects the result only the percent level.

## C Multipole Estimator

We use the method to estimate the angular power spectrum described in [56], where the method is described in detail. In this Appendix, we only briefly discuss the method and test it.

The goal is to estimate the multipoles of the field  $f(\hat{\mathbf{n}})$ , which for our applications is typically a number density. The complication arises, because only a fraction  $f_{\text{sky}}$  of the sky is observed. We introduce the window function  $W(\hat{\mathbf{n}})$ , which is either one, if the region of the sky is observed, and zero, if it is masked. Only the field  $\tilde{f}(\hat{\mathbf{n}}) = W(\hat{\mathbf{n}})f(\hat{\mathbf{n}})$  is available for the analysis. We analyse the field on a pixelised sphere using the methods provided by healpy. First, we fit the monopole  $m$  to the field

$$m = \sum_p \frac{\tilde{f}(\hat{\mathbf{n}}_p)}{f_{\text{sky}} N_{\text{pix}}}, \quad (\text{C.1})$$

where the sum runs over all pixels  $p$  and remove it by subtracting  $m$  from each pixel value  $\tilde{f}(\hat{\mathbf{n}}_p)$ . Next, the pseudo power spectrum  $\tilde{C}_l$  is calculated which is defined as

$$\tilde{C}_l = \frac{1}{2l+1} \sum_{m=-l}^l |\tilde{a}_{lm}|^2 \quad (\text{C.2})$$

$$\tilde{a}_{lm} = \frac{1}{m} \int d\Omega \tilde{f}(\hat{\mathbf{n}}) Y_{lm}^*(\hat{\mathbf{n}}) \approx \frac{4\pi}{N_{\text{pix}} m} \sum_p \tilde{f}(\hat{\mathbf{n}}) Y_{lm}^*(\hat{\mathbf{n}}) \quad (\text{C.3})$$

with the healpy-method `anafast`. As it is shown in [56], the expected values of the pseudo power spectrum can be related to the true power spectrum by

$$\langle \tilde{C}_l \rangle = \sum_{l'} R_{ll'} \langle C_{l'} \rangle. \quad (\text{C.4})$$

This means that averaging over many realizations of  $C_l$ , the mixing matrix  $R_{ll'}$  correctly describes the effect of the partial sky coverage, which leads to the mean pseudo power spectrum. For one realization, however, this is not quite true. Nevertheless, it serves as a good estimator for our purpose. The mixing matrix can be derived by inserting the relation between the pseudo and the true spherical harmonic coefficients

$$\tilde{a}_{lm} = \int d\Omega W(\hat{\mathbf{n}}) f(\hat{\mathbf{n}}) Y_{lm}^*(\hat{\mathbf{n}}) = \sum_{l'm'} a_{l'm'} \int d\Omega W(\hat{\mathbf{n}}) Y_{l'm'}(\hat{\mathbf{n}}) Y_{lm}^*(\hat{\mathbf{n}}) \quad (\text{C.5})$$

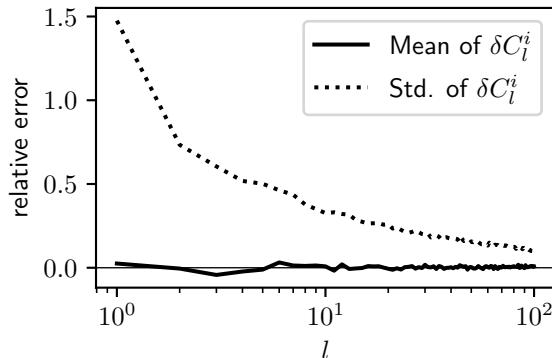


Figure C.1: The mean and standard deviation of the relative error  $\delta C_l^i$  as defined in the main text of 500 simulations. While the estimator is unbiased (vanishing mean), the uncertainty can become as large as 75% for small  $l > 1$ .

into equation (C.2). All the steps are found in the Appendix A.2 of [56]. The result expressed in terms of the power spectrum of the window function ( $\mathcal{W}_l = 1/(2l+1) \sum_m |w_{lm}|^2$ ,  $w_{lm} = \int d\Omega W(\hat{\mathbf{n}}) Y_{lm}^*(\hat{\mathbf{n}})$ ) and the Wigner symbols is

$$R_{l_1 l_2} = \frac{2l_2 + 1}{4\pi} \sum_{l_3} (2l_3 + 1) \mathcal{W}_{l_3} \begin{pmatrix} l_1 & l_2 & l_3 \\ 0 & 0 & 0 \end{pmatrix}. \quad (\text{C.6})$$

Inverting equation (C.4), we obtain our estimator for the angular power spectrum of a masked sky.

$$C_l^{\text{est}} = \sum_{l'} R_{ll'}^{-1} \tilde{C}_{l'}. \quad (\text{C.7})$$

We test the estimator to function properly by computing 100 realizations of a density field with

$$C_l^{\text{true}} = 10^{-5} / \sqrt{l}. \quad (\text{C.8})$$

for  $l \geq 0$  and  $C_0^{\text{true}} = 4\pi$ . We use Mask 2 from the NVSS analysis to cover 35% of the sky, see Figure 3.4. To test the estimator, we define the relative error between the estimated angular power spectrum and the true one of the  $i$ th realization

$$\delta C_l^i \equiv (C_l^{\text{est},i} - C_l^{\text{true},i}) / C_l^{\text{true},i}. \quad (\text{C.9})$$

The average relative error of all the simulations should be zero, such that the estimator is unbiased. The standard deviation, i.e. the scatter in the relative error shows how large the error typically is. The result is shown in Figure C.1. The mean of  $\delta C_l^i$  is smaller than 5% for all  $l$  and averaged over  $l$  only 0.3%, so the estimator is unbiased. Each individual realization however can be estimated differently by up to 75% for small multipoles with  $l > 1$ . In previous studies, the matrix  $R_{ll'}^{-1}$  is approximated to be diagonal [40, 57, 65]. This is a good approximation for higher multipoles [65]. Since we are interested in small multipoles, where the window function can mix the multipole coefficient significantly, we use the full matrix.

## D Bulk Flow Velocity

The bulk flow velocity is the expected root mean square velocity of all observed sources. If the sources are distributed accordingly to the normalized redshift distribution  $n(z)$ , one can define the window function

$$W(\mathbf{r}) = H(z(r)) \frac{n(z(r))}{4\pi r^2}, \quad (\text{D.1})$$

such that  $\int dx^3 W(\mathbf{r}) = \int dz n(z) = 1$ .

The bulk flow of all the observed sources is expected to be (in units of the speed of light)

$$\begin{aligned} \langle \mathbf{v}_{\text{flow}}^2 \rangle &= \left\langle \left( \int d^3x W(\mathbf{r}) \mathbf{v}(\mathbf{r}) \right)^2 \right\rangle = \\ &= \frac{1}{2\pi^2} \int dk P_{\delta\delta}(k) \left( \int dz H(z) f(z) D_+(z) n(z) \frac{\sin(kr(z))}{kr(z)} \right)^2. \end{aligned} \quad (\text{D.2})$$

We take the power spectrum  $P_{\delta\delta}$  (in synchronous gauge) at zero redshift from CLASS. The difference between using the non-linear or linear power spectrum is negligible because only the largest scale is relevant. We use that the velocity has no curl,  $\mathbf{v} = \hat{\mathbf{k}}V$ , and  $\mathbf{v} \cdot \mathbf{k} = -f(z)H(z)D_+(z)\delta(0)$  [66] with  $f(z) \approx \Omega_m^{4/7}(z)$  and the growth function defined by  $f = \frac{d \ln D_+}{d \ln a}$  [67]. For the redshift distributions of the two applications (see Figure 5.3), we find

$$\text{LSST/Euclid:} \quad \langle \mathbf{v}_{\text{flow}}^2 \rangle = (2.4 \times 10^{-5})^2 \quad (\text{D.3})$$

$$\text{SKA:} \quad \langle \mathbf{v}_{\text{flow}}^2 \rangle = (2.0 \times 10^{-5})^2 \quad (\text{D.4})$$

In our universe, we expect a random velocity  $v$  from a  $\chi(3)$ -distribution with  $\langle v^2 \rangle = \langle \mathbf{v}_{\text{flow}}^2 \rangle$ , pointing in a random direction. This means that the mean rest frame of all observed sources and the rest frame defined by the CMB differ by  $v$ .

# List of Acronyms

**$\Lambda$ CDM**  $\Lambda$  (dark energy) Cold Dark Matter (the standard model of cosmology)

**AGN** Active Galactic Nucleus

**CatWISE** Catalog of sources from WISE and NEOWISE survey data

**CMB** Cosmic Microwave Background

**LSS** Large Scale Structure

**LSST** Legacy Survey of Space and Time

**NRAO** Northern Radio Astronomy Observatory

**NVSS** NRAO VLA Sky Survey

**PDF** Probability Density Function

**RSD** Redshift Space Distortions

**SFG** Star-Forming Galaxy

**SKA** Square Kilometre Array

**Std.** Standard deviation

**VLA** Very Large Array

**w.r.t.** with respect to

# Bibliography

- [1] E. A. Milne (1937). “Kinematics, dynamics, and the scale of time”. *Proceedings of the Royal Society of London. Series A - Mathematical and Physical Sciences* 158 (894): pp. 324–348.
- [2] J. A. Peacock (1998). *Cosmological Physics*. Cambridge University Press.
- [3] M. I. Scrimgeour, T. Davis, C. Blake, J. B. James, G. B. Poole, L. Staveley-Smith, S. Brough, M. Colless, C. Contreras, W. Couch, S. Croom, D. Croton, M. J. Drinkwater, K. Forster, D. Gilbank, M. Gladders, K. Glazebrook, B. Jelliffe, R. J. Jurek, et al. (Sept. 2012). “The WiggleZ Dark Energy Survey: the transition to large-scale cosmic homogeneity”. *Monthly Notices of the Royal Astronomical Society* 425 (1): pp. 116–134.
- [4] R. B. Tully, H. Courtois, Y. Hoffman, and D. Pomarède (Sept. 2014). “The Laniakea supercluster of galaxies”. *Nature* 513 (7516): pp. 71–73.
- [5] D. W. Hogg, D. J. Eisenstein, M. R. Blanton, N. A. Bahcall, J. Brinkmann, J. E. Gunn, and D. P. Schneider (May 2005). “Cosmic Homogeneity Demonstrated with Luminous Red Galaxies”. *The Astrophysical Journal* 624 (1): 54–58.
- [6] C. H. Lineweaver, L. Tenorio, G. F. Smoot, P. Keegstra, A. J. Banday, and P. Lubin (Oct. 1996). “The Dipole Observed in the COBE DMR 4 Year Data”. *Astrophysical Journal* 470: p. 38.
- [7] Planck Collaboration, Aghanim, N., Akrami, Y., Arroja, F., Ashdown, M., Aumont, J., Baccigalupi, C., Ballardini, M., Banday, A. J., Barreiro, R. B., Bartolo, N., Basak, S., Battye, R., Benabed, K., Bernard, J.-P., Bersanelli, M., Bielewicz, P., Bock, J. J., Bond, J. R., et al. (2020). “Planck 2018 results - I. Overview and the cosmological legacy of Planck”. *Astronomy and Astrophysics* 641: A1.
- [8] P. J. E. Peebles and D. T. Wilkinson (Oct. 1968). “Comment on the Anisotropy of the Primeval Fireball”. *Phys. Rev.* 174 (5): pp. 2168–2168.
- [9] Planck Collaboration, Aghanim, N., Armitage-Caplan, C., Arnaud, M., Ashdown, M., Atrio-Barandela, F., Aumont, J., Baccigalupi, C., Banday, A. J., Barreiro, R. B., Bartlett, J. G., Benabed, K., Benoit-Lévy, A., Bernard, J.-P., Bersanelli, M., Bielewicz, P., Bobin, J., Bock, J. J., Bond, J. R., et al. (2014). “Planck 2013 results. XXVII. Doppler boosting of the CMB: Eppur si muove”. *Astronomy and Astrophysics* 571: A27.
- [10] C. Blake and J. Wall (Mar. 2002). “A velocity dipole in the distribution of radio galaxies”. *Nature* 416 (6877): 150–152.

- [11] J. J. Condon, W. D. Cotton, E. W. Greisen, Q. F. Yin, R. A. Perley, G. B. Taylor, and J. J. Broderick (May 1998). “The NRAO VLA Sky Survey”. *The Astronomical Journal* 115 (5): pp. 1693–1716.
- [12] A. K. Singal (Nov. 2011). “Large peculiar motion of the solar system from the dipole anisotropy in sky brightness due to distant radio sources”. *The Astrophysical Journal* 742 (2): p. L23.
- [13] C. Gibelyou and D. Huterer (Nov. 2012). “Dipoles in the sky”. *Monthly Notices of the Royal Astronomical Society* 427 (3): 1994–2021.
- [14] M. Rubart and D. J. Schwarz (2013). “Cosmic radio dipole from NVSS and WENSS”. *Astronomy and Astrophysics* 555: A117.
- [15] P. Tiwari, R. Kothari, A. Naskar, S. Nadkarni-Ghosh, and P. Jain (Feb. 2015). “Dipole anisotropy in sky brightness and source count distribution in radio NVSS data”. *Astroparticle Physics* 61: 1–11.
- [16] P. Tiwari and P. Jain (Jan. 2015). “Dipole anisotropy in integrated linearly polarized flux density in NVSS data”. *Monthly Notices of the Royal Astronomical Society* 447 (3): pp. 2658–2670.
- [17] J. Colin, R. Mohayaee, M. Rameez, and S. Sarkar (June 2017). “High-redshift radio galaxies and divergence from the CMB dipole”. *Monthly Notices of the Royal Astronomical Society* 471 (1): 1045–1055.
- [18] P. Tiwari and A. Nusser (Mar. 2016). “Revisiting the NVSS number count dipole”. *Journal of Cosmology and Astroparticle Physics* 2016 (03): 062–062.
- [19] C. Bengaly, R. Maartens, and M. Santos (2018). “Probing the Cosmological Principle in the counts of radio galaxies at different frequencies”. *Journal of Cosmology and Astroparticle Physics* 04: p. 031.
- [20] T. M. Siewert, M. Schmidt-Rubart, and D. J. Schwarz (2020). “The Cosmic Radio Dipole: Estimators and Frequency Dependence”. *arXiv preprint 2010.08366*.
- [21] M. F. Skrutskie, R. M. Cutri, R. Stiening, M. D. Weinberg, S. Schneider, J. M. Carpenter, C. Beichman, R. Capps, T. Chester, J. Elias, J. Huchra, J. Liebert, C. Lonsdale, D. G. Monet, S. Price, P. Seitzer, T. Jarrett, J. D. Kirkpatrick, J. E. Gizis, et al. (Feb. 2006). “The Two Micron All Sky Survey (2MASS)”. *The Astronomical Journal* 131 (2): pp. 1163–1183.
- [22] J. P. Huchra, L. M. Macri, K. L. Masters, T. H. Jarrett, P. Berlind, M. Calkins, A. C. Crook, R. Cutri, P. Erdoğdu, E. Falco, T. George, C. M. Hutcheson, O. Lahav, J. Mader, J. D. Mink, N. Martimbeau, S. Schneider, M. Skrutskie, S. Tokarz, and M. Westover (Apr. 2012). “The 2MASS Redshift Survey—Description and Data Release”. *The Astrophysical Journal Supplement* 199 (2), 26: p. 26.
- [23] T. Mauch, T. Murphy, H. J. Buttery, J. Curran, R. W. Hunstead, B. Piestrzynski, J. G. Robertson, and E. M. Sadler (July 2003). “SUMSS: a wide-field radio imaging survey of the southern sky - II. The source catalogue”. *Monthly Notices of the Royal Astronomical Society* 342 (4): pp. 1117–1130.
- [24] H. T. Intema, P. Jagannathan, K. P. Mooley, and D. A. Frail (Feb. 2017). “The GMRT 150 MHz all-sky radio survey. First alternative data release TGSS ADR1”. *Astronomy and Astrophysics* 598: A78.

- [25] P. Tiwari, S. Ghosh, and P. Jain (Dec. 2019). “The Galaxy Power Spectrum from TGSS ADR1 and the Effect of Flux Calibration Systematics”. *The Astrophysical Journal* 887 (2): p. 175.
- [26] R. B. Rengelink, Y. Tang, A. G. de Bruyn, G. K. Miley, M. N. Bremer, H. J. A. Roettgering, and M. A. R. Bremer (Aug. 1997). “The Westerbork Northern Sky Survey (WENSS), I. A 570 square degree Mini-Survey around the North Ecliptic Pole”. *Astronomy and Astrophysics Supplement Series* 124 (2): pp. 259–280.
- [27] N. J. Secrest, S. v. Hausegger, M. Rameez, R. Mohayaee, S. Sarkar, and J. Colin (Feb. 2021). “A Test of the Cosmological Principle with Quasars”. *The Astrophysical Journal* 908 (2): p. L51.
- [28] C. A. P. Bengaly, T. M. Siewert, D. J. Schwarz, and R. Maartens (Apr. 2019). “Testing the standard model of cosmology with the SKA: the cosmic radio dipole”. *Monthly Notices of the Royal Astronomical Society* 486 (1): 1350–1357.
- [29] Bertin, E. and Arnouts, S. (1996). “SExtractor: Software for source extraction”. *Astron. Astrophys. Suppl. Ser.* 117 (2): pp. 393–404.
- [30] N. Mohan and D. Rafferty (Feb. 2015). “PyBDSF: Python Blob Detection and Source Finder”, ascl:1502.007.
- [31] M. Hardcastle and J. Croston (June 2020). “Radio galaxies and feedback from AGN jets”. *New Astronomy Reviews* 88: p. 101539.
- [32] C. Mancuso, A. Lapi, I. Prandoni, I. Obi, J. Gonzalez-Nuevo, F. Perrotta, A. Bressan, A. Celotti, and L. Danese (June 2017). “Galaxy Evolution in the Radio Band: The Role of Star-forming Galaxies and Active Galactic Nuclei”. *The Astrophysical Journal* 842 (2): p. 95.
- [33] G. F. R. Ellis and J. E. Baldwin (Jan. 1984). “On the expected anisotropy of radio source counts”. *Monthly Notices of the Royal Astronomical Society* 206: pp. 377–381.
- [34] R. Maartens, C. Clarkson, and S. Chen (2018). “The kinematic dipole in galaxy redshift surveys”. *Journal of Cosmology and Astroparticle Physics* 01: p. 013.
- [35] A. Einstein (1905). “Zur Elektrodynamik bewegter Körper”. *Annalen der Physik* 322 (10): pp. 891–921.
- [36] C. Bonvin and R. Durrer (Sept. 2011). “What galaxy surveys really measure”. *Physical Review D* 84 (6).
- [37] A. Challinor and A. Lewis (Aug. 2011). “Linear power spectrum of observed source number counts”. *Physical Review D* 84 (4).
- [38] E. Di Dio, F. Montanari, J. Lesgourgues, and R. Durrer (2013). “The CLASSgal code for Relativistic Cosmological Large Scale Structure”. *Journal of Cosmology and Astroparticle Physics* 1311: p. 044.
- [39] D. Alonso, P. Bull, P. G. Ferreira, R. Maartens, and M. G. Santos (Nov. 2015). “Ultra-large scale cosmology with next-generation experiments”. *The Astrophysical Journal* 814 (2): p. 145.
- [40] P. Tiwari and P. K. Aluri (June 2019a). “Large Angular-scale Multipoles at Redshift 0.8”. *The Astrophysical Journal* 878 (1): p. 32.
- [41] N. Kaiser (Sept. 1984). “On the spatial correlations of Abell clusters.” *Astrophysical Journal* 284: pp. L9–L12.

- [42] R. Durrer (2020). *The Cosmic Microwave Background*. 2nd ed. Cambridge University Press.
- [43] D. Blas, J. Lesgourgues, and T. Tram (2011). “The Cosmic Linear Anisotropy Solving System (CLASS) II: Approximation schemes”. *Journal of Cosmology and Astroparticle Physics* 1107: p. 034.
- [44] F. Crawford (Feb. 2009). “Detecting the cosmic dipole anisotropy in large-scale radio surveys”. *The Astrophysical Journal* 692 (1): pp. 887–893.
- [45] E. W. Weisstein (2021a). *Noncentral Chi-Squared Distribution*. <https://mathworld.wolfram.com/NoncentralChi-SquaredDistribution.html>. [From MathWorld - A Wolfram Web Resource; accessed 15-March-2021].
- [46] A. Nuttall (1975). “Some integrals involving the  $Q_M$  function (Corresp.)” *IEEE Transactions on Information Theory* 21 (1): pp. 95–96.
- [47] A. Zonca, L. Singer, D. Lenz, M. Reinecke, C. Rosset, E. Hivon, and K. Gorski (Mar. 2019). “healpy: equal area pixelization and spherical harmonics transforms for data on the sphere in Python”. *Journal of Open Source Software* 4 (35): p. 1298.
- [48] K. M. Gorski, E. Hivon, A. J. Banday, B. D. Wandelt, F. K. Hansen, M. Reinecke, and M. Bartelmann (Apr. 2005). “HEALPix: A Framework for High-Resolution Discretization and Fast Analysis of Data Distributed on the Sphere”. *The Astrophysical Journal* 622 (2): 759–771.
- [49] S. Chen and D. J. Schwarz (2016). “Angular two-point correlation of NVSS galaxies revisited”. *Astronomy and Astrophysics* 591: A135.
- [50] van Velzen, Sjoert, Falcke, Heino, Schellart, Pim, Nierstenhöfer, Nils, and Kampert, Karl-Heinz (2012). “Radio galaxies of the local universe - All-sky catalog, luminosity functions, and clustering”. *Astronomy and Astrophysics* 544: A18.
- [51] A. Nusser and P. Tiwari (Oct. 2015). “The Clustering of Radio Galaxies: Biasing and Evolution Versus Stellar Mass”. *The Astrophysical Journal* 812 (1): p. 85.
- [52] A. Bonaldi, M. Bonato, V. Galluzzi, I. Harrison, M. Massardi, S. Kay, G. De Zotti, and M. L. Brown (Sept. 2018). “The Tiered Radio Extragalactic Continuum Simulation (T-RECS)”. *Monthly Notices of the Royal Astronomical Society* 482 (1): 2–19.
- [53] van Haarlem, M. P., Wise, M. W., Gunst, A. W., Heald, G., McKean, J. P., Hessels, J. W. T., de Bruyn, A. G., Nijboer, R., Swinbank, J., Fallows, R., Brentjens, M., Nelles, A., Beck, R., Falcke, H., Fender, R., Hörandel, J., Koopmans, L. V. E., Mann, G., Miley, G., Röttgering, H., et al. (2013). “LOFAR: The LOW-Frequency ARray”. *Astronomy and Astrophysics* 556: A2.
- [54] E. K. Mahony, R. Morganti, I. Prandoni, I. M. van Bemmell, T. W. Shimwell, M. Brienza, P. N. Best, M. Brüggen, G. Calistro Rivera, F. de Gasperin, M. J. Hardcastle, J. J. Harwood, G. Heald, M. J. Jarvis, S. Mandal, G. K. Miley, E. Retana-Montenegro, H. J. A. Röttgering, J. Sabater, et al. (Sept. 2016). “The Lockman Hole project: LOFAR observations and spectral index properties of low-frequency radio sources”. *Monthly Notices of the Royal Astronomical Society* 463 (3): pp. 2997–3020.
- [55] P. Tiwari and P. K. Aluri (June 2019b). “Large Angular-scale Multipoles at Redshift  $\sim 0.8$ ”. *The Astrophysical Journal* 878 (1): p. 32.

- [56] E. Hivon, K. M. Gorski, C. B. Netterfield, B. P. Crill, S. Prunet, and F. Hansen (Mar. 2002). “MASTER of the Cosmic Microwave Background Anisotropy Power Spectrum: A Fast Method for Statistical Analysis of Large and Complex Cosmic Microwave Background Data Sets”. *The Astrophysical Journal* 567 (1): 2–17.
- [57] C. Blake, P. G. Ferreira, and J. Borrill (July 2004). “The angular power spectrum of NVSS radio galaxies”. *Monthly Notices of the Royal Astronomical Society* 351 (3): 923–934.
- [58] P. R. M. Eisenhardt, F. Marocco, J. W. Fowler, A. M. Meisner, J. D. Kirkpatrick, N. Garcia, T. H. Jarrett, R. Koontz, E. J. Marchese, S. A. Stanford, D. Caselden, M. C. Cushing, R. M. Cutri, J. K. Faherty, C. R. Gelino, A. H. Gonzalez, A. Mainzer, B. Mobasher, D. J. Schlegel, et al. (Apr. 2020). “The CatWISE Preliminary Catalog: Motions from WISE and NEOWISE Data”. *The Astrophysical Journal Supplement Series* 247 (2): p. 69.
- [59] E. L. Wright, P. R. M. Eisenhardt, A. K. Mainzer, M. E. Ressler, R. M. Cutri, T. Jarrett, J. D. Kirkpatrick, D. Padgett, R. S. McMillan, M. Skrutskie, S. A. Stanford, M. Cohen, R. G. Walker, J. C. Mather, D. Leisawitz, T. N. Gautier, I. McLean, D. Benford, C. J. Lonsdale, et al. (Nov. 2010). “The Wide-field Infrared Survey Explorer (WISE): mission description and initial on-orbit performance”. *The Astronomical Journal* 140 (6): pp. 1868–1881.
- [60] R. Laureijs, J. Amiaux, S. Arduini, J. L. Auguères, J. Brinchmann, R. Cole, M. Cropper, C. Dabin, L. Duvet, A. Ealet, B. Garilli, P. Gondoin, L. Guzzo, J. Hoar, H. Hoekstra, R. Holmes, T. Kitching, T. Maciaszek, Y. Mellier, et al. (2011). *Euclid Definition Study Report*.
- [61] LSST Science Collaboration, P. A. Abell, J. Allison, S. F. Anderson, J. R. Andrew, J. R. P. Angel, L. Armus, D. Arnett, S. J. Asztalos, T. S. Axelrod, S. Bailey, D. R. Ballantyne, J. R. Bankert, W. A. Barkhouse, J. D. Barr, L. F. Barrientos, A. J. Barth, J. G. Bartlett, A. C. Becker, et al. (2009). *LSST Science Book, Version 2.0*.
- [62] D. Korytov, A. Hearin, E. Kovacs, P. Larsen, E. Rangel, J. Hollowed, A. J. Benson, K. Heitmann, Y.-Y. Mao, A. Bahmanyar, and et al. (Dec. 2019). “CosmoDC2: A Synthetic Sky Catalog for Dark Energy Science with LSST”. *The Astrophysical Journal Supplement Series* 245 (2): p. 26.
- [63] D. J. Bacon, R. A. Battye, P. Bull, S. Camera, P. G. Ferreira, I. Harrison, D. Parkinson, A. Pourtsidou, M. G. Santos, and et al. (2020). “Cosmology with Phase 1 of the Square Kilometre Array Red Book 2018: Technical specifications and performance forecasts”. *Publications of the Astronomical Society of Australia* 37.
- [64] E. W. Weisstein (2021b). *Spherical Harmonic*. <https://mathworld.wolfram.com/SphericalHarmonic.html>. [From MathWorld - A Wolfram Web Resource; accessed 8-April-2021].
- [65] P. J. E. Peebles (Oct. 1973). “Statistical Analysis of Catalogs of Extragalactic Objects. I. Theory”. *Astrophysical Journal* 185: pp. 413–440.
- [66] P. Coles and F. Lucchin (2002). *Cosmology: The Origin and Evolution of Cosmic Structure*. 2nd ed. Wiley.

- 
- [67] A. J. S. Hamilton (Apr. 2001). “Formulae for growth factors in expanding universes containing matter and a cosmological constant”. *Monthly Notices of the Royal Astronomical Society* 322 (2): 419–425.
- [68] C. R. Harris, K. J. Millman, S. J. van der Walt, R. Gommers, P. Virtanen, D. Cournapeau, E. Wieser, J. Taylor, S. Berg, N. J. Smith, R. Kern, M. Picus, S. Hoyer, M. H. van Kerkwijk, M. Brett, A. Haldane, J. F. del R'io, M. Wiebe, P. Peterson, et al. (Sept. 2020). “Array programming with NumPy”. *Nature* 585 (7825): pp. 357–362.
- [69] E. Jones, T. Oliphant, P. Peterson, et al. (2001–). *SciPy: Open source scientific tools for Python*.
- [70] Astropy Collaboration, T. P. Robitaille, E. J. Tollerud, P. Greenfield, M. Droettboom, E. Bray, T. Aldcroft, M. Davis, A. Ginsburg, A. M. Price-Whelan, W. E. Kerzendorf, A. Conley, N. Crighton, K. Barbary, D. Muna, H. Ferguson, F. Grollier, M. M. Parikh, P. H. Nair, et al. (Oct. 2013). “Astropy: A community Python package for astronomy”. *Astronomy and Astrophysics* 558, A33: A33.
- [71] Astropy Collaboration, A. M. Price-Whelan, B. M. Sipőcz, H. M. Günther, P. L. Lim, S. M. Crawford, S. Conseil, D. L. Shupe, M. W. Craig, N. Dencheva, A. Ginsburg, J. T. VanderPlas, L. D. Bradley, D. Pérez-Suárez, M. de Val-Borro, T. L. Aldcroft, K. L. Cruz, T. P. Robitaille, E. J. Tollerud, et al. (Sept. 2018). “The Astropy Project: Building an Open-science Project and Status of the v2.0 Core Package”. *The Astronomical Journal* 156 (3), 123: p. 123.
- [72] Wolfram Research, Inc. *Mathematica, Version 10.3*.
- [73] J. D. Hunter (2007). “Matplotlib: A 2D graphics environment”. *Computing in Science & Engineering* 9 (3): pp. 90–95.

---

### Scientific Acknowledgements

I acknowledge the use of NumPy [68], SciPy [69], Astropy [70, 71], healpy [47] and Mathematica [72]. Plots have been produced with Matplotlib [73].

## Acknowledgements

I am extremely grateful to Ruth Durrer and Martin Kunz for an excellent supervision and guidance throughout this one-year project. Equally, I thank Hamsa Padmanabhan for taking part in the supervision after a few months and helping this project with valuable insights since. It was a great pleasure and a valuable experience to have been working with you. I appreciate your kindness, patience and that I was able to learn a lot through your knowledge and expertise.

I would like to thank Jochen Weller for officially supervising the project. Especially, I very much appreciate how you supported the idea to go abroad for a master's project from the very beginning as well as taking the time to help me with different applications for scholarships.

I am grateful to the Cosmology Group in Geneva for their warm and friendly welcome. While it is a shame that the Coronavirus prevented me from getting to know many of you better, I greatly enjoyed any encounter through the journal club, seminar or as teaching assistants.

I acknowledge the financial support by the Cusanuswerk throughout my studies and the SEMP for the duration of this project.

I am immensely grateful to my family, Andrea, Bruno and Johanna for always supporting me in all kinds of matters. It is only for you that I have so many possibilities, such as moving to Switzerland for this research project.

Finally, I cannot thank Nicola enough for all the support along the way.

## **Erklärung**

Hiermit erkläre ich, die vorliegende Arbeit selbständig verfasst zu haben und keine anderen als die in der Arbeit angegebenen Quellen und Hilfsmittel benutzt zu haben.

Ecublens, der 15. April 2021